Università di Palermo
Dipartimento di Scienze Fisiche ed Astronomiche

Dottorato di Ricerca in Fisica
XIV ciclo
A.A. 2000/2001

X-ray Emission from Early-Type Galaxies in Groups and Poor Clusters.

Author
Paolillo Maurizio

Supervisor
Prof. G. Peres

ABSTRACT

We present the study of three bright Early-Type galaxies hosted in groups or poor clusters: NGC 1399, NGC 1404 and NGC 507. We used ROSAT HRI and PSPC data to study the morphological structure of the X-ray halo and, when available, the higher resolution *Chandra* data. Our study revealed a complex halo structure for the two dominant cluster galaxies, NGC 1399 and NGC 507. The halo center was found to be dominated by a bright X-ray peak coincident with the position of the optical galaxy. This central peak is not explained by the classical homogeneous or inhomogeneous cooling flow models. Instead our data suggest that these features are produced by stellar ejected material, kinetically heated by stellar mass losses. The total mass distribution shows that, within the effective radius, the hot halo distribution is essentially tracing the galactic potential due to luminous matter. At larger distances the halo dynamics is dominated by a large amount of dark matter extending on group and cluster scales. The NGC 1399 X-ray halo possess a more complex morphology than NGC 507. This finding requires either that the dark matter distribution has a hierarchical structure, or that environmental effects (ram stripping from ICM, tidal interaction with nearby galaxies) are producing departures from hydrostatic equilibrium. We found significant density fluctuations in the hot gas distribution of both NGC 1399 and NGC 507. Some of these features are explained by the interaction of the radio-emitting plasma, filling the radio jets and lobes, with the surrounding ISM. This evidence indicates that Radio/X-ray interactions are a more widespread phenomena than observed before. The nature of the remaining structures is more uncertain: we speculate that they can be the result of galaxy-galaxy encounters or wakes produced by the motion of the galaxy through the ICM. Alternatively they may reflect the inhomogeneity of the cooling process invoked by many authors as an explanation for the failure of the standard cooling-flow models.

NGC 1404 represents a puzzling case. In fact, despite a large X-ray luminosity and halo temperature, which suggest a similarity with dominant cluster members, significant differences are found in the regular halo profile, small velocity dispersion and low metallicity. These conflicting evidences can be explained assuming that environmental effects, such as stifling of galactic winds by the ICM, are affecting the physical status of the halo.

Finally, we studied the population of discrete sources found in proximity of the two dominant galaxies. We were able to assess that the observed excess of sources observed in the Fornax cluster is associated with NGC 1399. This result was later confirmed by the higher resolution *Chandra* data.

Contents

INTRODUCTION **i**

1 X-RAY EMISSION FROM EARLY-TYPE GALAXIES **1**

1.1 THE EARLY-TYPE GALAXIES 1

1.1.1 cD Galaxies 3

1.2 X-RAY PROPERTIES OF NORMAL EARLY–TYPE GALAXIES 4

1.3 X-RAY EMISSION MECHANISMS 8

1.3.1 Thermal Emission 8

1.3.2 Inverse Compton scattering 11

1.3.3 Discrete Sources Emission 14

1.4 PHYSICAL STATUS OF THE HALO 17

1.4.1 Beta isothermal model 17

1.4.2 Empirical Gas Distributions 19

1.4.3 Total Mass Determination 20

1.5 COOLING FLOWS 22

1.6 ENVIRONMENTAL EFFECTS 24

2 NGC 1399 **27**

2.1 INTRODUCTION 27

2.2 OBSERVATIONS AND DATA ANALYSIS 29

2.2.1 Aspect Correction 29
2.2.2 Composite Observation and Exposure Corrections 30
2.2.3 Surface Brightness Distribution and X-ray/Optical Comparison . . . 32
2.2.4 Radial Brightness Profiles 34
2.2.5 Bidimensional Halo Models 40
2.2.6 Density, Cooling Time and Mass Profiles 45
2.2.7 Total Fluxes and Luminosities 49
2.2.8 X-ray/Radio Comparison 49
2.2.9 Discrete Sources 53
2.2.10 The *Chandra* data 59
2.3 DISCUSSION 63
2.3.1 Origin of the Central X-ray Peak 63
2.3.2 Dynamical Status of the Halo 65
2.3.3 X-ray/Radio Interactions 69
2.3.4 Discrete sources 72

3 NGC 1404 73

3.1 INTRODUCTION 73
3.2 OBSERVATIONS AND DATA ANALYSIS 74
3.2.1 Brightness Distribution and X-ray/Optical Comparison 74
3.2.2 Radial Brightness Profiles 75
3.2.3 Density, Cooling Time and Mass Profiles 78
3.2.4 Total Fluxes and Luminosities 79
3.3 DISCUSSION 79

4 NGC 507 83

4.1 INTRODUCTION 83

4.2 OBSERVATIONS AND DATA ANALYSIS 84
4.2.1 The Data 84
4.2.2 Surface Brightness Distribution 86
4.2.3 X-ray/Radio Comparison 89
4.2.4 Bidimensional Halo Model 91
4.2.5 Radial Brightness Profiles 92
4.2.6 Density, Cooling Time and Mass Profiles 96
4.2.7 Discrete Sources 102
4.3 DISCUSSION 107
4.3.1 Origin of the Central Component 107
4.3.2 X-ray/Radio Correlations 108
4.3.3 Large-scale Halo structure 110
4.3.4 Discrete Sources 112

5 DISCUSSION 113

5.1 Summary of the Results 113
5.1.1 NGC 1399 113
5.1.2 NGC 1404 114
5.1.3 NGC 507 115
5.2 The Origin of the Central Emission Peak in NGC 1399 and NGC 507 116
5.3 Dynamical Status of the Halo 118
5.4 NGC 1404: a peculiar galaxy? 120
5.5 Density Fluctuations in the ISM 121
5.6 X-ray/Radio Interaction 122
5.7 Discrete Sources Population 123

CONCLUSIONS 124

ACKNOWLEDGEMENTS **127**

LIST OF ACRONYMS AND ABBREVIATIONS **129**

BIBLIOGRAPHY **132**

INTRODUCTION

This thesis discusses the X-ray properties of Early-Type (i.e. Elliptical and S0) galaxies in groups and poor clusters. We focus on the brightest Early-Type (BETG) whose X-ray luminosity is dominated by the thermal emission from the gaseous halo. The study of these hot halos is of fundamental importance for understanding BETG, since its properties are connected with the evolution of the stellar population and to the formation history of the galaxy; moreover they are very good tracers of the gravitational structure and allow us to study the amount of dark matter hosted by these systems.

Despite the fast development of scientific instrumentation and analysis methods, the X-ray properties of BETG are still a matter of debate. The X-ray satellites of the last generation (*Chandra* and XMM) permit to clearly separate, for the first time, the contribution of different components (i.e. accreting binaries, hot gas, cooling flow); however their discoveries are also seriously challenging many of the classical models used to describe the physical status of the halos. For instance the large scatter of the X-ray properties of BETG, which show instead a high degree of homogeneity in optical bands, is not fully understood. The cooling flow models, which were assumed to be responsible for the structure of the inner halo, are not able to describe the temperature structure of the hot gas; the presence of multiphase medium, that they predict, is still uncertain and the fate of the accreted material is still unknown. Studies of large samples of Early-Type galaxies are suggesting that the X-ray structure of these systems is mostly determined by the gravitational potential well produced by large amounts of dark matter rather than by thermal mechanisms.

These problems are enhanced in dominant Early-Types at the center of groups or clusters of galaxies since these objects lie at bottom of large-scale potential structures which must affect the hot gas properties. Moreover they are likely to form and evolve through interactions with nearby galaxies and with the Intra Cluster Medium, and may thus reveal how important these mechanisms are in the galaxy formation framework.

In the present work we study BETG through pointed and archival data of the ROSAT and *Chandra* X-ray satellites. We choose galaxies at the center of two nearby systems: the

Fornax cluster, a poor cluster located located $\sim$ 20 Mpc from our galaxy, and the NGC 507 group, which is part of the Pisces cluster located at $\sim$ 66 Mpc. These systems host very bright dominant galaxies which, due to their proximity, permit a detailed study of their X-ray properties. The choice to study BETG in poor clusters and groups is justified by the fact that these environments allow us to better disentangle the properties of individual galaxies from those of the ICM: the intergalactic gas is less dense than in rich clusters and there are no large cluster cooling flows which may affect the formation and evolution of the dominant galaxies.

We will focus on the analysis of the morphology and of the dynamical structure of the X-ray halo in order to separate small and large scale structures and to determine to which extent the galactic halo properties are influenced by the local environment. We will then investigate the presence of interaction between the radio sources, hosted in the core of some galaxies, and the surrounding interstellar medium. When possible we will also study the properties of the discrete source population.

The comparison between different galaxies will help to understand which mechanisms play a fundamental role in determining the X-ray properties of bright Early-Type galaxies and, more in general, affect the formation and evolution of these massive systems.

The thesis is organized as follows:
- in chapter 1 we introduce the properties of Early-Type galaxies in the X-ray band and discuss the main sources of X-ray emission. We then focus on the informations that can be inferred from the study of the X-ray halos and on the effect of the local environment, paying particular attention to the latest developments;
- in chapters 2, 3 and 4 we present the data analysis concerning the individual galaxies and discuss the results on each object separately. A preliminary version of the work discussed in Chapter 2 is presented in Paolillo et al. (2000, 2001); the final results of Chapters 2 and 3 have been published in Paolillo et al. (2002). Chapter 4 will be included in a separate paper that is currently in preparation;
- in chapter 5 we compare the results on the individual galaxies obtained in previous chapters and discuss global properties of bright Early-Type X-ray emission in the context of the different halo formation and evolution scenarios.

Chapter 1

X-RAY EMISSION FROM EARLY-TYPE GALAXIES

1.1. THE EARLY-TYPE GALAXIES

Early-type galaxies are large, bright stellar systems with considerable structural regularity. According to the Hubble (1926) criteria (Figure 1.1), which classifies galaxies based on their morphology and light concentration toward the nucleus, the Early-Type galaxies represent a group which includes both Elliptical (E0-E7) and Lenticular (S0) galaxies. These stellar systems are characterized by approximately elliptical and concentric isophotes with axial ratios ranging from 1 (E0) to 0.3 (E7). In the case of S0 galaxies the elliptical bulge is integrated by a disk component, missing the 'arms' typical of spiral (S) galaxies.

The Early-Type galaxies represent a class of well studied objects both because of their homogeneous properties and because of their high luminosity (absolute magnitudes in the range $-24 < M_B < -20$) which allows to detect them at large distances. These objects are usually composed by an 'old' stellar population, since the last major star formation event occurred several Gyrs ago. Their optical emission is thus centered at longer wavelengths with respect to the 'bluer' spiral galaxies. Photometric studies (Capaccioli 1989; Caon, Capaccioli & D'Onofrio 1993) revealed that the surface brightness of Ellipticals is well represented by a *de Vaucouleurs* profile (de Vaucouleurs 1948):

$$\log\left[\frac{I(r)}{I(r_c)}\right] = -3.331\left[\left(\frac{r}{r_c}\right)^{1/4} - 1\right] \tag{1.1}$$

where I represents the surface brightness, r is the projected distance from the galactic center

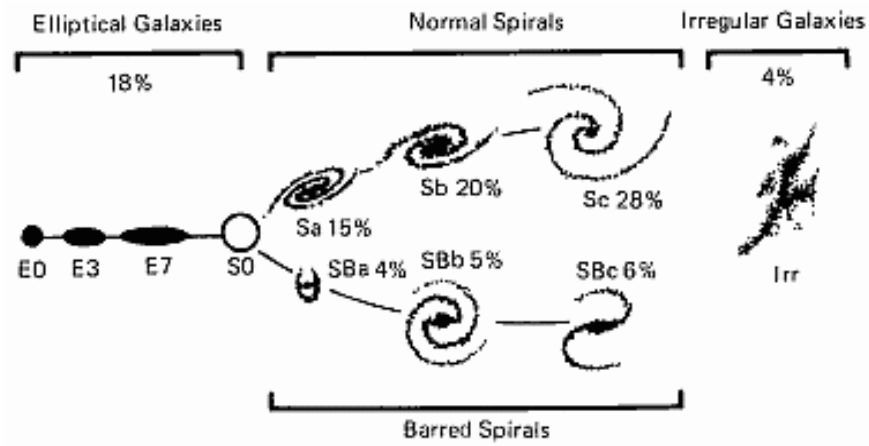

Fig. 1.1.— The Hubble (1926) classification of galaxies. The numbers represent the relative abundance of each type.

and r_c is the *effective radius*, i.e. the radius which includes half of the total light of the galaxy. S0 galaxies possess an additional disk component with an exponential profile:

$$I(r) = I_0 \exp(-r/r_d) \tag{1.2}$$

where I_0 is the central brightness and r_d is the disc scale length.

Unlike Late-Type galaxies (Spirals and Irregulars), Early-Types have depleted already their hydrogen supply either by forming stars or ejecting it into the Intra Cluster Medium (ICM) (Sarazin 1988). However while the content of cold gas, emitting at optical wavelengths, is usually small, we will see in § 1.2 that this situation is reversed when we take into account the hot, fully-ionized Inter Stellar Medium (ISM).

The stellar dynamic of these systems is characterized by a high triaxial velocity dispersion and small or no rotation (de Zeeuw & Franx 1991, and references therein). For this reason Early-Type galaxies are often called 'hot systems' with a dynamical temperature $T_{dyn} = \mu m_p \sigma^2/k \sim 1.4 - 5.4 \times 10^6$ K, where μ is the mean molecular mass, m_p the proton mass, k the Boltzmann constant and $\sigma \sim 150 - 300$ km s^{-1} the stellar velocity dispersion (e.g. Whitmore, McElroy & Tonry 1985; Graham et al. 1998). The homogeneity of Elliptical galaxies is supported by the fact that stellar velocity dispersion, surface brightness and effective radius are constrained to a 'fundamental plane' (Djorgovski & Davis 1987; Dressler et al. 1987).

Early-Type galaxies are found to be more numerous in high-density environments, such as groups or clusters of galaxies. This suggests that their formation is related, to some extent, to galaxy-galaxy interactions: Elliptical galaxies may accrete either by means of

tidal interactions, capturing smaller galaxies or part of them in their deeper potential well, or by merging of smaller systems, maybe Spirals which loose part of their angular momentum, creating a spheroidal system with high velocity dispersion (Barnes 1988; Barnes & Hernquist 1992; Hernquist 1993).

1.1.1. cD Galaxies

Even though Early-Type galaxies seem to be a nearly homogeneous class, the data acquired in the last 20 years has shown that significant departures from the general properties are often present in the form of large quantities of dust and gas (Capaccioli & Longo 1994), anomalous or counter-rotating nuclei, polar rings (Bertola & Galletta 1978; Bender 1988; Whitmore, McElroy & Schweizer 1987). Moreover Elliptical galaxies are often strong X-ray and radio emitters.

Within the peculiar Early-Type galaxies there are the largest known stellar systems: the giant cD Ellipticals. cD galaxies were defined by Mathews, Morgan & Schmidt (1964) as galaxies with a nucleus of a very luminous Elliptical (represented by the *de Vaucouleur* brightness profile) embedded in an extended amorphous halo of low surface brightness. They are usually found at the center of regular, compact clusters of galaxies (Bautz & Morgan 1970) but several cDs have been also found in poor clusters and groups (Morgan, Kayser & White 1975; Albert, White & Morgan 1977; Killeen & Bicknell 1988). Their peculiar nature is confirmed by the fact that these galaxies are too bright ($M_V \geq -24$) to belong to the same galaxy luminosity function that fits the other bright Ellipticals distribution (Schechter 1976). They also often have double or multiple nuclei (Minkowski 1961; Hoessel 1980; Schneider & Gunn 1982) and/or intense X-ray and radio emission.

Their special structural and kinematic properties suggest that they have been formed or modified by dynamical processes in clusters. Gallagher & Ostriker (1972) and Richstone (1975, 1976) have suggested that cDs consist of the debris from galaxy collisions in which the outer envelopes of galaxies are stripped by tidal effects and then settle at the cluster center. An alternative scenario (Ostriker & Tremaine 1975; Gunn & Tinsley 1976) is one in which the orbits of massive cluster galaxies decay due to dynamical friction and subsequently merge in the cluster center forming a single massive galaxy. This galaxy would then swallow any smaller galaxy passing through the cluster center (the so called 'galactic cannibalism', Ostriker & Hausman 1977). However the core of a rich cluster is a very active physical environment in which many other processes may be important.

1.2. X-RAY PROPERTIES OF NORMAL EARLY–TYPE GALAXIES

The first identification of extragalactic X-ray sources and their association with galaxy clusters were made with balloon and rocket-borne detectors (e.g. Byram, Chubb & Friedman 1966; Fritz et al. 1971) while the study of their physical properties begun with the *Uhuru*, *Ariel* and HEAO satellites (e.g. Kellogg et al. 1973; Kellogg 1973, 1975; Elvis et al. 1975; Ulmer et al. 1981). However, before the launch of the *Einstein* satellite (Giacconi et al. 1979), just four individual galaxies had been detected in X-rays[1]: the Milky Way, M31 and the Magellanic Clouds. In general the so called 'normal' galaxies were thought to be of little interest for X-ray astronomy because they were missing an active nucleus or star forming regions.

The *Einstein* satellite showed that normal Early-Type galaxies are strong X-ray emitters with luminosities ranging from 10^{39} erg s^{-1} to 10^{43} erg s^{-1}, the upper limits being reached by cD galaxies in the center of rich clusters. *Einstein* (see Fabbiano 1989 for a review of *Einstein* results) and the following generation of X-ray satellites with improved spatial and spectral resolution (ROSAT: Pfeffermann et al. 1987, David et al. 1996; ASCA: Tanaka, Inoue & Holt 1994; Beppo-SAX: Boella et al. 1997) allowed to study in detail the properties of these systems.

Different physical mechanism were suggested to be responsible for the X-ray luminosity of normal Early-Type galaxies: i) integrated stellar coronal emission; ii) thermal emission due to the hot ISM; iii) end products of stellar evolution (compact binary systems and supernovae remnants); iv) X-ray diffuse emission due to non-thermal processes.

Stellar coronae have X-ray luminosities reaching up to 10^{33} erg s^{-1} (Vaiana et al. 1981) but their integrated emission does not contribute significantly to the total X-ray emission of normal Early-Type galaxies, except for the fainter ones or at low energies (< 0.3 keV, e.g. Pellegrini & Fabbiano 1994). Instead, the emission coming from hot ISM and end products of stellar evolution must be taken both into account to explain the Early-Type X-ray emission. Fabbiano (1984) and Forman, Jones & Tucker (1985) have shown that Elliptical galaxies must be divided in two groups depending on their total luminosity. Objects with $L_X < 10^{41}$ erg s^{-1} seems to be dominated by the integrated emission of compact accreting systems. This is demonstrated by the 'hard' spectra (kT$>$ 2 keV) and by the correlation between optical and X-ray luminosity similar to the one seen for Spiral galaxies, whose emission is

[1]Excluding sources associated with Seyfert nuclei

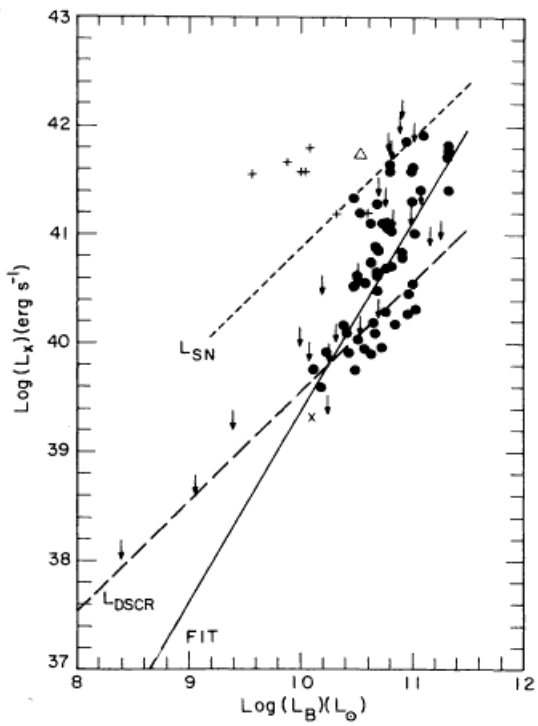

Fig. 1.2.— Early-Type galaxies with high X-ray luminosity (filled circles) show a steeper correlation (continuous line), in the L_X-L_B plane, different from the one expected if the emission was due only to discrete sources (long-dashed line), as happens for Spirals and fainter Ellipticals. L_{SN} represent the expected correlation if the hot gas is heated by Supernovae explosions (from Canizares, Fabbiano & Trinchieri 1987).

mostly due to discrete sources (Kim, Fabbiano & Trinchieri 1992b; Irwin & Sarazin 1998b; Trinchieri et al. 2000, and references therein).

Early-Type galaxies with $L_X > 10^{41}$ erg s^{-1} show a correlation between L_B and L_x steeper than the one observed for Spirals and fainter Ellipticals (Figure 1.2, Canizares, Fabbiano & Trinchieri 1987). This result implies the presence of an additional component in the bright galaxies. This components is represented by hot ($\sim$ 1 keV) ISM trapped by the galaxy potential well (Eskridge, Fabbiano & Kim 1995) whose emission is due to thermal processes (see § 1.3.1).

The origin of the hot ISM is still unclear. The gas may be the remainings of the primordial gas from which the galaxy formed or may be the result of the stellar mass losses and supernovae ejections accumulated during the galaxy life. The possibility to ascertain which of these theories is true relies on our ability to measure the ISM metallicity: low

metallicities would confirm the primordial origin while near-solar ones would indicate metal enrichment after the galaxy formation. In fact primordial nucleosyntesis models predict that during the formation of the universe (the Big Bang) no elements than hydrogen, helium and lithium were formed, because of the lack of any stable isotopes with atomic weights of 5 or 8 (Weinberg 1972; see also Longair 1998). All the mechanisms which have been suggested for the formation of heavier elements involve processing in stars.

The low spectral resolution of *Einstein* and ROSAT allowed both single-temperatures spectral models with subsolar metallicities or multi-temperature fits with solar metallicities (e.g. Kim & Fabbiano 1995). However extensive ASCA studies (Matsushita, Ohashi & Makishima 2000; Buote 2000a) have now shown that the ISM metallicity is nearly solar up to great distances (~ 100 kpc) from the galaxy centers, thus supporting the stellar origin of the ISM. This result seems to be further confirmed by the latest *Chandra* results (e.g. David et al. 2000).

In X-ray faint Early-Type the hot interstellar gas, that dominates the emission of their bright counterparts, may have been lost in galactic winds (Loewenstein & Mathews 1987; David, Forman & Jones 1991), by ram-pressure stripping by ambient intracluster or intragroup gas (White & Sarazin 1991; Toniazzo & Schindler 2001). The bulk of the X-ray emission in X-ray faint Early-Type is uncertain: it might be due to low-mass X-ray binaries (LMXBs), to an active galactic nucleus (AGN, Allen, di Matteo & Fabian 2000), to interstellar gas (Pellegrini & Fabbiano 1994) or to fainter stellar sources.

In general X-ray faint galaxies have significantly different X-ray spectral properties than their X-ray bright counterparts. In fact X-ray faint galaxies exhibit two distinct spectral components. They have a hard $\sim 5-10$ keV component, most easily seen in ASCA spectra (Matsumoto et al. 1997), which is roughly proportional to the optical luminosity of the galaxy. Actually, both X-ray faint and X-ray bright Early-Type galaxies appear to have this hard X-ray component, thus suggesting that it is due to LMXBs like those seen in the bulge of our Galaxy (e.g. White, Nagase & Parmar 1995). However, the ASCA observations cannot resolve this component into discrete sources because of its low angular resolution, nor they provide much detailed information on its spectrum.

X-ray faint galaxies also have a very soft ($\sim$ 0.2 keV) component, whose origin is uncertain (Fabbiano, Kim & Trinchieri 1994; Pellegrini 1994; Kim et al. 1996). Suggested stellar sources for this soft emission include M stars and RS CVn binaries or supersoft sources (Kahabka & van den Heuvel 1997), but none of these appears to work quantitatively (Pellegrini & Fabbiano 1994; Irwin & Sarazin 1998a). It was also proposed that the soft X-rays may be due to warm (0.2 keV) ISM (Pellegrini & Fabbiano 1994) or to the same LMXBs

population responsible for the hard emission (Irwin & Sarazin 1998a,b). Recent ROSAT and *Chandra* (Weisskopf et al. 1996) studies have now identified these discrete sources in the faint Early-Type galaxy NGC 4697 and demonstrated that they can account for $> 70\%$ of the total X-ray emission (Irwin, Sarazin & Bregman 2000; Sarazin, Irwin & Bregman 2001). They also showed that, in this galaxy, the soft emission is mainly produced by warm ISM.

The presence of diffuse non-thermal X-ray emission in Early-Type galaxies requires the presence of a population of high energy electrons. The existence of such a population is now well established through radio measurements. In fact radio observations have shown collimated radio jets emanating from the nucleus itself, with velocities approaching the speed of light. The jets are believed to be made up of very energetic particles expelled from the nucleus and fueling diffuse structures called 'radio lobes'. Bright spots (hotspots) are often observed at the extremities of the lobes. The radio emission is invariably polarized and is characterized by large brightness temperatures ($10^{10} - 10^{12}$ K) so that it is assumed to be generated by the synchrotron process.

The two primary mechanisms normally considered in order to explain X-ray emission in radio sources are synchrotron emission itself and inverse Compton (IC) emission (Harris 1999). Synchrotron emission is often considered to explain X-ray emission from knots and hotspots associated with radio jets. The gas flowing in the jet at supersonic velocity, decelerates suddenly near the hot spot and this causes a shock wave to form across the jet. Before reaching the shock wave, most of the energy is in the form of ordered kinetic energy. The passage through the shock converts this into relativistic electron energy and magnetic field energy. The relativistic electrons with $\gamma \sim 10^7$ are thus able to radiate synchrotron emission in the X-ray band. An example is knot A in the M87 jet (Biretta, Stern & Harris 1991).

Alternatively the relativistic electrons, responsible for the radio emission, may scatter low energy photons into the X-ray energy band through inverse Compton. The IC process can work on any photon distribution: in particular with synchrotron emission and 3 K background photons. The synchrotron self Compton (SSC) emission requires compact, high-brightness radio structures in order to be detectable by current X-ray systems. For instance it has been established to be responsible for the hotspots of Cygnus A (Harris, Carilli & Perley 1994). IC scattering of background photons, instead, may produce diffuse, low-brightness X-ray emission corresponding with the position of the radio lobes, such as has been observed in the strong radio galaxy Fornax A (Feigelson et al. 1995; Kaneda et al. 1995). This process may be important also in faint radio galaxies and will be discussed in greater detail in § 1.3.2.

1.3. X-RAY EMISSION MECHANISMS

1.3.1. Thermal Emission

The ISM responsible for the thermal component of the X-ray emission in normal Early-Type galaxies is in the form of a hot ($T \sim 10^7$ K) and low density ($n < 10^{-1}$ cm^{-1}) plasma. In these conditions it is possible to make several simplifications (Sarazin 1988): i) the time scale for elastic Coulomb collisions between particles in the plasma is much shorter than the age, or cooling time (see § 1.5), of the plasma, and thus the free particles can be assumed to have a Maxwell-Boltzmann distribution at temperature T_g; this is the kinetic temperature of electrons which determines the rate of all excitation and ionization processes; ii) due to the low density, collisional excitation and de-excitation are much slower than radiative decays and thus any ionization or excitation process can be assumed to be initiated from the ground state of an ion; three-body (or more) collisional processes can be ignored; iii) the radiation field in a cluster is sufficiently dilute that stimulated radiative transition are not important, and the effect of the radiation field on the gas is insignificant; iv) at these low densities the gas is optically thin and the absorption processes do not affect the radiation field. These assumptions constitute the 'coronal limit', under which ionization and emission result primarily from collisions of ions with electrons (collisions with ions can be ignored). Finally, v) the time scales for ionization and recombination are generally considerably less than the age of the galaxy or any other relevant hydrodynamic time scale, so that the plasma can be assumed to be in ionization equilibrium.

In the ISM (and almost in all astrophysical plasma) hydrogen and helium are the most common elements with all the heavier elements being considerably less abundant. It is conventional to use solar abundances as a standard when studying many astrophysical systems. Since most of the electrons originate in hydrogen and helium atoms, and they are fully ionized under the conditions considered here, the electron number density is nearly independent of the state of ionization and is roughly given by $n_e = 1.21\ n_p$ where n_p is the hydrogen number density. This is the assumption that we will use throughout this work.

The X-ray continuum emission of a hot diffuse plasma is due primarily to three processes: thermal bremsstrahlung (free-free emission), recombination (free-bound) emission and two-photon decay of metastable levels. Processes that contribute to the X-ray line emission include collisional excitation of valence or inner shell electrons, radiative recombination, inner shell collisional excitation and radiative cascades following any of these processes. Compilations of emissivities (emitted energy per unit time, frequency and volume) for X-ray lines and continua have been given by various authors (e.g. Mewe, Gronenschild & van den

Oord 1985; Landini & Monsignori Fossi 1990); however throughout this work we adopted the Raymond-Smith model (Raymond & Smith 1977, and more recent updates) which is one of the most used in literature and is included in many spectral fitting packages (e.g. Xspec, CIAO).

Since all the emission processes just mentioned have emissivities proportional to the product of the ion and of the electron densities, and otherwise depend only on the temperature, we can write:

$$\epsilon(\nu, T_g) = \sum_{X,i} \Lambda_{X^i}(\nu, T_g)\ n_{X^i}\ n_e \tag{1.3}$$

where $\epsilon(\nu, T_g)$ is the emissivity at frequency ν and gas temperature T_g, Λ_{X^i} is the emission per ion at unit electron density, n_{X^i} is the number density of the i-th ionization stage of the element X and n_e is the electron number density. If n_X is the total density of the element X, in equilibrium the ionization fractions $f(X^i) = n_{X^i}/n_X$ depend only on the temperature and equation (1.3) becomes:

$$\epsilon(\nu, T_g) = n_p n_e \sum_{X,i} \frac{n_X}{n_p}[f(X^i, T_g)\ \Lambda_{X^i}(\nu, T_g)] \tag{1.4}$$

If we assume solar abundances the ratio n_X/n_p is known and the quantity $[f(X^i, T_g)\ \Lambda_{X^i}(\nu, T_g)]$ depends only on the temperature. Thus equation (1.4) can be written as:

$$\epsilon(\nu, T_g) = n_p n_e\ \Lambda(\nu, T_g) = \frac{n_e^2}{1.21}\Lambda(\nu, T_g) \tag{1.5}$$

where

$$\Lambda(\nu, T_g) = \sum_{X,i} \frac{n_X}{n_p}[f(X^i, T_g)\ \Lambda_{X^i}(\nu, T_g)] \tag{1.6}$$

is usually called 'cooling function'. Examples of cooling functions from literature, integrated over the whole spectrum, are shown in Figure 1.3. The differences arise from the different approximations and atomic models adopted by the authors to calculate the relative contribution of each physical process involved in the radiative process.

In discussing which properties can be derived by X-ray measurements we must consider that X-ray detectors allow us to measure the X-ray flux and spectrum, both of which are the result of the ISM emissivity integrated along the line of sight. $\Lambda(\nu, T_g)$, instead, depends only on the local gas properties. The shape of the spectrum thus reflects the distribution of temperatures, abundances $n(X)/n(H)$ and density through the gas. Deriving these quantities from the measured X-ray spectrum through thermal models fitting can be a very difficult task, unless we make some assumptions on how these parameters vary within the ISM. In

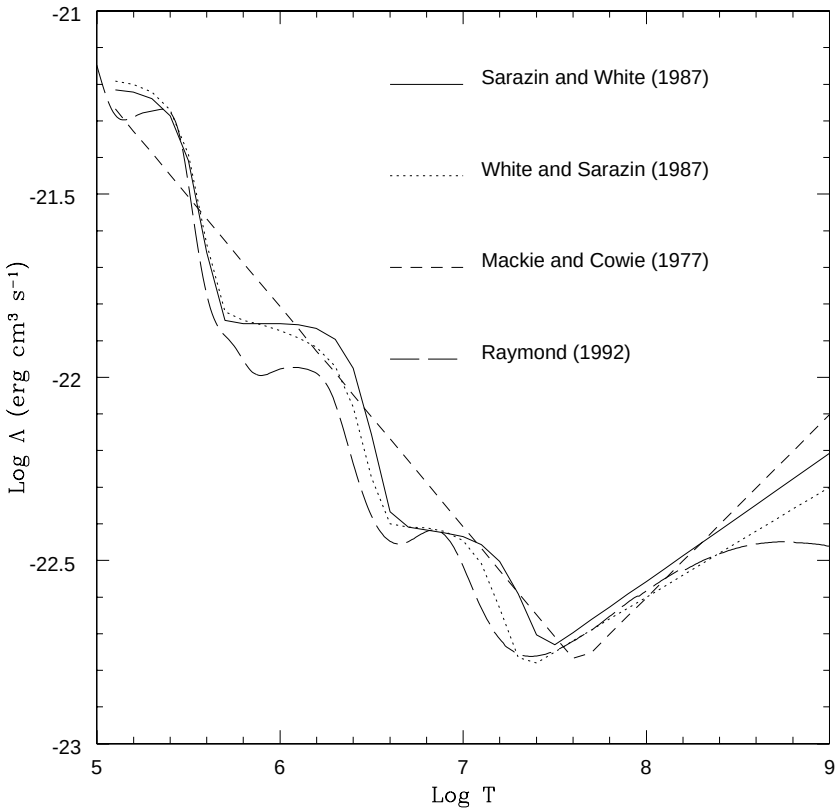

Fig. 1.3.— Bolometric cooling functions from literature.

the simplest case we can assume that the gas temperature and the chemical composition are constant along the line of sight, so that the total luminosity L_ν of a galaxy is given by:

$$L(\nu, T_g) = \int \epsilon(\nu, T_g)\mathrm{d}V = \int n_p n_e \Lambda(\nu, T_g)\mathrm{d}V = EM \cdot \Lambda(\nu, T_g) \tag{1.7}$$

where

$$EM = \int n_p n_e \mathrm{d}V \tag{1.8}$$

is the *emission measure* of the plasma and V is the emitting volume. Thus knowing T_g from the spectral fit we can derive EM.

To define completely the status of the gas we need to find n_e, and thus the gas density. This implies the knowledge of the observed volume and of the gas distribution through this volume. This problem can be solved in part assuming some simple distribution of the hot gas, such as those discussed in § 1.4. We will also see that the use of 'deprojection' techniques

allows to consider more complex situations in which the ISM is characterized by different temperatures and abundances at each radius from the galaxy center.

1.3.2. Inverse Compton scattering

Among the physical processes discussed in § 1.2, which produce non-thermal X-ray emission, we are mostly concerned with Inverse Compton scattering from the 3 K background photons (3 K IC). This is because the galaxies considered here are only weak radio sources. The radio emitting plasma is most probably moving at subsonic speed so that the shock produced at the lobe leading edge is not strong enough to produce 'hotspots'. Similarly the radio brightness is too low to produce detectable SSC emission. 3 K IC instead may be an important process also in radio faint sources and will be discussed in greater detail to obtain some important relations that will be useful later.

Nonthermal synchrotron radio emission generally has a spectrum in which the flux $S_r(\nu)$ is well represented as a power-law over a wide range of frequencies ν (Robertson 1983):

$$S_r \propto \nu^{-\alpha_r} \tag{1.9}$$

where α_r is the radio spectral index, with typical value of ~ 0.8. It is generally assumed that this spectral shape is due to the power-law energy distribution of the relativistic electrons:

$$N_e(E)\mathrm{d}E = N_0 E^{-p}\mathrm{d}E \qquad E_l < E < E_u \tag{1.10}$$

where $N_e\mathrm{d}E$ is the number of electrons with energies between E and $E + \mathrm{d}E$, $E = \gamma m_e c^2$ is the electron energy, E_l and E_u define the lower and upper energy cutoff of the distribution. In this case the number of electrons with $\gamma < 10^3$, which contribute to IC scattering of background photons to energies ~ 1 keV (Harris & Grindlay 1979), will be larger than those in the range $\gamma \sim 10^3 - 10^5$ which are responsible for the synchrotron emission, so that every radio galaxy must be a source of IC emission as well.

These extremely relativistic electrons ($\gamma >> 1$) will scatter photons with initial frequency ν_b up to an average frequency (Longair 1992):

$$< \nu_x >= \frac{4\gamma^2 \nu_b}{3}. \tag{1.11}$$

The resulting IC radiation has a spectrum given by (Sarazin 1988):

$$\frac{\mathrm{d}L_x}{\mathrm{d}\nu_x} = 3\sigma_T c h 2^p N_0 \frac{p^2 + 4p + 11}{(p+3)^2(p+1)(p+5)} \left[\int \nu_b^{\alpha_x} n_b(\nu_b)\mathrm{d}\nu_b \right] \nu_x^{\alpha_x} \tag{1.12}$$

where L_x is the X-ray luminosity emitted at frequency ν_x, n_b is the number density of background photons as a function of frequency ν_b, σ_T is the Thompson cross section, and the X-ray spectral index is related to the electron distribution index by:

$$\alpha_x = \frac{p-1}{2} \tag{1.13}$$

If the source of low energy photons is the 3 K cosmic background radiation, taken to be a blackbody at temperature T_r, then:

$$\frac{\mathrm{d}L_x}{\mathrm{d}\nu_x} = \frac{3\pi\sigma_T}{h^2c^2} b(p) N (kT_r)^3 \left(\frac{kT_r}{h\nu_x}\right)^{\alpha_x} \tag{1.14}$$

for frequencies in the range $\gamma_l^2 << (kT_r/h\nu_x) << \gamma_u^2$. The function $b(p)$ is given by Sarazin (1988).

The synchrotron radio luminosity L_r produced by the same electron population is given by

$$\frac{\mathrm{d}L_r}{\mathrm{d}\nu_r} = \frac{8\pi^2 e^2 \nu_B N_0}{c}\, a(p) \left(\frac{3\nu_B}{2\nu_r}\right)^{\alpha_r} \tag{1.15}$$

where $\nu_B \equiv eB/2\pi m_e c$ is the gyrofrequency in the magnetic field B and $a(p)$ is an analytic function of p (Sarazin 1988).

The radio spectral index α_r is equal to the X-ray index α_x. The synchrotron radio and IC X-ray emission from the same relativistic electrons will thus have the same spectral shape, reflecting the underlying electron energy distribution. The luminosities in the two bands are simply related:

$$\frac{L_x}{L_r} = \frac{U_b}{U_B} \tag{1.16}$$

where U_b and $U_B = B^2/8\pi$ are the energy density of the background radiation and of the magnetic field, respectively. This result shows that the X-ray luminosity expected from IC scattering in a radio source can be easily determined if one knows the radio luminosity and the magnetic field energy density, since the cosmic background energy density is well known. Equivalently we can determine U_B if we can measure both L_x and L_r.

In practice, fluxes at a single frequency are easier to measure than integrated luminosities. Harris & Grindlay (1979; also see Feigelson et al. 1995) obtained an expression for the magnetic field B_{IC} required to produce a measured ratio of radio to X-ray flux:

$$B_{IC} = \left[\frac{(4790)^{\alpha_r} C(\alpha_r) G(\alpha_r) (1+z)^{3-\alpha_r} S_r E_x^{\alpha_r}}{10^{70} S_x \nu^{\alpha_r} \sin\phi}\right]^{1/(1-\alpha_r)} \tag{1.17}$$

where z is the source redshift, ϕ is the angle between the (assumed) uniform magnetic field and the line of sight, S_r is the radio flux density measured in Jansky at ν_r (in GHz) and

S_x is the X-ray flux density (in ergs s^{-1} cm^{-2} Hz^{-1}) at energy E_x (in keV). The functions $C(\alpha_r)$ and $G(\alpha_r)$ are given in Harris & Grindlay (1979).

The problem in estimating the X-ray flux expected from a given radio source is to estimate the magnetic field intensity in the radio lobes, where the bulk of the IC emission originates. In fact the nature of synchrotron emission is such that it is difficult to separate the number density of relativistic electrons from the magnetic field strength. The general approach is to invoke equipartition to allow order of magnitude estimates.

The total energy contained in the lobes is given by the sum of the magnetic field energy density $U_B = B^2/8\pi$ and the particles energy density $U_p \propto B^{-3/2}$ (obtained assuming a power law distribution of the particles and a high energy cutoff, as in equation (1.10)) so that:

$$U_{tot} = aB^{-3/2} + bB^2 \tag{1.18}$$

Here a and b are two constants which depend on the power-law index p, the total radio luminosity and the energy cutoffs (see for instance Pacholczyk 1970). The equipartition approach consists simply in determining the value of B that yields the minimum energy density:

$$\frac{\partial U_{tot}}{\partial B} = -\frac{3}{2}aB^{-5/2} + 2bB = 0 \tag{1.19}$$

The full expression for the minimum energy field B_{ME} is given by Miley (1980):

$$B_{ME} = 5.69 \times 10^{-5} \left[\frac{(1+k)}{\eta}(1+z)^{3-\alpha_r} \frac{1}{\theta^2 s \sin^{3/2}\phi} \frac{S_r}{\nu_r^{\alpha_r}} \frac{\nu_2^{\alpha_r+(1/2)} - \nu_1^{\alpha_r+(1/2)}}{\alpha_r + \frac{1}{2}} \right] \tag{1.20}$$

where η is the filling factor of the synchrotron emitting region, θ is the lobe diameter (in arcseconds), s is the path length through the source (in kpc) and ν_1 and ν_2 (in GHz) are the upper and lower cutoff frequencies for the radio synchrotron spectrum. Since the synchrotron emission is essentially due to electrons, the energy density contained in heavier particles can not be inferred directly from observations. Thus the factor k, defined as the ratio of the energy in heavy particles to the energy in electrons, is introduced in equation (1.20) to take into account this contribution.

Equation (1.19) also yields $b = 3/4\ aB^{-7/2}$ and thus:

$$\frac{U_p}{U_B} = \frac{aB^{-3/2}}{bB^2} \simeq 1 \tag{1.21}$$

which explains why the minimum energy condition is also called 'equipartition'. Of course the equipartition condition is not necessarily valid but allows to obtain lower limits on the expected X-ray emission from IC scattering in radio sources.

1.3.3. Discrete Sources Emission

We have seen in § 1.2 that discrete sources contribute significantly to the X-ray emission of faint Early-Type galaxies and are present in bright galaxies too. These sources are basically represented by binary stellar systems emitting in X-rays (Trinchieri & Fabbiano 1985; Canizares, Fabbiano & Trinchieri 1987; Irwin & Sarazin 1998a,b; Irwin, Sarazin & Bregman 2000; Sarazin, Irwin & Bregman 2001). The knowledge of the properties of these objects is very important to understand the star formation history and the evolution of the stellar population in galaxies. An exhaustive treatment of the physical processes responsible for the X-ray emission in these systems is a very complex task and is beyond the aim of this work. Instead, I will qualitatively discuss the scenario in which the X-ray emission is produced and mention the main properties of this emission. More detailed informations can be found in the references included below.

An X-ray binary is composed either by a neutron star or a black hole accreting material from a companion star (see Lewin, van Paradijs & van den Heuvel 1995 for an extensive review). The primary factors that determine the emission properties of an accreting compact object are i) whether the central object is a black hole (BH) or a neutron star (NS), ii) if it is a neutron star, the strength and geometry of its magnetic field, and iii) the geometry of the accretion flow from the companion (disk vs spherical accretion). These determine whether the emission region is the small magnetic polar cap of a neutron star, a hot accretion disk surrounding a black hole, a shock heated region in a spherical inflow, or the boundary layer between an accretion disk and a neutron star. Two more factors are the mass of the central object and the mass accretion rate; these influence the overall luminosity, spectral shape and time variability of the emission.

A neutron star with a strong magnetic field ($\sim 10^{12}$ G) will disrupt the accretion flow at several hundred neutron-star-radii and funnel material onto the magnetic poles (Pringle & Rees 1972; Davidson & Ostriker 1973; Lamb, Pethick & Pines 1973). If the magnetic and rotation axes are misaligned, X-ray pulsations will be observed if the beamed emission from the magnetic poles rotates through the line of sight (Meszaros, Nagel & Ventura 1980; Nagel 1981a,b). When the magnetic field of the neutron star is relatively weak ($< 10^{10}$ G), the disk may touch or come close to the neutron star surface. The energy released from the inner accretion disk and the boundary layer between the disk and the neutron star will dominate the emission (e.g. Mitsuda et al. 1984). If the central object is a black hole the X-rays come from the inner disk and are the results of viscous heating (Shakura & Sunyaev 1973).

Instabilities in the emission region, or its influence on the nearby accretion flow, can give rise to rapid fluctuations, or quasi-periodic oscillations. The material, as it accumulates

on the neutron star, may reach a critical size and undergo a thermonuclear flash, resulting in an X-ray burst. Instabilities in the accretion flow can also give rise to X-ray bursts or flares (Taam & Fryxell 1988).

The spectral type of the companion determines the mode of the mass transfer to the compact object and the overall environment in it's vicinity. In the low-mass X-ray binaries (LMXBs) the companion is later than type A and can, in some very evolved systems, be a white dwarf. A late type or degenerate star does not have a natural wind strong enough to power the observed X-ray source. Significant mass transfer will occur only if the companion fills its critical gravitational lobe: the Roche lobe.

In high-mass X-ray binaries (HMXBs) the companion is an O or B star whose optical/UV luminosity may be comparable to, or greater than, that of the X-ray source (Conti 1978; Petterson 1978). X-ray heating is minimal, with the optical properties dominated by the companion star. The companion star has substantial stellar wind, removing $10^{-6} - 10^{-10} M_{\odot}$ yr^{-1} with a terminal velocity up to 2000 km s^{-1}. A NS or BH in a relatively close orbit will capture a significant fraction of the wind, sufficient to power the X-ray source. Roche lobe overflow can be a supplement to the mass transfer rate.

Many X-ray binaries are transient sources that appear on a timescale of a few days, and then decay over tens or hundreds of days (White, Kaluzienski & Swank 1984; van Paradijs & Verbunt 1984). The transient episodes may result from an instability in the accretion disk, or a mass ejection episode from the companion.

The flow geometry is determined by the angular momentum per specific mass of the accretion flow. If the companion star fills its critical Roche lobe, then a stream of material will be driven through the inner Lagrangian point. This stream will orbit the compact object at a radius determined by its specific angular momentum (Lubow & Shu 1975). Viscous interactions and angular momentum conservation will cause the ring to expand into a disk. The disk's outer radius is limited by tidal forces, which will transfer angular momentum back to the binary orbit.

Our knowledge of discrete sources comes basically from objects in our galaxy or in very nearby ones (e.g. M31). Only recently the use of XMM and *Chandra* satellites is revealing the properties of these sources in more distant galaxies. In particular the emission due to discrete emission in Early-Type galaxies is thought to be mainly due to low-mass X-ray binaries. This is because in HMXBs the time taken by the massive companion of the neutron star to evolve from the neutron-star-forming supernova event to the end of the X-ray emitting phase is relatively short ($\sim 5 \times 10^6$ yr , van den Heuvel 1992). In LMXBs, on the contrary, this interval lasts $\sim 1 - 2 \times 10^9$ yr (Ghosh & White 2001). HMXBs are thus expected to

fade away shortly after the last relevant star formation event, while LMXBs survive much longer. In Early-Type galaxies star formation ended several Gyrs ago (§ 1.1) and very few (if any) HMXB are expected to be still present.

The spectral properties of the LMXBs population in Early-Type galaxies is still a matter of debate. The assumed spectra is usually a thermal bremsstrahlung with characteristic temperature ≥ 5 keV (e.g. Irwin, Sarazin & Bregman 2000). However studies of galactic LMXBs revealed that these objects may exhibit different spectral features. The physics of the accretion process, which is very complex and not fully understood, allows the presence of other components such as a multi-temperature blackbody spectrum, attributed to the accreting disk, or a power-law spectrum, due to IC scattering of the emitted photons in the dense environment surrounding the compact accreting object (e.g. La Parola et al. 2001; also see White, Nagase & Parmar 1995 for a review of the LMXBs spectral properties).

Sarazin, Irwin & Bregman (2001) found that a bremsstrahlung model with $kT \sim 8$ keV fits well the average spectra of X-ray sources in faint elliptical galaxies. However the X-ray luminosity function of LMXBs has a 'knee' at $L_x = 3.2 \times 10^{38}$ erg s^{-1}, and sources fainter than this limit have additional soft emission ($kT \sim 0.15$). The different spectra and the change in slope of the luminosity function may reflect difference in the emission mechanism due to the presence of a BH instead of a NS in the binary system. In fact, stellar evolution theories predict that the upper mass limit of a NS is ~ 1.4 M$_\odot$, since more massive objects undergo the gravitational collapse which creates a BH. Assuming equilibrium between the gravitational force acting on the infalling material and the radiative pressure, it is possible to calculate the 'Eddinghton luminosity', i.e. the maximum luminosity expected from the accreting material on a NS:

$$L_{Edd} \sim \frac{4\pi G M m_p c}{\sigma_T} = 1.3 \times 10^{38} \frac{M}{M\odot} \text{ erg s}^{-1} \tag{1.22}$$

where M is the mass of the accreting star, m_p is the mass of the proton, σ_T is the Thomson cross section. Thus, the 3.2×10^{38} erg s^{-1} luminosity is close to the upper limit expected from a 1.4 M$_\odot$ NS. Higher luminosities would destabilize the accretion flow and can be explained only taking into account relativistic effects associated with a BH (Fabbiano 1989, and references therein).

1.4. PHYSICAL STATUS OF THE HALO

The different luminosities observed in bright Early-Type galaxies, i.e. those where the main contribution to the X-ray flux comes from the hot halo, is believed to be due to the capability of the system to 'confine' the gas. Large galaxies are usually located at the bottom of the local gravitational well, often also due to their position at the center of clusters or groups of galaxies.

The X-ray data can be used to derive the physical properties of the hot emitting gas, such as central density, cooling times and total gaseous mass. They also allow to infer the total amount of matter (both luminous and dark) present in such systems and thus to test different galaxy formation scenarios and cosmological models. However we have seen in § 1.3.1 that we need to assume the distribution that characterizes the gas density. In this section we will describe some of these models and show how they can be used to define the physical status of the hot halo and the underlying total matter distribution.

1.4.1. Beta isothermal model

In general, elastic collision times for ions and electrons in the ISM are much shorter than the time scales for any heating, cooling or dynamical process that occurs in the galactic and cluster halos, so that the gas can be treated as a fluid (Sarazin 1988). Moreover, since the sound crossing time (i.e. the time for a sound wave in the ISM to cross the galaxy) is $t_s \sim 10^8$ yr and thus much smaller than the age of the galaxy of $\sim 10^{10}$ yr, the gas will be hydrostatic and the pressure will be a smoothly varying function of the position, unless very fast heating or cooling mechanisms are present. In this case:

$$\nabla P = -\rho_g \nabla \phi(r) \tag{1.23}$$

where $P = \rho_g kT/\mu m_p$ is the gas pressure[2], ρ_g is the gas mass density and $\phi(r)$ is the gravitational potential of the cluster. If the system is assumed to be spherically symmetric, equation (1.23) reduces to:

$$\frac{1}{\rho_g}\frac{\mathrm{d}P}{\mathrm{d}r} = -\frac{\mathrm{d}\phi}{\mathrm{d}r} = -\frac{GM(r)}{r^2} \tag{1.24}$$

where r is the radius from the galaxy center and $M(r)$ is the total cluster mass within r.

[2]Due to its high temperature and low density, the physical status of the ISM is very similar to that of an ideal gas.

The simplest distributions of gas temperatures is the isothermal one, i.e. $T_g(r) =$ constant. This distribution has been often used since temperature profiles based on low spectral resolution instruments seemed to be almost isothermal (e.g. Kim & Fabbiano 1995; Rangarajan et al. 1995; Jones et al. 1997). Although recent studies support the presence of multi-phase medium in the galactic halos (e.g. Buote 1999; Buote, Canizares & Fabian 1999; Buote 2000a), this remains a simple and useful model to derive the halo physical properties. If an isothermal distribution is assumed equation (1.24) becomes:

$$\frac{\mathrm{d}\ln\rho_g}{\mathrm{d}r} = \frac{\mu m_p}{kT_g}\frac{\mathrm{d}\phi(r)}{\mathrm{d}r} \tag{1.25}$$

In most models the galaxy potential is assumed to be that of a self-gravitating isothermal sphere (Chandrasekhar 1942; King 1966). Since this can not be represented exactly in terms of simple analytic functions, the King (1962) approximation is often used:

$$\rho(r) = \rho_0\left[1+\left(\frac{r}{r_0}\right)^2\right]^{-3/2} \tag{1.26}$$

$$\phi(r) = -4\pi\rho_0 r_0^2\frac{\ln[(r/r_0)+(1+(r/r_0)^2)^{1/2}]}{r/r_0} \tag{1.27}$$

where ρ is the total mass density, ρ_0 is the central total density and r_0 is the core radius of the distribution. These parameters are related to the line-of-sight velocity dispersion of test particles (e.g. the stars) by:

$$\sigma_r^2 = \frac{4\pi G\rho_0 r_0^2}{9} \tag{1.28}$$

(see Sarazin 1988 for a detailed derivation of this equation). The resulting gas distribution is given by (Cavaliere & Fusco-Femiano 1976):

$$\rho_g(r) = \rho_{g,0}\left[1+\left(\frac{r}{r_0}\right)^2\right]^{-3\beta/2} \tag{1.29}$$

Here

$$\beta = \frac{\mu m_p\sigma_r^2}{kT_g} \tag{1.30}$$

represents the ratio between the energy stored in stars to the one in the gas. This model is often referred to as **Beta model** in order to distinguish it from a true isothermal distribution (see discussion in Appendix C of Trinchieri, Fabbiano & Canizares 1986).

The X-ray surface brightness at a projected radius b, integrated over the whole spectrum, is then (Sarazin & Bahcall 1977, Gorenstein et al. 1978):

$$\Sigma(b,T_g) = \Lambda(T_g)\cdot\int n_e n_p \mathrm{d}l = \Sigma_0(T_g)\left[1+\left(\frac{b}{r_0}\right)^2\right]^{-3\beta+1/2} \tag{1.31}$$

where $\int n_e n_p \mathrm{d}l$ is the *emission measure* of the gas along the line-of-sight l through the galaxy, at projected radius b, and

$$\Sigma_0(T_g) = \Lambda(T_g)\sqrt{\pi}\left(\frac{n_e}{n_p}\right)\rho_{g,0}^2\ r_0\frac{\Gamma(3\beta - 1/2)}{\Gamma(3\beta)} \tag{1.32}$$

is the central surface brightness.

To determine the free parameters $\rho_{g,0}$ and r_0, that define the gas distribution in the Beta model, the usual approach is to fit the observed X-ray surface brightness profile with expression (1.31). β, instead, can be derived both by a surface brightness fit or through equation (1.30) if we know the gas temperature and the stellar velocity dispersion. To distinguish the two methods in the following chapters, we will adopt the symbol β when we refer to the brightness profile and β_{spec} for the spectral determination.

The surface brightness fits generally give $\beta \sim 0.4 - 0.6$ (e.g. Trinchieri, Fabbiano & Canizares 1986; Fabbiano & Schweizer 1995; Kim & Fabbiano 1995), although departures from a simple power law are quite common (see § 2.2.4). This suggests that the gas is generally hotter than the stars. However Matsushita (2001a) has recently shown, by means of spectral PSPC data, that this discrepancy is largely reduced if the Early-Type spectrum is modeled with two components: a thermal emission due to hot ISM plus a hard bremsstrahlung which models the contribution of discrete source. She obtains $\beta_{spec} \sim 1$ for faint galaxies, which means that the hot halo is probably heated by stellar mass losses. For brighter systems instead $\beta_{spec} \sim 0.5$, thus requiring additional heating. This is believed to be due to gravitational heating caused by the deep potential well which surrounds these galaxies.

Other heating mechanisms may be: supernova heating (Canizares, Fabbiano & Trinchieri 1987; Bertin & Toniazzo 1995), thermal conduction from the hotter Intra Cluster Medium (ICM) or, when nuclear radio sources are present, heating from relativistic electrons (Fabbiano 1989, and references therein).

1.4.2. Empirical Gas Distributions

The inconsistence of the isothermal Beta model for the brightest galaxies in clusters, discussed in the previous section, and the possible presence of multi-phase gas, has led to develop more empirical methods to derive the gas distribution.

Instead of assuming an a-priori model, the gas distribution can be derived directly from observations of the X-ray surface brightness. The X-ray surface brightness at a projected

distance b from the center of a spherical galaxy is:

$$\Sigma(b) = 2\int_b^\infty \frac{\epsilon(r)\mathrm{d}r}{\sqrt{r^2 - b^2}} \tag{1.33}$$

where ϵ is the X-ray emissivity defined in equation (1.5). This *Abell* integral can be inverted to give the emissivity as a function of radius (e.g. Binney & Tremaine 1987):

$$\epsilon(r) = -\frac{1}{\pi}\int_r^\infty \frac{\mathrm{d}\Sigma(b)}{\mathrm{d}b}\frac{\mathrm{d}b}{\sqrt{b^2 - r^2}}. \tag{1.34}$$

Because of the discretized nature of X-ray observations and the sensitivity of integral inversion to noise, the surface brightness data are often smoothed, either by fitting a smooth function to the observations or by applying this equation to the surface brightness averaged in rings about the galaxy center.

The emissivity ϵ is given by equation (1.5) and depends on the elemental abundances, the gas density and temperature. If the ISM abundances and temperatures are known (e.g. through spectral fits) equation (1.34) allows to determine the gas density $n_e(r)$ in the hypothesis that the gas is characterized by a single density and temperature at each radius. An iterative procedure which exploits this method has been developed by Kriss et al. (1983) and will be applied to our data in § 2.2.6, 3.2.3 and 4.2.6.

For the sake of completeness we notice that more general politropic models have also been employed to model the hot gas distribution (e.g. Killeen & Bicknell 1988). We will not discuss them here since they are not employed this work but more informations can be found in Sarazin (1988).

1.4.3. Total Mass Determination

Once the density and temperature distributions of the gas are known, it is possible to derive the total underlying mass distribution, in the hypothesis that the gas is in hydrostatic equilibrium. We have seen in § 1.4.1 that this is a reasonable assumption unless the galaxy is undergoing merger events or strong ram pressure stripping from the surrounding medium, and the gas motions remains subsonic.

If the gas is spherically distributed the hydrostatic equilibrium condition is expressed by equation (1.24). Combining it with the ideal gas law we obtain:

$$M(<r) = -\frac{rkT(r)}{\mu m_p G}\left(\frac{\mathrm{d}\log\rho_g}{\mathrm{d}\log r} + \frac{\mathrm{d}\log T}{\mathrm{d}\log r}\right) \tag{1.35}$$

where $M(< r)$ is the mass contained within r, T is the gas temperature, and $\mathrm{d}\log\rho_g/\mathrm{d}\log r$ and $\mathrm{d}\log T/\mathrm{d}\log r$ are respectively the logarithmic gradients of the gas density and temperature.

Equation (1.35) has been used by many authors to discover massive dark halos surrounding Early-Type galaxies with masses of $\sim 10^{13}$ $\mathrm{M}_\odot$ (Fabricant, Lecar & Gorenstein 1980; Kim & Fabbiano 1995; Jones et al. 1997, e.g). This method may be applied also when gas flows due to temperature gradients (see § 1.5) develop inside the halo, because dynamical timescales are long compared to the sound crossing time. However the resulting masses must be considered upper limits since it is possible that other mechanisms, such as the pressure of the ICM, may contribute to lower the mass required to confine the hot gas (Fabricant, Lecar & Gorenstein 1980; Vedder, Trester & Canizares 1988).

1.5. COOLING FLOWS

If the gaseous halos observed in Early-Type galaxies are in equilibrium with the gravitational potential of the galaxy, the energy released in the X-ray band is compensated by the energy acquired by gravitational infall, keeping the temperature constant and the gas in quasi-hydrostatic conditions. However, we have seen in § 1.3.1 that the thermal emissivity is proportional to the square of the density (equation 1.5). A reasonable approximation of the gas emissivity is (Sarazin 1988):

$$\epsilon \propto T^a n_e^2 \qquad \begin{cases} a = -1/2 & T < 3 \times 10^7 \text{ K} \\ a = 1/2 & T > 3 \times 10^7 \text{ K} \end{cases} \tag{1.36}$$

where T is the gas temperature and n_e is the electron density. This implies that in the center of the halo the gas cools more rapidly than in the outskirts, and its pressure drops. This process is not compensated by the drop in temperature, since below 3×10^7 K the emissivity is inversely proportional to the temperature and, however, the dependence on T is weaker than the one on density. The weight of the overlaying gas then causes a slow, subsonic inflow which is usually called "cooling flow".

The presence of cooling flows at the center of gaseous halos has been proposed since the *cooling times* τ_c in the central regions of most galaxies are smaller than the Hubble time (i.e. the epoch of galaxy formation). For an isobaric transformation (Fabian et al. 1981):

$$\tau_c = \frac{5}{2} \frac{nkT}{n_e n_p \Lambda} \tag{1.37}$$

where $n = m_p + n_e$ is the total number density. Typical cooling times in the center of Early-Type galaxies are $\leq 10^8$ yrs (see for instance Canizares, Fabbiano & Trinchieri 1987).

Even if no direct proof of the presence of cooling flows exist, such as the Doppler shift of X-ray emission lines (the spectral resolution of modern detectors are still too low to measure these slow motions), X-ray observations have allowed to discover both imaging and spectroscopic indirect evidences: a) X-ray images of bright Early-Type galaxies show a strong central emission peak, which is attributed to the emission of the dense cooling component in the galaxy core; b) the gas temperatures inferred from spectral analysis revealed a central drop[3], explained with the presence of cooler gas (Fabian 1994, and references therein).

If a steady-state spherical flow develops in the halo, we can derive the amount of mass deposited in the galaxy center from the flow equations (Fabian & Nulsen 1977; Binney &

[3]The isothermal models discussed in § 1.4.1 are still a reasonable approximation of the gas distribution since the temperature drop affects only the central regions of the halo.

Cowie 1981; Canizares, Stewart, & Fabian 1983):

$$\dot{M} = 4\pi r^2 \rho_g^2 \Lambda(T) \left\{ \frac{\mathrm{d}}{\mathrm{d}r} \left[\frac{5}{2} \frac{kT}{\mu} + \phi(r) \right] \right\}^{-1} \tag{1.38}$$

and compare it with the observed central X-ray peak. This kind of comparisons have shown that the central brightness excess is much smaller than the one expected if all the cooling mass reached the galaxy center. Moreover observations at other wavelengths have shown no evidence of the presence of the accreted material. This suggests that the cool material does not remain in the gaseous phase but cools enough to form stars. However this would result in a bluer color of the Early-Type core, which is not seen. To avoid this problem some authors have proposed that the star formation process creates low-mass objects that are more difficult to detect.

Alternative scenarios consider the possibility that the steady-state cooling flow model is wrong, and the gas does not reach the galaxy center but is deposited throughout the galaxy at all radii. This hypothesis is supported by the fact that the mass deposition profiles derived by many X-ray studies are not constant (as would be expected in a steady-state flow) but are proportional to the galactocentric radius: $\dot{M} \propto r$ (e.g Bertin & Toniazzo 1995; Kim & Fabbiano 1995; Rangarajan et al. 1995; Matsushita et al. 2001b).

If cool material is deposited throughout the halo we expect to see multiphase gas. In fact recent observations suggest that multi-temperature models fit better than single-temperatures ones the observed X-ray spectra of ASCA and ROSAT (Buote 1999; Buote, Canizares & Fabian 1999; Buote 2000a; Makishima et al. 2001). However the cooling-flow models are now in serious troubles since recent studies with XMM found no evidence of multi-phase gas and showed that, in several cases, a lower temperature cutoff must be introduced in the cooling flow models to explain the observed spectra (Peterson et al. 2001; Kaastra et al. 2001; Tamura et al. 2001). The latter point requires the presence of additional heating sources, such as a high supernova rate or an active nucleus, to prevent the gas from cooling.

Finally there are evidences that the hot halo structure is more related to the shape of the gravitational well, than to the presence of a central cooling flow (Makishima et al. 2001; Matsushita 2001a; Matsushita et al. 2001b). In faint Early-Type galaxies the halo temperature seems to be compatible with stellar mass-loss heating, while in brighter galaxies there is an additional extended component that may be produced by a large amount of dark matter in the galaxy outskirts.

1.6. ENVIRONMENTAL EFFECTS

The dependence of galaxy properties on the environmental conditions is a well established fact. Optical studies have shown that galaxy morphology is strongly dependent on the density of galaxies in the sense that while Early-Type galaxies represent the dominant morphological class in groups and clusters of galaxies, Late-Types are more common in low density environments (e.g. Bahcall 1996). The galaxy luminosity function has a steeper slope in denser environments, thus indicating that different evolutionary processes are at work (e.g. Trentham 1998; Christlein 2000). Moreover giant and cD ellipticals are only found in the center of rich systems. Even if it is not clear which are the main parameters (e.g. local density, total density of the cluster, distance from cluster center) that play a fundamental role, it is generally accepted that galaxy encounters, merging and interaction with the ICM are all processes that must affect the properties of galaxies to some extent.

It is thus not surprising that environmental effects may be suspected to contribute in determining also the X-ray properties of galaxies. Although there are several suggested mechanisms by which the environment may affect the X-ray halo of a galaxy, the actual role that these effects play is unclear. Ram-pressure stripping is likely to remove gas from galaxies passing through a dense intra-cluster medium (Gunn & Gott 1972), and turbulent viscous stripping may be as effective in the group environment (Nulsen 1982). It is also likely that the ICM provide reservoirs of gas which can be captured by slow moving or stationary galaxies.

However the observational evidence is conflicting and often difficult to interpret. For instance White & Sarazin (1991) found that, for a sample of Early-Type galaxies observed with *Einstein*, galaxies with $\log L_x/L_B < 30$ erg s^{-1} L$_B^{-1}$ had $\sim 50\%$ more neighbors than X-ray bright galaxies. They attribute this to ram pressure stripping, which would be expected to reduce L_X more in higher density environments. An opposite view was presented by Brown & Bregman (2000), who found that L_X/L_B increased with environmental density. Their explanation is that for the majority of galaxies ram-pressure stripping is a less-important effect than the stifling of galactic winds by a surrounding ICM. In this model the ICM encloses the galaxy, increasing the gas density of its halo and therefore its X-ray luminosity.

Brown & Bregman (1998) claimed an environmental dependence based on a correlation between L_X/L_B and Tully density parameter ρ (Tully 1988) for their sample. However, Helsdon et al. (2001) show that group dominant galaxies often have X-ray luminosities which are more related to the properties of the group than of the galaxy. Their high luminosities are more likely to be caused by a group cooling flow than by a large galaxy halo. Once these objections are removed from consideration, the correlation between L_X/L_B and ρ becomes

very weak.

In a large ROSAT PSPC sample, O'Sullivan, Forbes & Ponman (2001) found no evidence of a correlation between L_X/L_B and the environmental density, while the similarity of the L_X/L_B relation in field, groups and clusters suggest that the environment does not change the properties of the whole population. They notice that their result does not mean that there are no effects on the X-ray properties of galaxies but that none of the processes affecting the X-ray halos is dominant or that they counter-balance each other.

Numerical simulations generally suggest strong environmental influence on the X-ray halo properties. Toniazzo & Schindler (2001) showed that interaction with the ICM may produce large fluctuations of the halo luminosity, depending on the galaxy orbit through the cluster. If the galaxy moves at supersonic speeds ram pressure stripping is very effective in removing large quantities of gas from the halo, while slow subsonic motions allow the galaxy to accumulate the gas produced by stellar mass losses. Such variation in halo gas content during the galaxy orbit is large enough to explain the observed scatter in X-ray luminosities. D'Ercole, Recchi & Ciotti (2000) studied tidal interactions in elliptical galaxies, showing that tidal stripping may produce strong fluctuations in the halo shape and luminosity, as well as removal of hot gas from the galaxy outskirts. Barnes (2000) further showed that such encounters may produce deformations of the X-ray halo and profile.

Finally the location of the larger X-ray halos, associated with giant and cD ellipticals, at the center of groups and clusters of galaxies indicates that the structure of the gravitational potential well must play an important role in retaining the hot gas. As already discussed in the previous section, this scenario is supported by recent works by Makishima et al. (2001) and Matsushita (2001a) which stress the fact that the properties of most massive system are mainly due to the presence of large potential structures.

Chapter 2

NGC 1399

2.1. INTRODUCTION

NGC 1399 is the central dominant galaxy of the Fornax cluster. Due to its proximity (19 Mpc for $H_0 = 75$ km s^{-1} Mpc^{-1}), this very regular, almost spherical (E0; Ferguson 1989) cD galaxy has been extensively studied in a wide range of wavelengths, ranging form radio to X-rays. The optical radial profile, first studied by Schombert (1986) and later in more detail by Killeen & Bicknell (1988), reveals a large halo extending up to 250 kpc. The galaxy is surrounded by a large number of globular clusters, 10 times in excess with respect to those of its nearer companion NGC 1404 and of the Fornax galaxy NGC 1380 (Kissler-Patig et al. 1999). Dynamical studies of the stellar population of NGC 1399 indicate that the central regions of the galaxy are characterized by a high velocity dispersion, decreasing with radius, and slow rotation, as expected in giant ellipticals (Graham et al. 1998). At larger radii the velocity dispersion starts increasing again, as shown by studies of the planetary nebulae (Arnaboldi et al. 1994) and globular clusters dynamical properties (Grillmair et al. 1994). This suggests a different dynamical structure, than that of the inner stellar body, for the galaxy envelope and the globular cluster population.

NGC 1399 hosts a weak nuclear radio source (Killeen, Bicknell & Ekers 1988) with radio luminosity of $\sim 10^{39}$ ergs s^{-1} between 10^7 and 10^{10} Hz. The radio source has two jets ending in diffuse lobes, confined in projection within the optical galaxy. Killeen, Bicknell & Ekers (1988) suggest that the radio source is intrinsically small and confined by the thermal pressure of the hot ISM.

X-ray data have shown the presence of an extended hot gaseous halo surrounding NGC 1399. Observations made with the *Einstein* IPC by Kim, Fabbiano & Trinchieri (1992a)

constrained the gas temperature to be $kT > 1.1$ keV. The *Einstein* IPC data were used also by Killeen & Bicknell (1988) to derive the mass distribution of the galaxy. They found that both models with and without dark matter were compatible with those data, depending on the assumed temperature profile. White (1992) suggested the presence of a cooling flow in the center of the galaxy, depositing 0.8±0.6 $M_\odot$ y^{-1}. *Ginga* observations (Ikebe et al. 1992) led to the detection of extended emission out to a galactocentric radius of ∼250 kpc. Serlemitsos et al. (1993) constrained the X-ray temperature to be $1.0 < kT < 1.5$ keV with the Broad Band X-ray Telescope (BBXT). Rangarajan et al. (1995, hereafter RFFJ), using the ROSAT PSPC, have studied in detail the temperature profile of the hot inter-stellar medium (ISM) out to 220 kpc finding an isothermal profile ($0.9 < kT < 1.1$) from 7 to 220 kpc, and a central cooling flow ($0.6 < kT < 0.85$) of at least 2 $M_\odot$ y^{-1}.

Ikebe et al. (1996) were able to identify with ASCA the presence of different components in the X-ray halo, associated respectively with the galaxy and the Fornax cluster potential. Jones et al. (1997) used the better resolution of the ROSAT PSPC for studying in detail the cluster X-ray structure and finding a total binding mass of (4.3-8.1)$\times 10^{12}$ $M_\odot$ within 100 kpc, with a mass-to-light ratio increasing from 33 $M_\odot/L_\odot$ at 14 kpc to 70 $M_\odot/L_\odot$ at 85 kpc. They also found a metal abundance of 0.6 solar. Buote (1999) analyzed ASCA data finding that either a two temperature spectral model or a cooling-flow model with solar Fe abundances, are required to fit the thermal X-ray emission, and additional absorption is needed in the galaxy center. Matsushita, Ohashi & Makishima (2000) found similar near solar metallicities but argued that the metallicity inferred by ASCA spectral fits is dependent on the assumed atomic physics model and is not solved by multi-components spectral models.

More recently Sulkanen & Bregman (2001) used ROSAT data to pose an upper limit on the nuclear source brightness. The *Chandra* data were used by Loewenstein et al. (2001) to further constrain the nuclear source and by Angelini, Loewenstein & Mushotzky (2001) to study the point source population hosted by globular clusters.

In this chapter we present the results of a deep observation of the NGC 1399/NGC 1404 field obtained from data collected between 1993 and 1996 with the ROSAT High Resolution Imager (HRI, for a description see David et al. 1996). We take advantage of the ∼ 5" resolution of the HRI to study in detail the structure of the galactic halo and relate the results to those obtained at larger scales with poorer resolution instruments. We study the interactions between the nuclear radio source and the galactic halo and discuss the properties of the discrete sources population. A preliminary analysis of *Chandra* data supports the ROSAT results.

We adopt $H_0 = 75$ km s^{-1} Mpc^{-1} and a distance of 19 Mpc (1'=5.5 kpc).

2.2. OBSERVATIONS AND DATA ANALYSIS

The NGC 1399 field, including NGC 1404, was observed at three separate times with the ROSAT HRI: in February 1993, between January and February 1996 and between July and August of the same year. The total exposure time is 167.6 ks (Table 2.1). The data were processed with the SASS7_8 and SASS7_9 versions of the ROSAT standard analysis software (SASS). For our data analysis, we used the IRAF/XRAY and CIAO packages developed at the Smithsonian Astrophysical Observatory and at the *Chandra* X-ray Center (CXC), and other specific software as mentioned in the text.

Table 2.1: ROSAT HRI observations of NGC 1399.

name	Field center		sequence id.	Exp.time	obs. date	P.I.[a]
	R.A.	Dec		(sec)		
NGC 1399	$03^h38^m31^s$	–35°27'00"	RH600256n00	7265	1993 Feb 17	D.-W. Kim
"	"	"	RH600831n00	72720	1996 Jan 04-1996 Feb 23	G. Fabbiano
"	"	"	RH600831a01	87582	1996 Jul 07-1996 Aug 26	G. Fabbiano

[a] Principal Investigator

2.2.1. Aspect Correction

The HRI data processed with the SASS versions prior to SASS7_B of March 1999 (as it happens for our data) suffer from an error in the aspect time behavior (Harris 1999). This translates into an error on the position of the incoming photons and thus it results in a degradation of the Point Response Function (PRF). Because high resolution analysis is the primary objective of this work we run the correction routine ASPTIME (F. Primini 2000, private communication) on the data, to improve the aspect solution. Visual inspection of the brightest pointlike sources in our field (Figure 2.1) demonstrates the improvement in the image quality.

Additional problems that may preclude the attainment of the HRI potential resolution are the imperfect correction of the spacecraft wobble and the wrong tracking of reference stars due to the variable pixel sensitivity across the detector (Harris et al. 1998). We followed the procedure suggested by Harris and collaborators, of dividing the observations in time

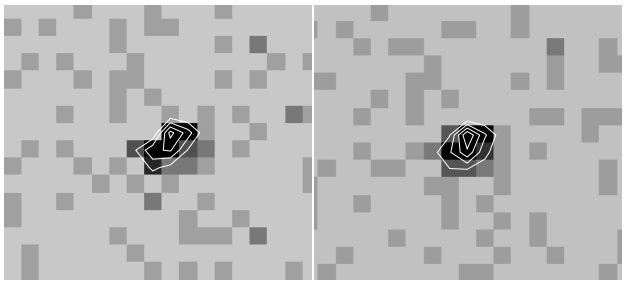

Fig. 2.1.— Comparison between the aspect of the brightest pointlike source in the NGC 1399/1404 field (No.8 in Table 2.3) before (left) and after (right) correction. The pixel size is 4". Contour levels are spaced by 5.9×10^{-2} cnts arcmin^{-2} s^{-1} with the lower one at 6×10^{-2} cnts arcmin^{-2} s^{-1}.

bins (OBI) and realigning these segments by using the centroids of a reference pointlike source in each OBI.

Our data can be divided in 4 OBIs in RH600256n00, 43 in RH600831n00 and 33 in RH600831a01. We checked each OBI individually using the brightest point source in the field (No.8 in Table 2.3). We found that in the first observation (RH600256n00) the OBI are well aligned and no correction is needed. The second observation (RH600831n00) has 7 OBIs out of 43 that are 7"-10" displaced; however, the overall PRF is 6" FWHM so that just a slight improvement can be obtained dewobbling the image. The third observation (RH600831a01) has a 8" PRF but the signal to noise ratio of the individual OBIs is worse than in the previous observations so that the dewobbling procedure cannot be applied. Given these results, we decided not to apply the dewobbling correction, and to take as good a resulting PRF, in the composite image, of $\simeq$7" FWHM.

2.2.2. Composite Observation and Exposure Corrections

The aspect-corrected observations were co-added to obtain a "composite observation". To make sure that pointing uncertainties did not degrade the image we used the centroids of three bright pointlike sources in the field (No.8, 19 an 24 in Table 2.3) to align the images. The applied corrections were all within 2 arcsec. The resulting composite image is shown in Figure 2.2. This image was then corrected for vignetting and variations of exposure time and quantum efficiency across the detector by producing an "exposure map" for each observation with the software developed by Snowden et al. (1994, hereafter SMB).

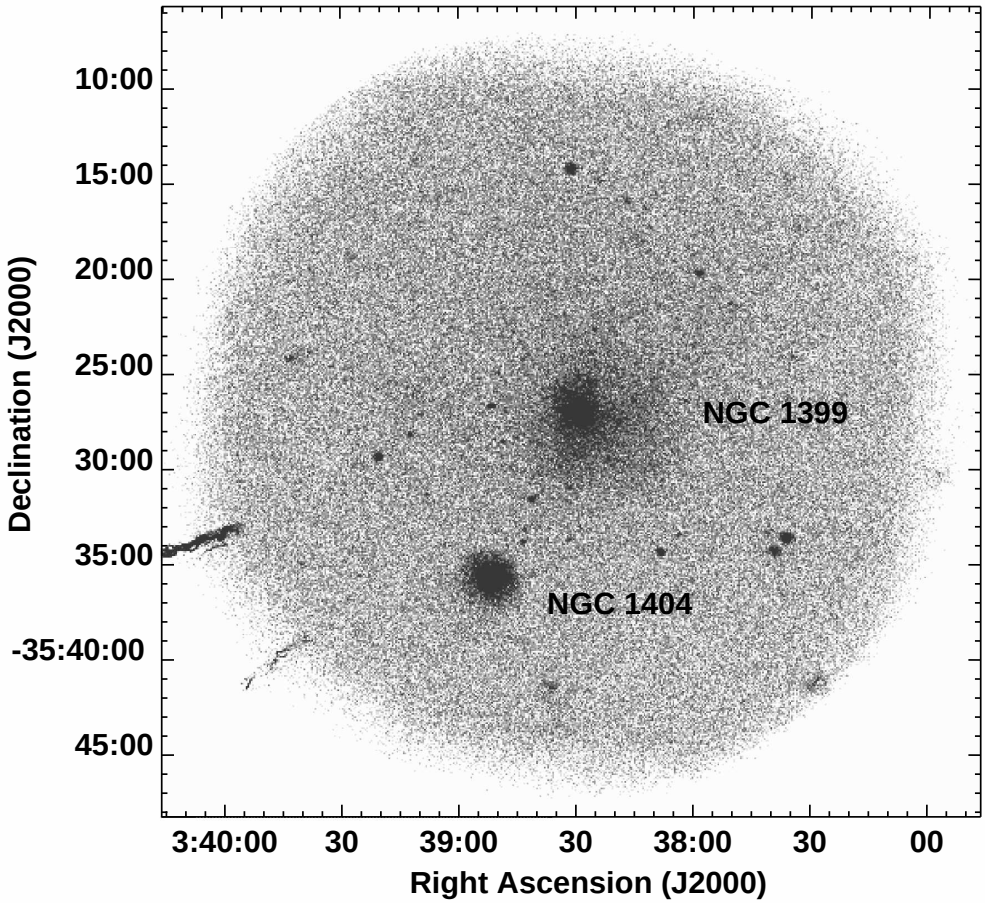

Fig. 2.2.— The 'raw' NGC 1399/NGC 1404 HRI field. The composite image is here displayed after it was rebinned to 5 arcsec/pixel. Even without exposure correction the extended emission surrounding NGC 1399 is clearly visible. The elongated features in the lower left corner are due to the presence of "bad pixels" on the detector. North is up and East is left.

2.2.3. Surface Brightness Distribution and X-ray/Optical Comparison

To study the large-scale brightness distribution of the NGC 1399 field we rebinned the exposure corrected data in 5”×5” pixels. We then adaptively smoothed the image with the CXC CIAO *csmooth* algorithm which convolves the data with a gaussian of variable width (depending on the local signal to noise range of the image) so to enhance both small and large scale structures.

The resulting image (Figure 2.3a) shows a complex X-ray morphology. The center of the image is occupied by the extended halo of NGC 1399. The galaxy possess a central emission peak and an external extended and asymmetric halo. This halo is not azimuthally symmetric with respect to the X-ray peak, but it extends more on the SW side. The X-ray surface brightness distribution of the halo appears filamentary, with elongated structures and voids. As it can be seen from a comparison with the optical Digitized Sky Survey (DSS) image (Figure 2.3b), while the X-ray emission peak is centered on the optical galaxy, the X-ray halo extends radially much further than the optical distribution. Moreover most of the features seen in the X-ray image have no direct optical counterpart. The SW clump centered at RA, Dec=$3^{h}38^{m}12^{s}$,–35°30’00” and the one at $3^{h}39^{m}12^{s}$,–35°26’12” were also detected by the wavelets algorithm (sources No.42 and 43 in Table 2.3 and Figure 2.19) presented in § 2.2.9.

A number of pointlike source in the field is visible in Figure 2.3a. The analysis of these sources is discussed in § 2.2.9. The X-ray emission of NGC 1404, instead, will be discussed in detail in Chapter 3.

We examined the inner halo of NGC 1399 in greater detail using a 1”/pixel resolution. The adaptively smoothed image (Figure 2.4) reveals an elongation of the inner halo structure in the N-S direction plus a large arc protruding to the West side of the halo. Several voids are present in the X-ray distribution, the largest being 1.5 arcmin NW of the emission peak. The central peak appears circular with at most a slight N-S elongation.

These features are all above 3σ significance, since 3σ was the minimum significance level requested for an intensity fluctuations to be smoothed on a given scale. We can rule out that features on scales of 1 arcmin are of statistical nature, because their significance can be as high as 6σ (see § 2.2.5). These brightness fluctuations must be due to the local physical conditions of the hot gaseous halo.

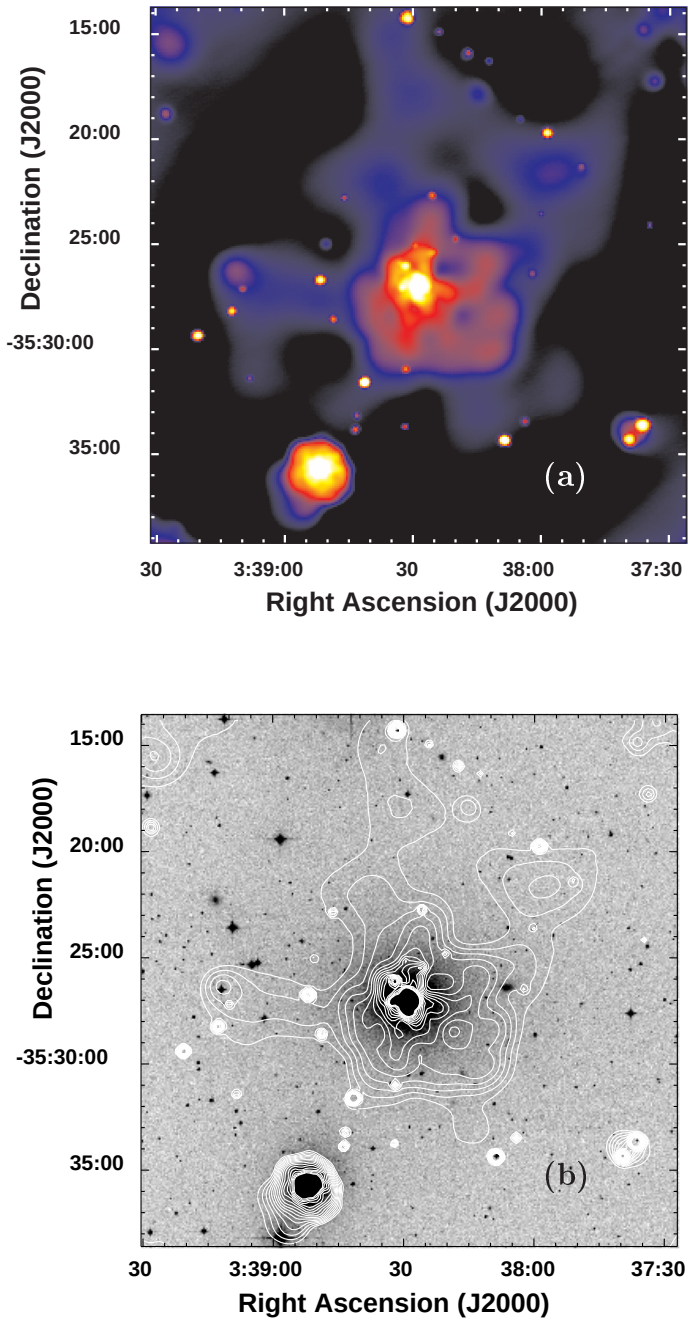

Fig. 2.3.— **(a)** 5×5 arcsec/pixel adaptively smoothed image of the central part of the NGC 1399/1404 HRI field. Colors from black to yellow represent logarithmic X-ray intensities from 5.6×10^{-3} to 3.58×10^{-1} cnts arcmin^{-2} s^{-1}. **(b)** X-ray brightness contours overlaid on the 1 arcsec/pixel DSS image (logarithmic grayscale). Contours are spaced by a factor 1.1 with the lowest one at 6.1×10^{-3} cnts arcmin^{-2} s^{-1}. The X-ray emission peak is centered on the optical galaxy for both NGC 1399 and NGC 1404. In the case of NGC 1404 the X-ray isophotes are consistent with the optical distribution while in NGC 1399 the X-ray emission extends further out than the optical one.

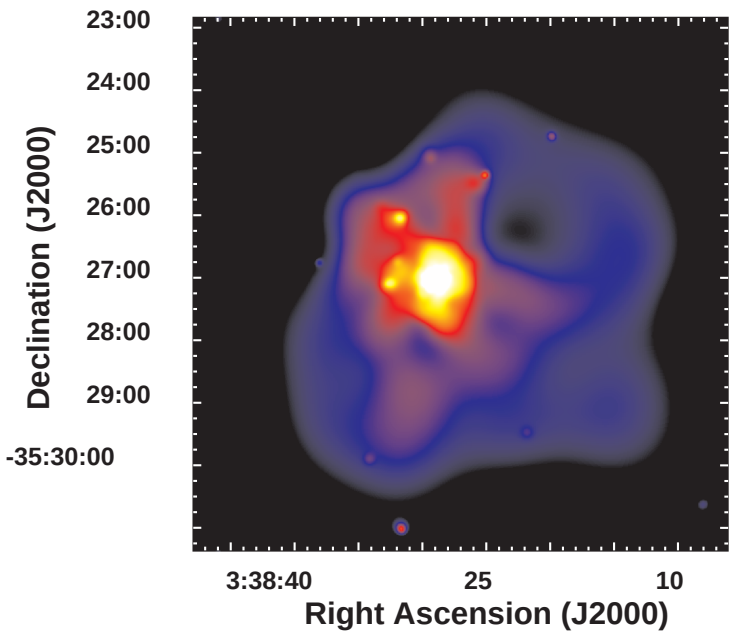

Fig. 2.4.— Adaptively smoothed image of the inner NGC 1399 halo. Colors from black to yellow represent logarithmic X-ray intensities from 6.4×10^{-3} to 7.7×10^{-1} cnts arcmin^{-2} s^{-1}.

2.2.4. Radial Brightness Profiles

As a first step in the quantitative study of the X-ray emission, we created a radial profile from the HRI data, assuming circular symmetry. Count rates from the exposure-corrected composite image, were extracted in circular annuli centered on the X-ray centroid RA, Dec=$3^{h}38^{m}28^{s}.9$, –35°27”02’.1. We took care to remove the contribution of all the detected point-like sources by excluding circles within the 3σ radius measured by the wavelets algorithm (§ 2.2.9), from the source centroid[1]. We also excluded a 150” circle centered on NGC 1404 (see § 3.2.2).

The X-ray brightness profile is shown as a continuous line in Figure 2.5. The emission extends out to $\sim$ 500” (46 kpc at the assumed distance of 19 Mpc). The radial profile flattens out past 500” (dash-dotted line in Figure 2.5) suggesting that we have reached the field background level and that any residual halo emission is below our sensitivity limit. Nevertheless we know from previous investigations of the Fornax cluster with *Ginga* (Ikebe

[1]The counts in each annulus are renormalized to the net observed area by the extraction procedure.

et al. 1992), *Einstein* (Killeen & Bicknell 1988) and ROSAT (Jones et al. 1997), that extended X-ray emission, bright enough to be detected in our data, is present at galactocentric radii $> 500''$. We thus expected to see a smooth gradient in the X-ray profile continuing past 500". We checked to see if a very high background was present in some OBIs or either in some of the HRI spectral channels[2] but we found none that could explain our lack of sensitivity. A possible explanation is that we didn't reach the background level around 500" and the actual background is much lower but, due to uncertainties in the exposure correction near the edge of HRI field of view, we are not able to see the expected decline in the X-ray emission.

We used the SMB software to calculate a background map for this field. The radial profile derived from this background map is shown as a small dashed line in Figure 2.5. The SMB model however may underestimate the "true" HRI background somewhat because it models only the charged particle contribution. We therefore corrected this value using the 52 ks ROSAT PSPC observation RP600043N00 centered on NGC 1399, taken on the 1991 August 15 (Figure 2.6). Even if the PSPC observation is much shorter than our HRI image, the higher sensitivity and lower background of this instrument allows a better study of the large scale X-ray emission.

The exposure corrected PSPC profile is shown in Figure 2.7. The background level (dashed line) was estimated from the 2400"-3000" annulus. We compared our radial profile to the one derived by Jones et al. (1997) and RFFJ, who made use of the same data, finding consistent results. We then rescaled the SMB background to find the best agreement between HRI and PSPC counts in the 50-400 arcsec region, after rebinning the HRI data to match the wider PSPC PRF. The "true" HRI background level found in this way (long-dashed line in Figure 2.5) lies in between the flattening level of the HRI profile and the SMB background and was used to derive the HRI background-subtracted profile shown as empty circles. This way of finding the HRI background assumes that the PSPC brightness profile is not affected by systematic errors on the background determination and can thus be used to rescale the HRI counts. However, even if the PSPC background suffered from residual errors (e.g. due to uncertainties in the exposure correction at large radii), they would not significantly affect the central region profile – used to rescale the SMB HRI background – because there the X-ray brightness is one order of magnitude larger than the PSPC background level.

The HRI radial surface brightness profile has a complex structure. In the 'central' region, i.e. within 50" from the emission peak, the X-ray emission is well represented by a simple Beta model (equation 1.31) with best fit parameters $r_0 = 3.93 \pm 0.16$ arcsec, $\beta = 0.506 \pm 0.003$

[2]The ROSAT HRI has 11 spectral channels. The spectral accuracy is too low to perform a reliable analysis but can be used to check for instrumental problems.

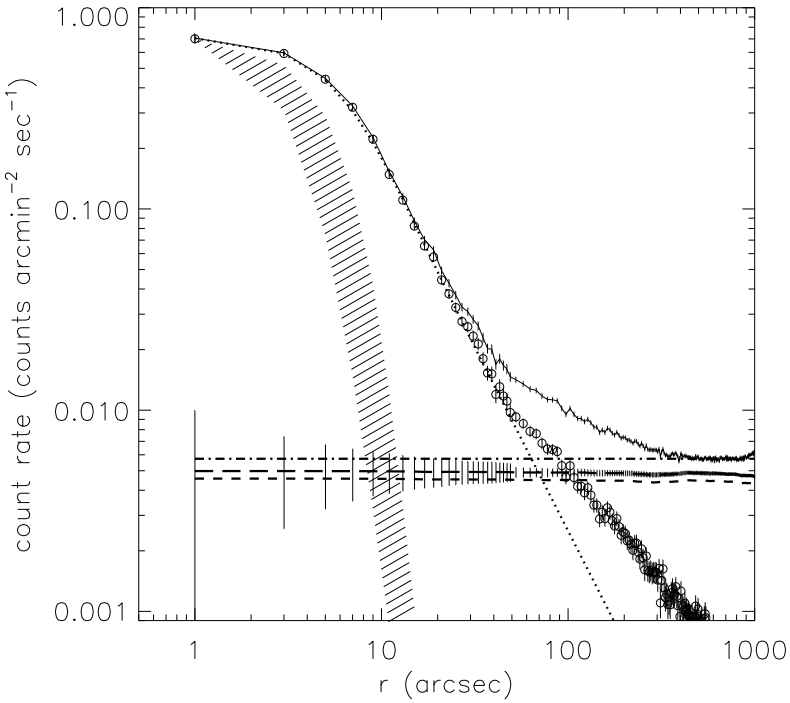

Fig. 2.5.— HRI radial profile of NGC 1399 X-ray surface brightness (continuous line) after excluding all point sources (§ 2.2.9) and NGC 1404. The dot-dashed line represents the flattening level of the HRI profile measured in the 500"-850" annulus. Short and long dashed lines represent respectively the SMB background level before and after rescaling to match PSPC counts. The rescaled background was used to derive the background-subtracted counts (open circles) and the best-fit Beta model within 50" shown in Figure 2.8 (dotted line). The HRI PRF range is represented by the shaded region. Radial bins are 2" wide up to r=50", and 5" wide at larger radii.

and $\chi^2 = 14.5$ for 22 degrees of freedom (Figure 2.8). To determine the best fit parameters the model was convolved with the HRI on-axis PRF (David et al. 1996). At radii larger than 1 arcmin the surface brightness profile shows a significant excess over this model (see Figure 2.5), indicating the presence of an additional 'galactic' component. Restricting the fit to r < 40" to check if this more extended component contributes around 50", gives consistent results with $r_0 = 3.88^{+0.20}_{-0.16}$ arcsec and $\beta = 0.504^{+0.004}_{-0.003}$ ($\chi^2 = 11$ for 17 degrees of freedom). Thus, for 3" $< r <$ 50" the X-ray emission falls as $r^{-2.04\pm0.02}$. As can be seen by the comparison with the HRI PRF (shaded region in Figure 2.5), whose uncertainty is due to residual errors in the aspect solution (David et al. 1996), the central component is extended and cannot be due to the presence of a nuclear point source, that in fact is not detected in our data (see §

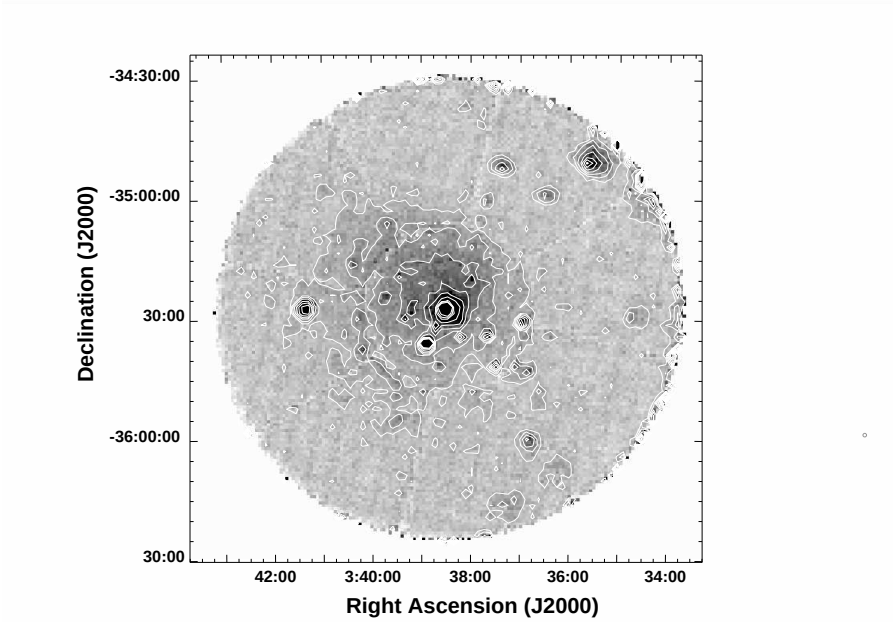

Fig. 2.6.— Exposure corrected PSPC image of the NGC 1399/1404 field. The two brightest central emission peaks represent the two galaxies (NGC 1399 and NGC 1404) visible also in the HRI field. X-ray contours, spaced by a factor of 1.3 with the lowest level at 3.5×10^{-3} cnts arcmin^{-2} s^{-1}, clearly show the presence of an extended halo much larger than the HRI FOV (central 40×40 arcmin). The black line delimits the two sectors used to extract the radial profiles shown in Figures 2.9a, b. Radial ribs are due to the PSPC support structure.

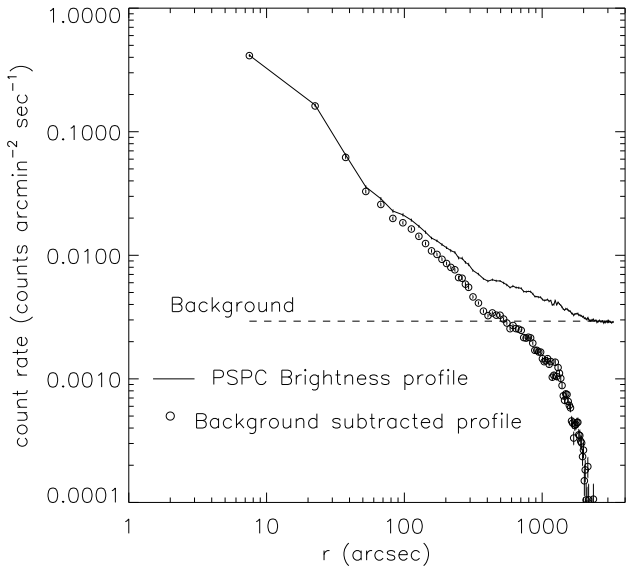

Fig. 2.7.— Exposure corrected PSPC radial profile of NGC 1399 (continuous line). The dashed line represents the background level measured in the 2400-3000 arcsec region, used to derive the background-subtracted counts (open circles). The X-ray halo clearly extends at much larger radii than visible in the HRI FOV but the central region is not well resolved due to the larger PRF.

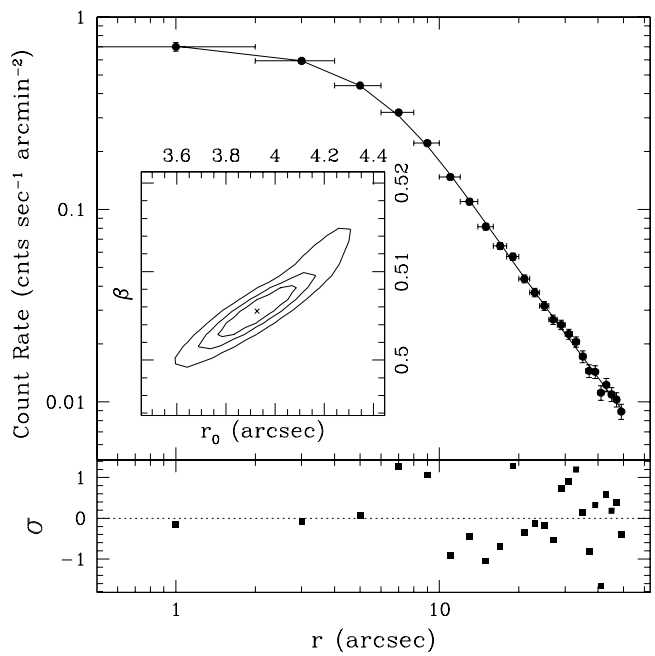

Fig. 2.8.— The best-fit model and the residuals of NGC 1399 brightness profile within 50". The 66%, 90% and 99% contour levels relative to the core radius r_0 and slope β are shown in the inner panel.

2.2.8).

The PSPC profile in Figure 2.7 shows that X-ray emission extends to much larger radii than visible in the HRI data and suggests the presence of a third component dominant at $r > 400$". Large azimuthal differences are seen in the X-ray profile at radii larger ~ 1 arcmin. We derived composite HRI-PSPC X-ray profiles in two sectors dividing the images along the line connecting the X-ray centroids of NGC 1399 and NGC 1404: a NE sector (Position Angle: 331.5° <P.A.< 151.5°) and a SW sector (151.5° <P.A.< 331.5°). While the emission within 1 arcmin is azimuthally symmetric, the galactic component ($r > 1'$) is much more extended in the SW direction and presents a steep decline in the NE sector, as suggested by Figures 2.3a and 2.4. The even more extended component visible in the PSPC data follows the opposite behavior, being 3 times brighter around 1000" on the NE side than on the SW one. While these asymmetries have been reported by Jones et al. (1997), their PSPC data alone do not have enough resolution to clearly separate the central component from the external halo. Jones and collaborators used a single power-law model to fit the whole distribution, thus obtaining a value of ∼0.35 for the power law slope.

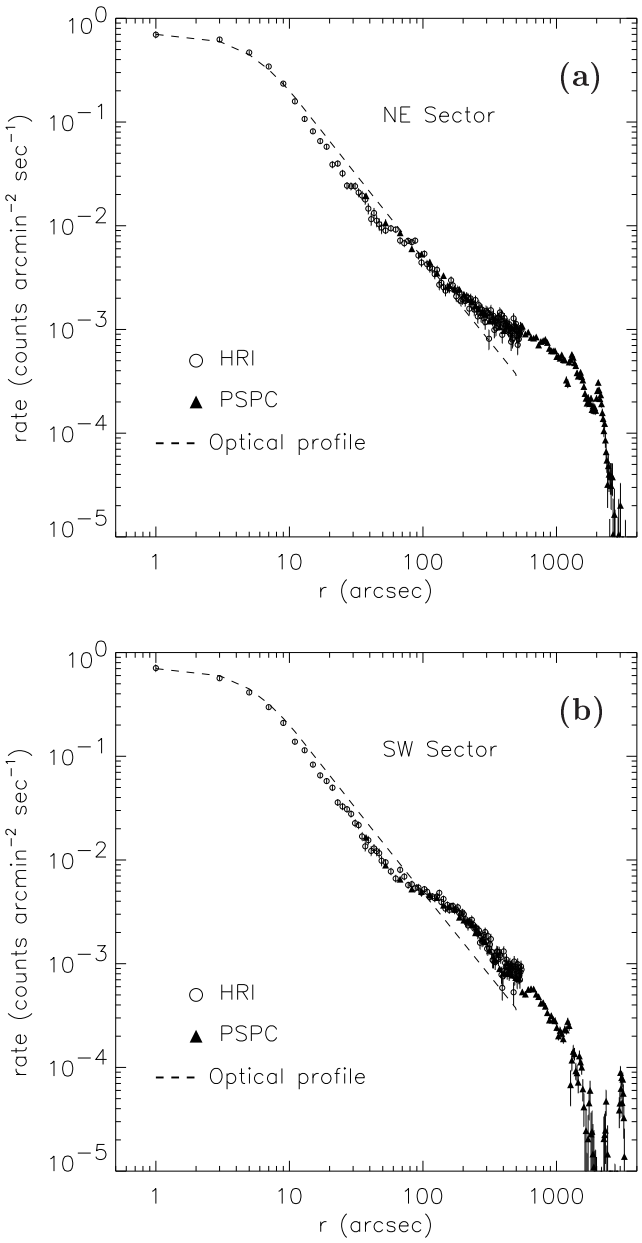

Fig. 2.9.— Background subtracted radial profile of NGC 1399 in the NE (a) and the SW (b) sectors. Open circles represent HRI data (2" annuli for $r < 50$", 5" for $r > 50$"), while filled triangles represent PSPC data (15" annuli for $r < 300$", 30" for $r > 300$"). PSPC counts are reduced by a factor ~ 0.3 to match the HRI profile; the inner 30" are not shown because of the lower resolution. The dashed line represents the optical profile (convolved with the HRI PRF) from Killeen & Bicknell (1988).

2.2.5. Bidimensional Halo Models

Because of the complex halo structure it is not possible to obtain a satisfactory fit of the entire surface brightness distribution of NGC 1399 with a single circularly symmetric model. The *Sherpa* modeling and fitting application of the CIAO package allows us to adopt a more realistic approach: we added together three models to represent the different components seen in the surface brightness profile (Figures 2.5 and 2.7). Moreover, to take into account the deviations from circular symmetry (Figures 2.9a and 2.9b), each component is represented by a bidimensional extension of the classical Beta model (equation 1.31) of the form:

$$\Sigma(x,y) = \frac{A}{(1+(r/r_0)^2)^{3\beta-0.5}} \tag{2.1}$$

where

$$r(x,y) = \frac{x_{new}^2(1-\epsilon)^2 + y_{new}^2}{1-\epsilon} \tag{2.2}$$

and

$$x_{new} = (x-x_0)\cos(\theta) + (y-y_0)\sin(\theta) \tag{2.3}$$

$$y_{new} = (y-y_0)\cos(\theta) - (x-x_0)\sin(\theta). \tag{2.4}$$

Here x_{new} and y_{new} correspond to the position of the X-ray centroid, $\epsilon = 1 - \frac{\text{minor axis}}{\text{major axis}}$ is the ellipticity and θ the Position Angle.

The final bidimensional model has to be fitted directly on the X-ray images, rather than on the radial profiles (as done in Figure 2.5). To exploit both the HRI spatial resolution (to sample the halo core) and the large PSPC FOV (to include the large-scale components) we had to fit the HRI and the PSPC data simultaneously. However, at the time this work was in progress, the CIAO package didn't allow to fit two datasets at the same time. Thus we used the following iterative procedure: **(a)** we rebinned the HRI image in 15"×15" pixels, in order to have enough counts per pixel to fit the galaxy halo and to smooth out small scale asymmetries; NGC 1404 and all the detected point-like sources (§ 2.2.9) were masked out before performing the fit. **(b)** The PSPC data were rebinned in 45"×45" pixels; the regions containing the support structure where masked, together with all the sources detected in the HRI field. Because the PSPC field of view (FOV) is larger than the HRI one, to mask all the remaining PSPC sources we used the source parameters measured by the wavelets algorithm in the context of the GALPIPE project (Mackie et al. 1996, and references therein), which has produced a list of all sources present in the ROSAT PSPC archive[3]. **(c)** We built a

[3]An online version of the GALPIPE database and documentation can be found at the D.I.A.N.A. homepage at the Palermo Observatory: http://dbms.astropa.unipa.it/

Table 2.2: Best-fit parameters for the bidimensional multi-component halo model.

Component	Center Position R.A.	Dec	r_0 (arcsec)	β	ϵ	θ (rad)	χ^2_ν	ν (d.o.f.)
Central	$03^h38^m28.9^s$	–35°27'01"	$3.93^{(a)}$	0.54±0.02	$0.0^{(a)}$	$0.0^{(a)}$	$1.2^{(b)}$	$1612^{(b)}$
Galactic	$03^h38^m25.0^s$	–35°27'40"	2125± 800	41± 25	0.018± 0.018	$1.09^{+1.97}_{-1.09}$		
Cluster	$03^h38^m48.2^s$	–35°23'05"	9000± 500	24± 3	0.14± 0.02	0.0 ± 0.1	1.5	4790

(a) The Central component parameters r_0, ϵ and θ have no error because they were held fixed during the fit.

(b) The χ^2 and ν values are the same for the 'Central' and 'Galactic' components because they were fitted together on the HRI image.

Note - uncertainties are 1σ confidence level for 5 interesting parameters

model composed of three bidimensional β components represented by expression (2.1) plus a constant background. **(d)** The first two components, representing the central and galactic halo emission, were fitted to the 15"×15" HRI data. Because at this resolution it is not possible to properly determine all the parameters of the central component, we fixed the core radius to the best-fit value obtained from the radial fit shown in Figure 2.5. While the central component shows a slight N-S elongation ($\epsilon \sim 0.05$, §2.2.3) at this resolution our attempts to vary also ellipticity ϵ and position angle θ resulted in no improvements of the fit, so that they were fixed to zero. **(e)** The third component, corresponding to the cluster emission, was fitted to the 45"×45" PSPC data, fixing the central and galactic halo parameters to the values obtained in step (d). The background value was fixed to the flattening level measured in §2.2.4. **(f)** Steps (d) and (e) were repeated iteratively until the best fit parameters converged within the errors.

The best-fit model parameters are shown in Table 2.2. In Figure 2.10 we show the model contours superimposed on the 45"/pixel PSPC image (main panel); the nuclear region is shown in greater detail in the right-bottom panel, with contours overlaid on the 15"/pixel HRI image. The three components have different features: while the central one is centered on the galaxy and is highly peaked, the more extended galactic halo is displaced to the South-West thus accounting of the observed asymmetries shown in Figure 2.9. In contrast with the circular symmetry of the smaller components ($\epsilon_{Central} \sim 0.05, \epsilon_{Galactic} = 0.02$) the third component is elongated in the East-West direction and its center is displaced to the North-East of the optical galaxy. These results suggest a different origin of each component,

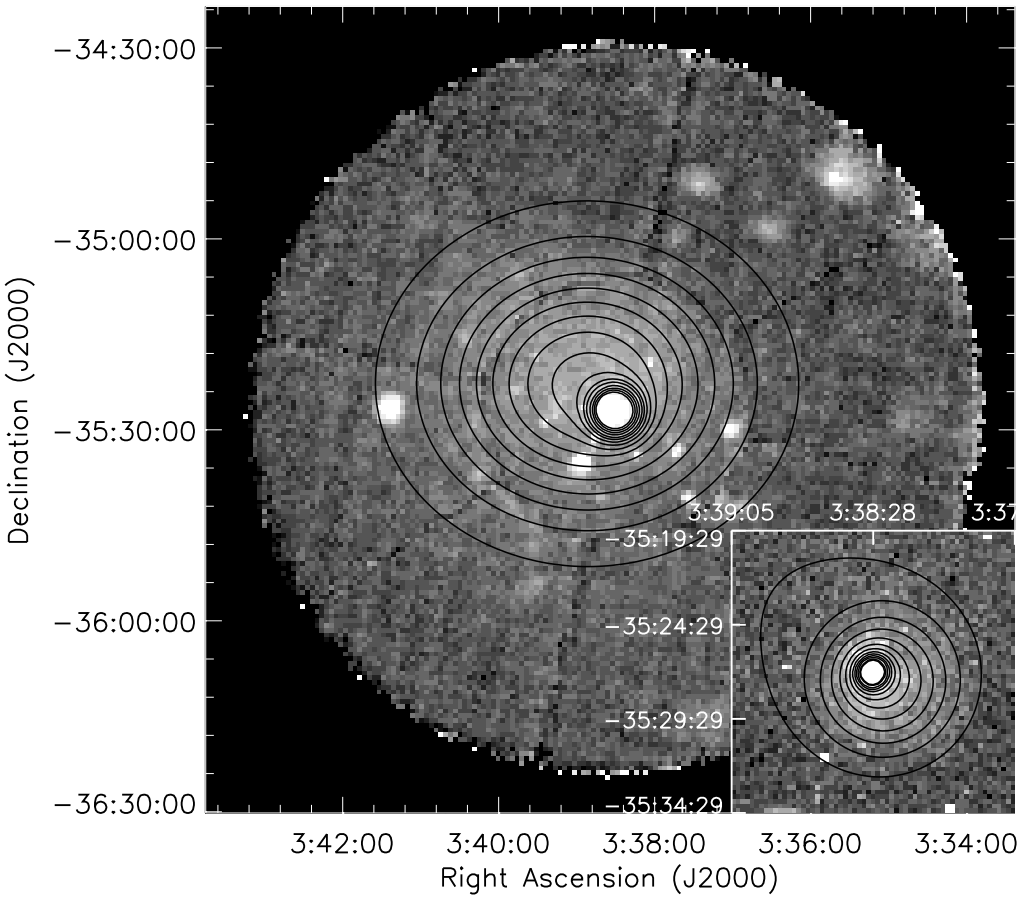

Fig. 2.10.— **Main panel:** contours of the bidimensional halo model superimposed on the 40"/pixel PSPC image. The cluster component is clearly displaced with respect to the galactic halo; the central component is not visible at this resolution. Contours are spaced by a factor of 1.1 with the lowest one at 3.1×10^{-3} cnts arcmin^{-2} s^{-1}. **Bottom-right panel:** bidimensional model contours overlaid on the 15"/pixel HRI image, showing in greater detail the galactic halo region. Contours are spaced by a factor of 1.1 with the lowest one at 6.0×10^{-3} cnts arcmin^{-2} s^{-1}.

that will be discussed in detail in § 2.3.

The χ^2 values obtained from the fit are quite large. This is not surprising considering the large spatial anisotropy of the X-ray surface brightness (see § 2.2.3). The situation is worse for the PSPC data (see Figure 2.6), also because of the poor knowledge of the exposure corrections past $\sim 1100''$ from the center of the FOV (the position of the support ring) and the large and irregular PRF at these radii that makes difficult a correct source masking. In

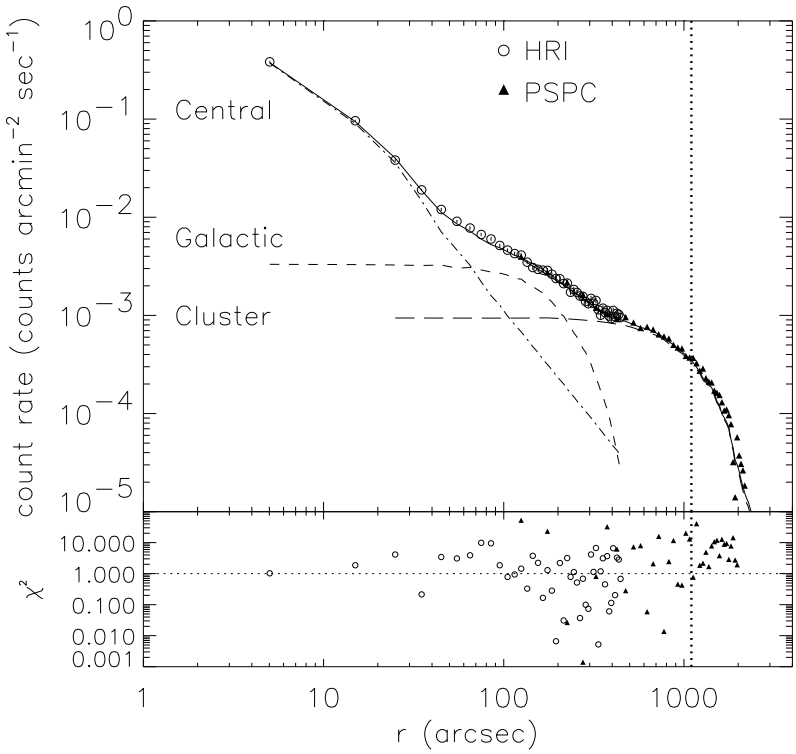

Fig. 2.11.— Radial profiles compared to the bidimensional model profiles. Open circles represent HRI counts while triangles represent PSPC counts rescaled to match the HRI. The continuous line represents the best-fit model while dot-dashed, short-dashed and long-dashed lines represent respectively the central, galactic and cluster halo components. The residuals are shown in the lower panel in χ^2 units. The vertical dotted line marks the position of the PSPC support ring; at larger radii the exposure correction is poorly known.

Table 2.2 the 'Central' and 'Galactic' components have the same χ^2 value because they were fitted together to the HRI data. If we restrict the fit to the region within 1 arcmin and use higher resolution (2"/pixel) we obtain a $\chi^2_\nu \sim 0.6$, in agreement with the results obtained in § 2.2.4 from the profile fitting.

The relative contribution of each component to the global profile is shown in Figure 2.11. We must notice that here both global and individual components profiles were extracted in annuli centered on the X-ray centroid (rather than centering each one on the respective component centroid) so to allow a comparison of the observed data with the model. The bottom panel shows the radial residuals respect to the best fit model. The high χ^2 values are in agreement with the values obtained from the bidimensional fit; in particular the residuals are systematically higher at radii larger than 1100" due to the problems explained above.

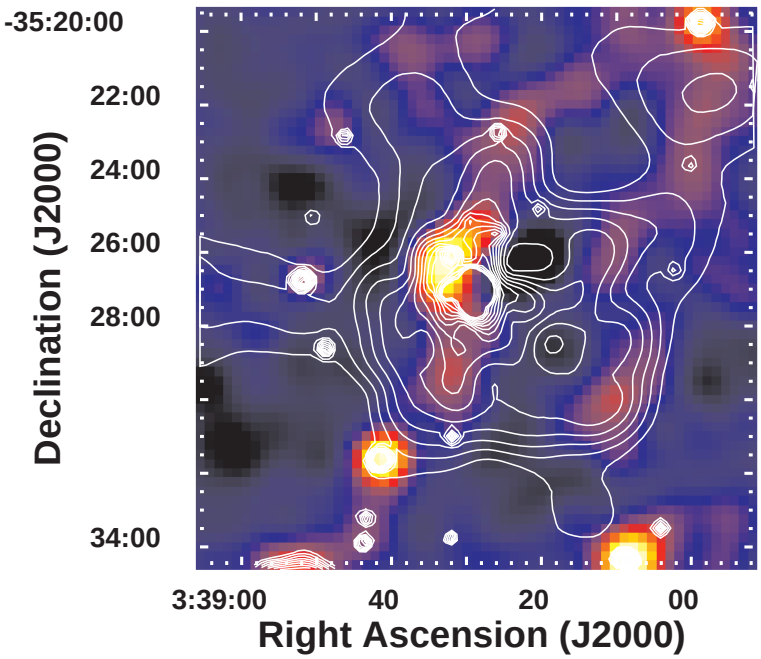

Fig. 2.12.— Residuals of the bidimensional fit on the 15 arcsec/pixel HRI image, after convolving with a gaussian of $\sigma = 30''$. Colors from black to white represent residuals from -2.5σ to 22σ. For comparison we superimposed the contour levels of the adaptively smoothed image (Figure 2.3a).

The residuals of the bidimensional fit to the HRI image are shown in Figure 2.12. The presence of structures in the gaseous halo is evident and confirms the results obtained with the adaptive smoothing technique. The highest residuals are coincident with the positions of point sources detected in the field, as can be seen from the overlaid contours. Considering the fluctuations on scales of 60" ($\sim$ 5 kpc) the statistical errors are reduced of a factor 4 with respect to the colorscale levels shown in Figure 2.12, and the significance of the residual emission is increased of the same factor. This means, for instance, that the deep 'hole' on the North-West side of the halo is approximately significant at the 6σ level above the fluctuations expected from the multicomponent model, while the excess emission regions on the North and South sides of the galactic center are significant at the 3σ level. Even though the multi-component bidimensional model may not be a proper physical representation of the hot X-ray halo this result shows that the filamentary structures seen in the halo are not due to statistical fluctuation over a smooth surface brightness distribution. This result is further confirmed by the *Chandra* data presented in § 2.2.10.

2.2.6. Density, Cooling Time and Mass Profiles

To derive the hot gas density of NGC 1399 we used the procedure discussed in § 1.4.2. Since the global gas distribution has a complex and asymmetric structure, we cannot apply this method to the total emission; instead we applied it to the single components separately. For the 'central' and 'galactic' components we assumed spherical symmetry; this is a reasonable approximation because their ellipticities, derived from the bidimensional models, are small (see previous section). The same approximation is not valid, instead, for the cluster halo so that, in deriving the density profile, we assumed rotational symmetry around the minor axis. We found that assuming symmetry around the major axis the difference is of the order of a few percents (except at very large radii where exposure correction uncertainties are dominant) and resulted in minor changes to our conclusions. The central, galactic and cluster components were assumed to be isothermal with temperatures of respectively kT =0.86, 1.1 and 1.1 keV, in agreement with the PSPC temperature profiles derived by RFFJ. Buote (1999) showed that ASCA data suggest the presence of multiphase gas within the central 5' of NGC 1399, better fitted by cooling flows models. However, as he notes, the narrower ROSAT energy range and the lower spectral resolution is unable to clearly discriminate between single and multi-temperature models (even though it reveals the presence of radial temperature gradients) so that our assumption of isothermal components is adequate for the kind of analysis performed here.

The electron density profiles of the isothermal components are shown in Figure 2.13. The density profiles are centered on the centers of their respective components and thus the total density does not take into account the centers offset. Including the displacements of each component with respect to the galaxy center results in a slightly smoother profile in the outer regions, due to the azimuthal averaging (see Figure 2.13). ROSAT and ASCA spectral fits (RFFJ; Buote 1999; Matsushita, Ohashi & Makishima 2000) revealed that additional absorption, over the galactic value, may be required in the galaxy center. We thus estimated an upper limit for the density of the central component assuming an absorption of 2×10^{21} cm^{-2} (downward triangles in Figure 2.13).

We must notice that adding the single density components, derived from the surface brightness decomposition, to obtain the total density profile is not strictly the correct approach since the surface brightness does not depend linearly on the gas density (see equations 1.7 and 1.31). However regions of the image in which more than one component are significant are small and the good agreement of our results with the estimate of RFFJ (who deprojected the total surface brightness) indicates that we are not introducing significant errors in our total density estimate. The same considerations hold for the mass profiles derived below.

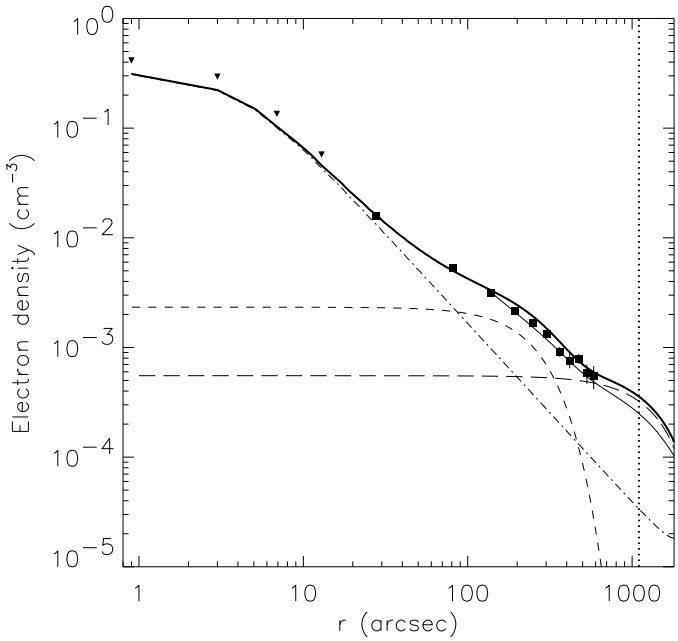

Fig. 2.13.— Density profiles derived from deprojection. Dot-dashed, short dashed and long dashed lines represent respectively the central, galactic and cluster halo component. Downward triangles show the upper limit on the central component profile adopting a central absorbing column of 2×10^{21} cm^{-2}. The thick (thin) continuous lines show the total density ignoring (including) the center offset of the different components (see discussion in text). For comparison the values obtained from Rangarajan et al. (1995) are shown as filled squares. As in Figure 2.11 the vertical dotted line marks the position of the PSPC support ring.

Using the density profiles and the assumed temperatures we estimated the cooling time (equation 1.37) as a function of radius. We adopted the cooling function given by Sarazin & White (1987). Figure 2.14 shows that the central and galactic components have cooling times much shorter than the age of the universe, assumed to be $\sim 10^{10}$ years, out to 250" and 350" (23 and 32 kpc) respectively.

The cumulative gas mass profile is shown in Figure 2.15a as a function of radius. The flat profile of the galactic component over 600" (55 kpc) reflects the steep slope of the Beta profile. The filled triangles show that the adoption of a high absorbing column in the galaxy center does not affect significantly the gas mass estimates, giving a difference of $\sim$33%. The total gravitating mass was calculated using expression (1.35). We tried four different temperature profiles based on published data: we used both the linear and power-law approximations derived by Jones et al. (1997) based on PSPC spectral fits, a constant temperature of 1.1 keV that approximates the isothermal profile found by RFFJ and a power-

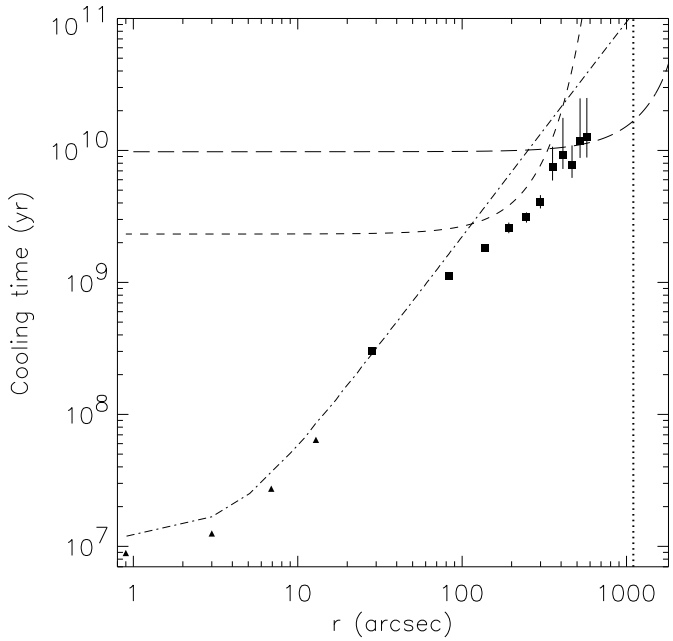

Fig. 2.14.— Cooling time profiles derived from deprojection. The symbols have the same meaning as in Figure 2.13. Note that the assumption of a high central absorption translates into lower limits on the central cooling time (filled triangles).

law profile $T(r) = T_0 r^{\alpha}$, with $T_0 = 0.6$ keV and $\alpha = 0.13$, representing the temperature drop in the inner 150" (14 kpc). The gravitating mass, extracted in concentric annuli centered on the X-ray centroid (i.e. taking into account the offset between the different components), is shown in Figure 2.15b. The similarity of the continuous lines indicates that the gravitating mass is weekly dependent on the assumed temperature profile and is mostly determined by the density profile. The largest deviation is seen in the model taking into account the central temperature drop, which is systematically lower in the inner 100". Our profiles are in good agreement with RFFJ and fall within the range predicted by optical observations (shaded region, Saglia et al. 2000). We clearly distinguish the transition between the galaxy and cluster halo near 700" (64 kpc), in agreement with the ASCA data (filled circles, Ikebe et al. 1996). Both components exceed the luminous mass, based on an extrapolation of stellar measurements (thin dashed line), indicating the presence of a consistent amount of dark matter.

Thanks to the ROSAT HRI resolution in the inner 100" (9 kpc) we are able to resolve the dynamical behavior of the central component. The gravitating mass follows closely the stellar mass profile, confirming that the central galaxy dynamics are dominated by the

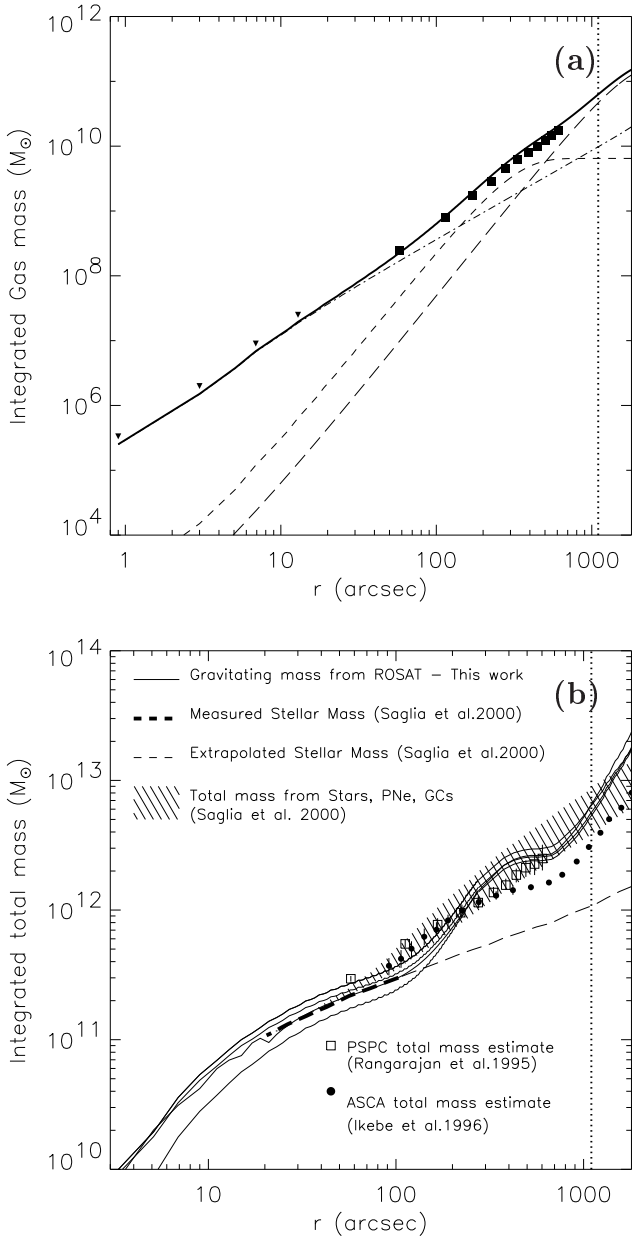

Fig. 2.15.— Integrated mass profiles derived from deprojection. **(a)** Integrated gas mass, with symbols having the same meaning as in Figure 2.13. **(b)** Integrated gravitating mass for our different temperature profiles (see discussion in text) are shown as continuous lines. Open squares and filled circles represent the total gravitating mass estimated respectively by Rangarajan et al. (1995) and Ikebe et al. (1996). The gravitating mass range derived by Saglia et al. (2000) from optical observations of stars, GCs and PNe, is shown as a shaded region. The contribution of the stellar matter measured (extrapolated) by Saglia et al. (2000) is represented by the thick (thin) dashed line.

luminous matter (Saglia et al. 2000).

2.2.7. Total Fluxes and Luminosities

To determine the total HRI X-ray flux of NGC 1399 we measured the total net counts within a 500" radius from the X-ray centroid. The background counts were extracted from the rescaled particle map (see § 2.2.4) in the 500"–850" annulus . We then corrected the background subtracted counts for the contamination of pointlike sources within the 500" circle. This was done by subtracting, for each source, the net counts measured by the wavelets algorithm (see § 2.2.9). The final count rate, for the hot halo of NGC 1399, is 0.451±0.004 counts sec^{-1}.

To convert this count rate into a flux we used the best fit Raymond-Smith (RS) model found by RFFJ from the ROSAT PSPC data (a main thermal component with $kT \simeq 1$ keV plus a softer emission with $kT = 80.8$ eV contributing for 16% of the emission in the 0.2–0.3 keV range). Using the HEASARC-XSPEC software, we simulated a RS spectrum fixing the absorbing column to the galactic value (1.3×10^{20} cm^{-2}) and the metal abundance to the solar value. With this spectrum, we calculated the conversion factor between counts and fluxes using the PIMMS software, that takes into account the HRI spectral response function. We obtain 1 count sec^{-1}=3.158×10^{-11} erg s^{-1} cm^{-2} so that $f_X = (1.42 \pm 0.01) \times 10^{-11}$ erg s^{-1} cm^{-2} in the 0.1-2.4 keV energy range. Assuming a distance of 19 Mpc, $L_X(0.1 - 2.4keV) = (5.50 \pm 0.04) \times 10^{41}$ erg s^{-1}. Taking into account the uncertainties in the exposure correction and background extraction, this result agrees within 10% with the estimate of RFFJ, converted to our adopted distance.

We also searched for evidence of nuclear variability in our data, finding none.

2.2.8. X-ray/Radio Comparison

NGC 1399 is known to be a radio galaxy with a faint radio core ($S_{core} \sim 10$ mJy at 5 GHz, Ekers et al. 1989). Killeen, Bicknell & Ekers (1988) studied in detail the 6 and 20 cm radio emission. The 6 cm radio contours (their Figure 1) are superimposed on the 'csmoothed' X-ray image in Figure 2.16. The radio core lies in the center of the galaxy, but the nuclear source is not distinguishable from the radio jets at this resolution.

We searched our X-ray data for a central point source that could be the counterpart of the radio core. Trying to model the nuclear emission with a Beta model plus a delta function, convolved with the HRI PRF, resulted in minor variations in the Beta model

parameters and no improvement in the fit statistics, thus indicating no need for additional nuclear emission. To estimate an upper limit we varied the central point source brightness and repeated the fit until we reached a 3σ confidence level. We obtain an upper count rate limit of 2.25×10^{-3} counts s^{-1}. Assuming a power law spectrum with photon index $\alpha_{ph} = 1.7$ and galactic absorption N_H, we get $f_X^{3\sigma} = 1.0 \times 10^{-13}$ erg s^{-1} cm^{-2} in the 0.1-2.4 keV band, corresponding to $L_X^{3\sigma} = 3.9 \times 10^{39}$ erg s^{-1}. This value is approximately half of the one derived by Sulkanen & Bregman (2001) making use of one of our HRI observations (RH600831a01) and 30% of the limit estimated by RFFJ by means of spectral analysis. Recently Loewenstein et al. (2001) were able to further reduce the upper limit on the nuclear source by one order of magnitude making use of *Chandra* data.

By comparing the 6 cm radio contours with the X-ray halo (Figure 2.16) we identify several interesting features: i) in the X-rays the nuclear region is elongated in the N-S direction, following the radio jets. This elongation is more pronounced in the Southern direction, where there is an excess of X-ray emission following the Western side of the jet (region A); ii) At the point where the Southern jet ends in the lobe there is a steep gradient in the X-ray emission. The lobe is bent towards the West and aligned with a region of low X-ray emission (region B); iii) The Southern lobe ends in an irregular clump coincident with a region of higher X-ray emission (region C); iv) No features as the ones seen in the Southern lobe are evident in the Northern one. Here the radio jet ends smoothly in a regular lobe with no sign of sharp transition and there is no evidence of cavities (minima) in the X-ray emission. Instead the jet and the lobe are aligned with an X-ray structure that seems to be coincident with the right side of the jet/lobe. At the North-West end of the Northern lobe there are two X-ray clumps (region D): they are detected as a single source by the wavelet algorithm (No.32 in Table 2.3). To a more accurate visual inspection we found that the smaller and compact source is coincident with an optical (probably background) counterpart, while there is no counterpart for the diffuse clump (§ 2.2.9) suggesting that it is a local feature of the hot gaseous halo.

From the residual image of the two-dimensional fit (Figure 2.12) we can calculate the significance of these features. We find that the depletion corresponding to the Southern lobe (region B) and the Northern diffuse clump (region D) are significant respectively at the 2.5σ and $\sim 4\sigma$ level. Region C corresponds to a 3σ brightness enhancement (§ 2.2.5).

To examine in greater detail the nuclear region we subtracted the halo model developed in § 2.2.5 from the X-ray image to produce a residual map of the nuclear region with a 2"/pixel resolution (Figure 2.17). As discussed at the beginning of this section, there is no evidence of a nuclear point source aligned with the radio centroid. Instead residual emission is visible on both sides of the radio jets a few arcseconds (≤ 1 kpc) from the nucleus. There

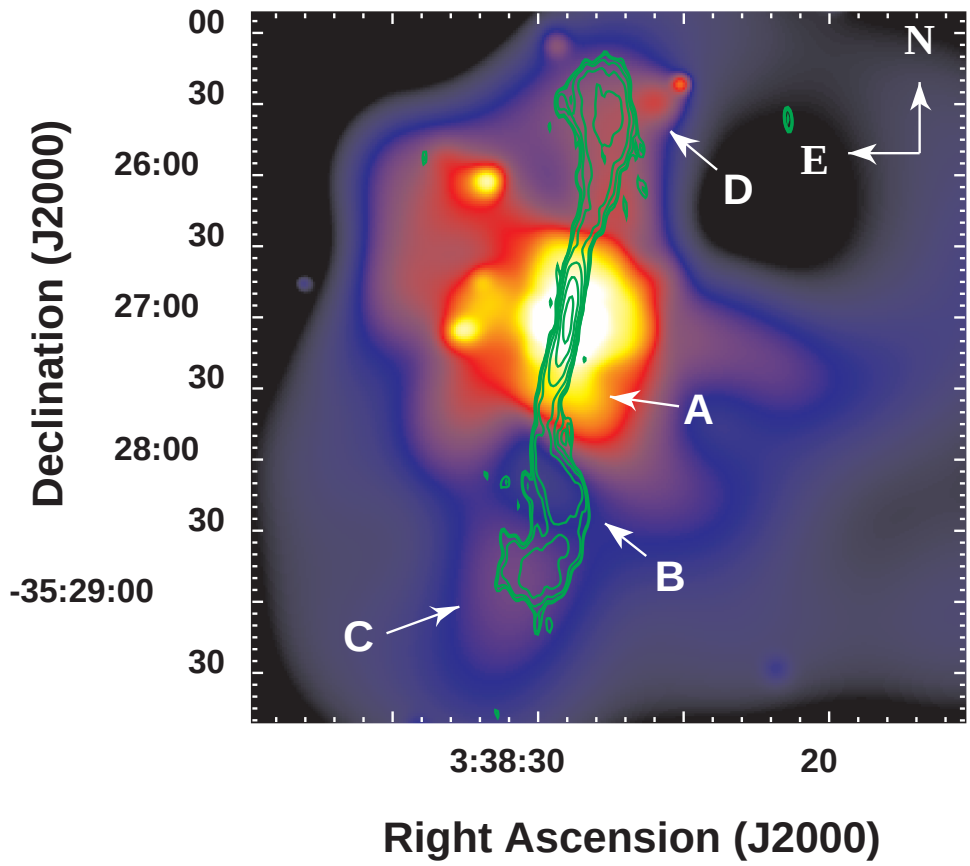

Fig. 2.16.— 6 cm radio contours (green; from Figure 1 of Killeen, Bicknell & Ekers 1988) superimposed on the adaptively smoothed 1"/pixel X-ray image. The logarithmic color scale represents intensities from 8.6×10^{-3} (black) to 6.7×10^{-1} (white) cnts arcmin^{-2} s^{-1}.

is no evidence that any of these excesses may be due to the nuclear source because they are displaced with respect to the radio emission. Moreover the radio emission seems to avoid the X-ray excess on the eastern side of the nucleus, suggesting that these features may be correlated.

In coincidence with the direction of the radio jets there are two regions of negative residuals ($\sim -2\sigma$), extending up to $\sim$ 20", where additional excess emission, on both the Northern and Southern sides of the X-ray core and aligned with the radio jets, is clearly visible. The Southern excess corresponds to region A of Figure 2.16. Residual emission is

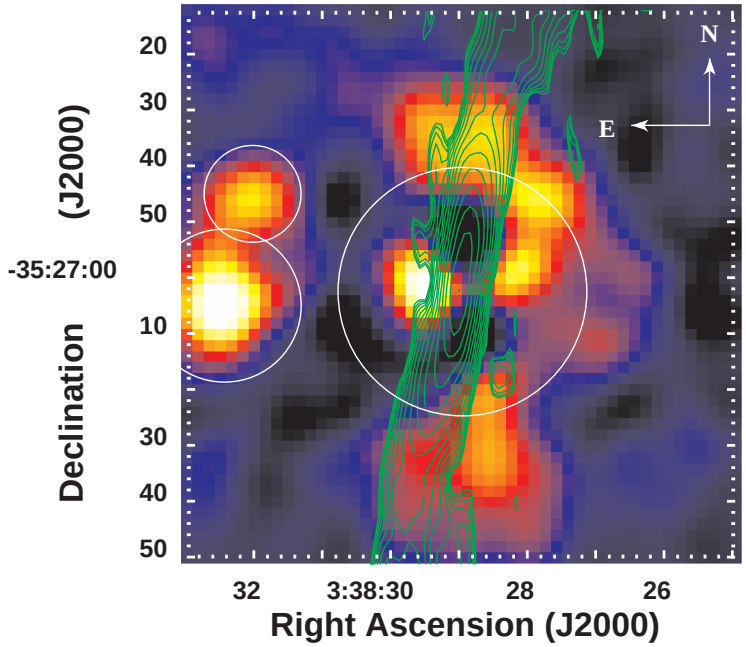

Fig. 2.17.— 6 cm radio contours superimposed on the 2"/pixel residuals X-ray image of the nuclear region. The image has been smoothed with a gaussian of $\sigma = 4$". In the logarithmic color scale black represents negative residuals while colors from blue to white represent increasing positive residuals. The residuals range from -2.2σ to $+4\sigma$. The white circles on the left show the positions of X-ray sources detected by the wavelets algorithm (No.2 and 11 in Table 2.3). The radius of the central source (corresponding to the central X-ray peak) is ~ 22".

also present on the Western side of the nuclear region. Visual inspection of the *Chandra* image (Figure 2.21) shows that this excess is probably due to the presence of point sources unresolved in the HRI image.

From the density profiles obtained in § 2.2.6 we were able to obtain the pressure profiles of the three halo components shown in Figure 2.18. The pressure profiles are compared to the minimum radio pressure measured by Killeen, Bicknell & Ekers (1988) in the Northern (circles) and Southern (triangles) radio jets/lobes. The Figure confirms their result that the radio source can be confined by the ISM whose pressure is higher than the radio one. We must notice that they found a difference between radio and thermal pressure of more than one order of magnitude, while we find $P_{Thermal}/P_{Radio} = 3 \div 4$. This is mostly due to the poor ISM temperature constraint obtained from the *Einstein* IPC data and to our better spatial resolution.

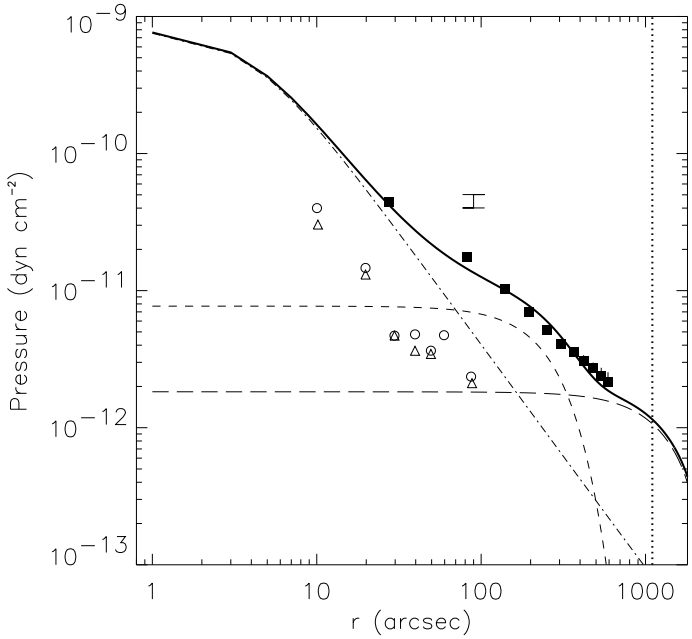

Fig. 2.18.— Gas pressure profiles derived from deprojection. The symbols have the same meaning of Figure 2.13. Open circles and triangles represent respectively the radio pressure of the Northern and Southern lobes measured by Killeen, Bicknell & Ekers (1988). The vertical error bar in the Figure indicates the pressure range of the D region (see discussion in text).

The vertical error bar in the Figure indicates the pressure estimate for the diffuse clump observed in the D region. To calculate this value we assumed that the brightness enhancement is due to a homogeneous sphere of $\sim$ 9" (800 pc) radius at the same temperature of the galactic halo (1.1 keV). Depending on whether the background is extracted locally (an annulus 9" wide) or from the Beta model, the 'bubble' pressure can vary up to 25%, so that the allowed range is shown as an error bar. This estimate is dependent on the assumed geometry of the emitting region and on projection effects, so that it must be considered as an upper limit on the actual pressure.

2.2.9. Discrete Sources

We used the algorithm developed at the Palermo Observatory by F. Damiani and collaborators (Damiani et al. 1997a) to detect the discrete sources present in the HRI field. The algorithm measures the relevant parameters in a wavelet transformed space, using differ-

ent wavelet scales to optimize the detection of both compact and extended sources. The wavelet algorithm found 43 sources in our field, using a signal to noise threshold of 4.65. The threshold was chosen to assure a contamination of one/two spurious detections per field (F. Damiani private communication, see also Damiani et al. 1997b). Three more sources were found with the algorithm, but being clearly associated to the ribbon-like features due to the presence of bad pixels in the detector (Figure 2.2), were excluded from the subsequent analysis. After visual inspection of the adaptively smoothed image (Figure 2.3) three more detections (No.44, 45, 46) with a lower S/N ratio but showing clear features of pointlike sources, were added to the list.

The source positions in the field are shown in Figure 2.19. Sources No.42 and 43 are clearly extended and seem to be associated to structures in the NGC 1399 halo revealed by the adaptive smoothing algorithm (§ 2.2.3).

Table 2.3 lists the parameters measured with the wavelets algorithm for each source: position, 3σ radius, number of counts with statistical error, maximum signal to noise ratio (for sources detected at different spatial scales), count rate and flux in the 0.5-2.0 keV band for both HRI and PSPC data. We computed the flux of each source assuming a power law spectrum with photon index $\alpha_{ph} = 1.96 \pm 0.11$ ($f^{pow.law}$ in Table 2.3), as found by Hasinger and collaborators for faint sources. This gives a conversion factor of 1 cnt s^{-1}=2.087×10^{-11} ergs s^{-1} cm^{-2} in the 0.5-2.0 keV band (the same used by Hasinger). We also tried a Raymond-Smith spectrum with $kT = 0.52$ KeV and abundance $Z \sim 0.2\ Z_{\odot}$, following the results of Kim & Fabbiano (1995) in their study of pointlike sources near NGC 507, and obtaining an almost identical result. In Table 2.3 $f^{max\ abs.}$ represent the flux estimated with the power law model fixing the absorption to the upper limit of 4.5×10^{20} cm^{-2}, allowed from the spectral analysis performed by RFFJ.

The the last three columns of Table 2.3 report the source short-term variability obtained with a Kolmogorov-Smirnov test of the HRI light curves, long-term variability from comparison with PSPC fluxes (as explained below), and possible optical counterparts (within the 3σ radius measured by the wavelets algorithm) found by both visual inspection of the DSS photographic plates and cross-checking with known sources present in the NASA Extragalactic Database (NED). The names of the counterparts correspond to those reported by Hilker et al. (1999b) or Smith et al. (1996) in their optical and NUV studies of the Fornax field. Sources No.27 and 28, representing respectively NGC 1399 and NGC 1404, are not included in the table.

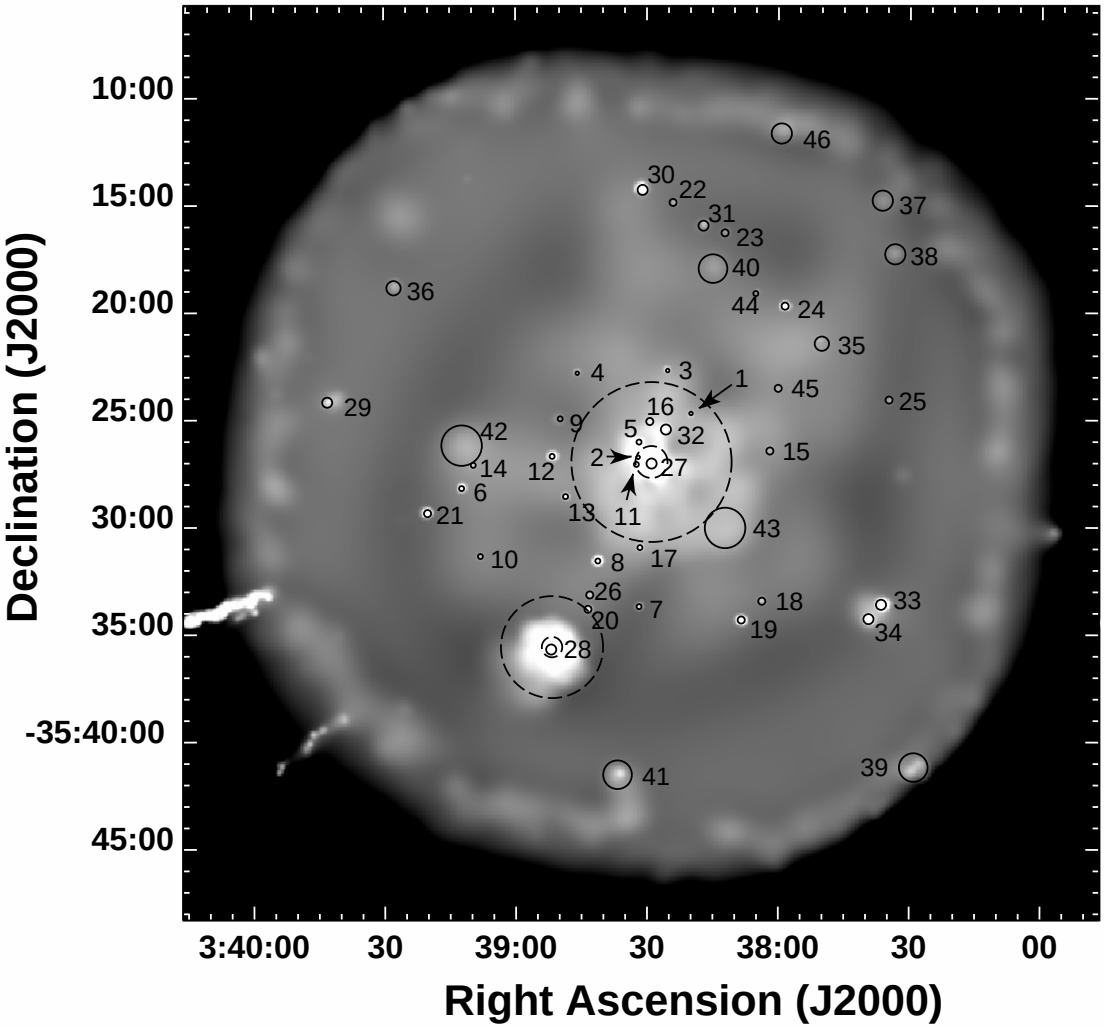

Fig. 2.19.— The sources detected with the wavelets algorithm of Damiani et al. (1997a,b) superimposed on the 5"/pixel adaptively smoothed HRI image. Solid circles show the region of maximum S/N ratio for each source. Dashed circles represent r_{eff} and $5r_{eff}$ for NGC 1399 and NGC 1404 (Goudfrooij et al. 1994).

Table 2.3: Discrete Sources Properties

Source No.	R.A. (J2000)	Dec. (J2000)	3σ Radius (arcsec)	Counts	Max S/N	Count Rate (10^{-4} Cnts sec^{-1})	$f_{HRI}^{pow.law\,(a)}$	$f_{HRI}^{max\ abs.\,(a)}$	$f_{PSPC}^{pow.law\,(a)}$	Time Var.$^{(b)}$ short-term / long-term	Opt.id.	NED obj.$^{(c)}$
1	3:38:20.0	-35:24:42	8.7	35±12	4.7	2.1±0.7	4.3±0.2	5.6	28±7	n/y	-	-
2	3:38:32.0	-35:26:45	8.7	54±17	6.1	3.2±1.0	6.7±0.3	8.6	-	n/···	-	-
3	3:38:25.3	-35:22:42	8.7	49±14	6.7	2.9±0.8	6.1±0.3	7.8	-	n/···	-	-
4	3:38:45.9	-35:22:50	8.7	42±12	6.1	2.6±0.7	5.3±0.3	6.9	9±3	n/n	y	CGF 0202
5	3:38:31.8	-35:26:02	11.9	165±23	13.0	10±2	20±1	26.0	-	n/···	-	CGF 0233
6	3:39:12.3	-35:28:12	13.2	172±21	14.9	10±1	21±1	27.5	25±4	n/n	y	-
7	3:38:31.8	-35:33:42	12.2	56±16	6.0	3.3±0.9	6.9±0.3	8.9	8±3	n/n	-	-
8	3:38:41.2	-35:31:35	10.8	1000±35	60.6	59±2	123±6	159.2	170±8	99%/y	y	-
9	3:38:49.8	-35:24:57	12.2	47±14	5.0	2.8±0.9	5.8±0.3	7.5	-	n/···	-	-
10	3:39:08.1	-35:31:22	12.2	56±16	6.2	3.3±0.9	6.9±0.4	8.9	22±6	n/n	-	-
11	3:38:32.4	-35:27:05	13.7	171±30	11.5	10±2	21±1	27.2	-	n/···	-	-
12	3:38:51.7	-35:26:42	11.6	295±22	24.7	17±1	36±2	47.0	58±6	95%/y	y	CGF 0102
13	3:38:48.6	-35:28:35	12.2	77±20	7.7	4.5±1.1	9.3±0.5	12.0	-	n/···	y	-
14	3:39:09.7	-35:27:07	12.2	46±14	5.0	2.8±0.8	5.7±0.3	7.4	-	n/···	y	-
15	3:38:01.9	-35:26:27	17.3	62±19	4.7	3.6±1.1	7.5±0.4	9.7	-	n/···	-	-
16	3:38:29.4	-35:25:05	17.3	75±23	4.8	4.4±1.3	9.1±0.5	11.7	-	n/···	-	-
17	3:38:31.6	-35:30:58	12.2	70±18	6.8	4.1±1.1	8.6±0.5	11.1	-	n/···	-	-
18	3:38:03.7	-35:33:27	17.3	65±19	5.4	4.1±1.2	8.5±0.4	10.9	-	n/···	y	CGF 0354
19	3:38:08.5	-35:34:20	15.0	908±34	52.3	57±2	119±6	152.7	127±7	99%/n	y	-
20	3:38:43.5	-35:33:50	15.2	105±18	8.7	6.3±1.1	13.1±0.7	16.8	-	n/···	y	-
21	3:39:20.1	-35:29:22	16.5	527±30	33.0	32±2	68±4	86.9	83±7	99%/n	y	-
22	3:38:24.1	-35:14:52	17.3	60±18	4.9	3.8±1.2	8.0±0.4	10.3	12±4	n/n	y	-
23	3:38:12.2	-35:16:17	17.3	59±18	4.8	3.7±1.1	7.7±0.4	9.9	-	n/···	y	-

$^{(a)}$ Flux in the 0.5-2.0 KeV band in units of 10^{-15} erg s^{-1} cm^{-2}.

$^{(b)}$ Short-term = probability of the Kolmogorov-Smirnov test: 'n' means no variability detected at the 95% level.
Long-term = difference between PSPC and HRI counts: 'y' means variable source ($> 3\sigma$), 'n' means no variability detected, '···' means no available data.

$^{(c)}$ CGF=Hilker et al. (1999b); FCCB=Smith et al. (1996)

Table 2.3: - Continued

Source No.	R.A. (J2000)	Dec.	3σ Radius (arcsec)	Counts	Max S/N	Count Rate (10^{-4} Cnts sec^{-1})	$f_{HRI}^{pow.law\,(a)}$	$f_{HRI}^{max\ abs.\,(a)}$	$f_{PSPC}^{pow.law\,(a)}$	Time Var.$^{(b)}$ short-term / long-term	Opt.id.	NED obj.$^{(c)}$
24	3:37:58.5	-35:19:42	16.7	379±27	24.9	24±2	48±2	61.6	75±7	n/y	y	-
25	3:37:34.8	-35:24:04	17.3	64±19	5.3	4.0±1.2	8.3±0.4	10.6	-	n/···	-	-
26	3:38:43.1	-35:33:10	17.3	73±21	5.6	4.3±1.2	9.0±0.5	11.6	-	n/···	y	-
29	3:39:43.0	-35:24:11	24.3	143±27	8.6	10±2	21±1	26.7	62±8	n/y	y	-
30	3:38:31.0	-35:14:17	26.4	586±38	26.5	38±2	79±4	102.1	-	99%/···	y	FCCB 1263
31	3:38:17.1	-35:15:57	24.5	124±31	7.2	8±2	16.4±0.8	21.1	-	n/···	y	-
32	3:38:25.7	-35:25:27	24.5	145±37	6.2	8.5±2.2	17.7±0.9	22.8	27±7	n/n	y	-
33	3:37:36.5	-35:33:37	24.2	921±40	41.4	60±3	125±6	161.5	-	n/···	y	-
34	3:37:39.4	-35:34:17	21.9	426±31	24.2	28±2	58±3	74.5	-	n/···	y	-
35	3:37:50.1	-35:21:27	34.6	139±37	5.8	8.4±2.3	17.6±0.9	22.6	-	n/···	y	-
36	3:39:27.8	-35:18:52	34.6	129±35	5.6	8.6±2.3	18.0±0.9	23.2	46±8	n/y	y	-
37	3:37:36.3	-35:14:47	49.0	153±44	5.1	11±3	24±1	30.7	25±7	n/n	-	-
38	3:37:33.4	-35:17:17	49.0	190±49	6.0	13±3	27±2	35.2	-	n/···	-	-
39	3:37:29.0	-35:41:11	69.3	580±119	14.1	67±14	140±7	180.1	232±12	n/···	y	-
40	3:38:14.7	-35:17:57	69.3	244±67	5.2	15±4	31±2	40.3	-	n/···	-	-
41	3:38:36.7	-35:41:32	62.9	366±61	8.9	24±4	51±3	65.8	57±7	n/n	-	-
42	3:39:12.3	-35:26:12	98.0	312±91	4.7	19±5	39±2	50.7	-	n/···	-	-
43	3:38:12.2	-35:30:02	98.0	365±101	5.0	22±6	46±2	59.1	60±14	n/n	-	-
44	3:38:05.1	-35:19:05	12.2	42±13	4.6	2.5±0.8	5.3±0.3	6.8	-	n/···	-	-
45	3:37:59.9	-35:23:30	17.3	56±18	4.4	3.3±1.0	6.8±0.4	8.8	-	n/···	-	-
46	03:37:59.2	-35:11:37	49.0	134±42	4.4	9.9±3.1	20±1	26.6	28±8	n/n	-	-

(a) Flux in the 0.5-2.0 KeV band in units of 10^{-15} erg s^{-1} cm^{-2}.

(b) Short-term = probability of the Kolmogorov-Smirnov test: 'n' means no variability detected at the 95% level.
Long-term = difference between PSPC and HRI counts: 'y' means variable source ($> 3\sigma$), 'n' means no variability detected, '···' means no available data.

(c) CGF=Hilker et al. (1999b); FCCB=Smith et al. (1996)

We tried to determine which X-ray sources belong to the Fornax cluster both by visual inspection of the photographic DSS plates and by comparing their positions with those of published catalogs of the Fornax region. Sources No.2 and 11 are likely to belong to NGC 1399 because of their position within the optical effective radius (r_{eff} = 44.7", Goudfrooij et al. 1994) while sources No.16 and 32 appear to be coincident with the position of two globular clusters (Kissler-Patig et al. 1999). Two sources are clearly associated with background objects: source No.4 corresponds to a background galaxy located at $z = 0.1126$ and represents the X-ray counterpart of the strongest component of the radio source PKS 0336-35 (Carter & Malin 1983); source No.30 is coincident with two optical background galaxies classified as interacting by Ferguson (1989) and clearly visible on the DSS plates. For the remaining sources there is no clear indication of whether they belong to the Fornax cluster or not.

Sources No.8, 12, 19, 21, 30 are variable at the 95% confidence level, according to our KS tests. Source No.30 is associated with a short X-ray burst occurred in the background galaxy between January and August 1996. In fact the source is not detected in both the August 1991 PSPC (RP600043n00) and the February 1993 HRI observations (RH600256n00). It is present, instead, in the last two HRI observations (RH600831n00 and RH600831a01) with a decrease in the observed count rate of a factor 8 between the two.

We must notice that our HRI background level was also variable so that the presence of short-term temporal variability was clearly detect only for the strongest sources ($f_{HRI}^{pow.law} \geq 3 \times 10^{-14}$ erg s^{-1} cm^{-2}). However, since the background subtraction was performed locally (i.e. extracting the background in a region surrounding the source, see Damiani et al. 1997a), this variability does not affect the source counts reported in Table 2.3. To further check the reliability of the wavelets algorithm, we extracted the counts manually for each source using a local annulus to measure the background, finding consistent results (within 1σ) with those derived by the wavelets technique.

We cross-checked our source list with the list of sources detected on the PSPC image by the GALPIPE project (see §2.2.5). Several sources detected in the HRI field were bright enough and sufficiently isolated to allow a comparison of the PSPC flux with the HRI results and to check for long-term variability. We converted the PSPC count rates to fluxes in the 0.5-2.0 keV band (1 cps=6.397×10^{-12} ergs cm^{-2} s^{-1}), assuming the same power law spectral model used for converting the HRI counts (see below). The PSPC fluxes and long-term variability (i.e. when PSPC and HRI flux estimates differ more than 3σ) are included in Table 2.3.

This comparison also confirmed that sources No.39 and 46, both near the very edge of the HRI FOV, are not an artifact of the poor S/N ratio or the steep emission gradient

because both are present in the PSPC data as well and detected with high significance.

We compared our source flux distribution to the expected background counts obtained from a deep survey of the Lockmann hole (Hasinger et al. 1993). We used the sensitivity map generated by the wavelet algorithm to weight each source for the effective detector area above the corresponding limiting flux. In this way we are able to normalize the measured counts at each flux to the total surveyed area. The flux distribution is shown in figure 2.20 where our differential counts are compared to the Hasinger ones. The horizontal error bars take into account uncertainties in the the power law slope. Our counts are higher than the Hasinger estimate, giving a total of 312 ± 47 sources vs 230 ± 15 expected counts, but still compatible within 2σ. To take into account absorption uncertainties we estimated a lower limit on the number of expected sources adopting the higher absorption value found by RFFJ in the NGC 1399 field (see above). In this case the number of expected counts decreases to 184 ± 14 leading to an upper limit of the observed excess of $\sim 2.6\sigma$.

The spatial distribution of detected sources is not uniform. In Figure 2.20 we show the source excess in circular annuli centered on NGC 1399. We find that the excess is peaked on the dominant galaxy, suggesting that the inner sources are likely to be associated with NGC 1399 rather than being background objects. In fact, excluding the central 300" (28 kpc), the measured counts drop to 244 ± 37, in agreement within less than 1σ from the expected value. The X-ray luminosity of the sources within the central 300" range from 1.7×10^{38} erg s^{-1} to 1.4×10^{39} erg s^{-1}, if they are in NGC 1399. Thus all of them have luminosities in excess of 1.3×10^{38} erg s^{-1}, i.e. the Eddinghton luminosity for a 1 $M_{\odot}$ neutron star (§ 1.3.3), suggesting that they may have massive Black Hole companions if they are accretion binaries.

2.2.10. The *Chandra* data

While this work was in progress the *Chandra* data on NGC 1399 became public. A full data reduction of the *Chandra* data, which is however already in progress (Angelini, Loewenstein & Mushotzky 2001; Loewenstein et al. 2001), is beyond the aim of the present work. However we decided to compare the ROSAT data with the *Chandra* image to see if our conclusions are supported by the improved *Chandra* resolution and sensitivity.

We used the longest *Chandra* observation of 60 ks (Obs. ID 319, 55.942 ks live time), performed on 2000 January 18 with the ACIS-S detector. We produced a 0.5 arcsec/pixel image in the energy band 0.3-10 keV, from the ACIS-S3 chip, which covers the central 8×8 arcmin of NGC 1399. The image was then adaptively smoothed with the *csmooth* algorithm included in the CIAO package. The final image is shown in Figure 2.21. No exposure

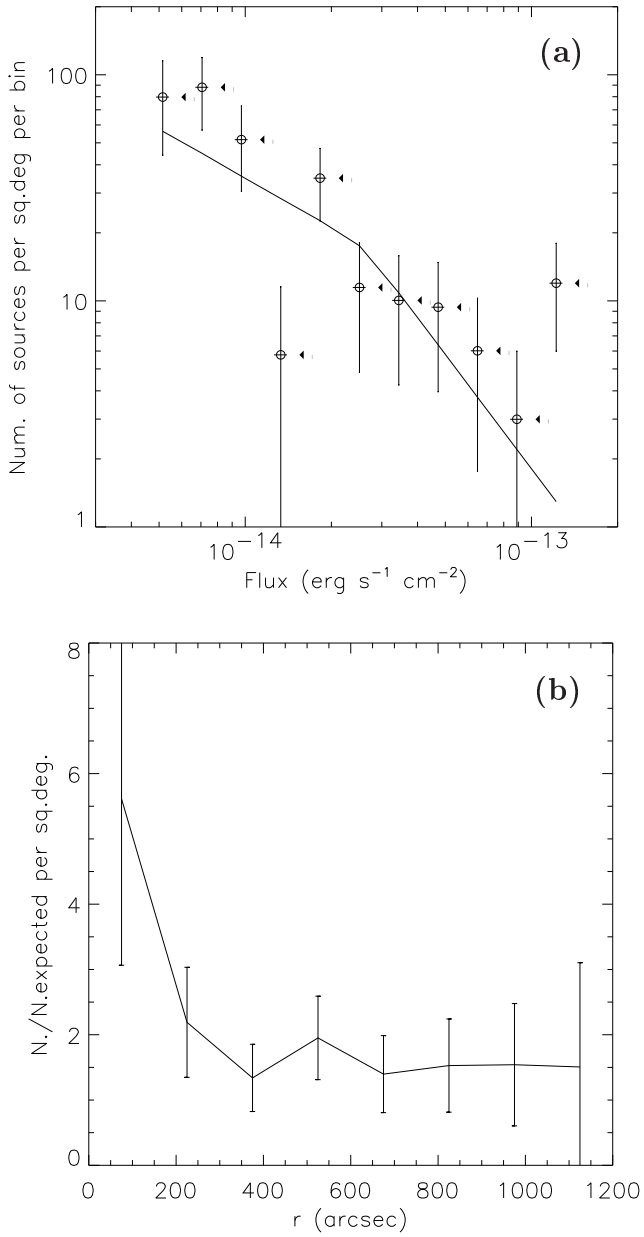

Fig. 2.20.— **(a)** Measured vs expected source counts. Measured counts, corrected for sensitivity variations across the detector, are represented by empty circles, while the continuous line is the expected distribution from Hasinger et al. (1993). Horizontal error bars take into account uncertainties in the power law slope. Arrows represent upper limits obtained fixing the absorption to 4.5×10^{20} cm^{-2} (Rangarajan et al. 1995). **(b)** Radial excess of sources over the expected number from Hasinger et al. (1993). The excess is concentrated around NGC 1399, thus suggesting to be due to sources associated with the galaxy.

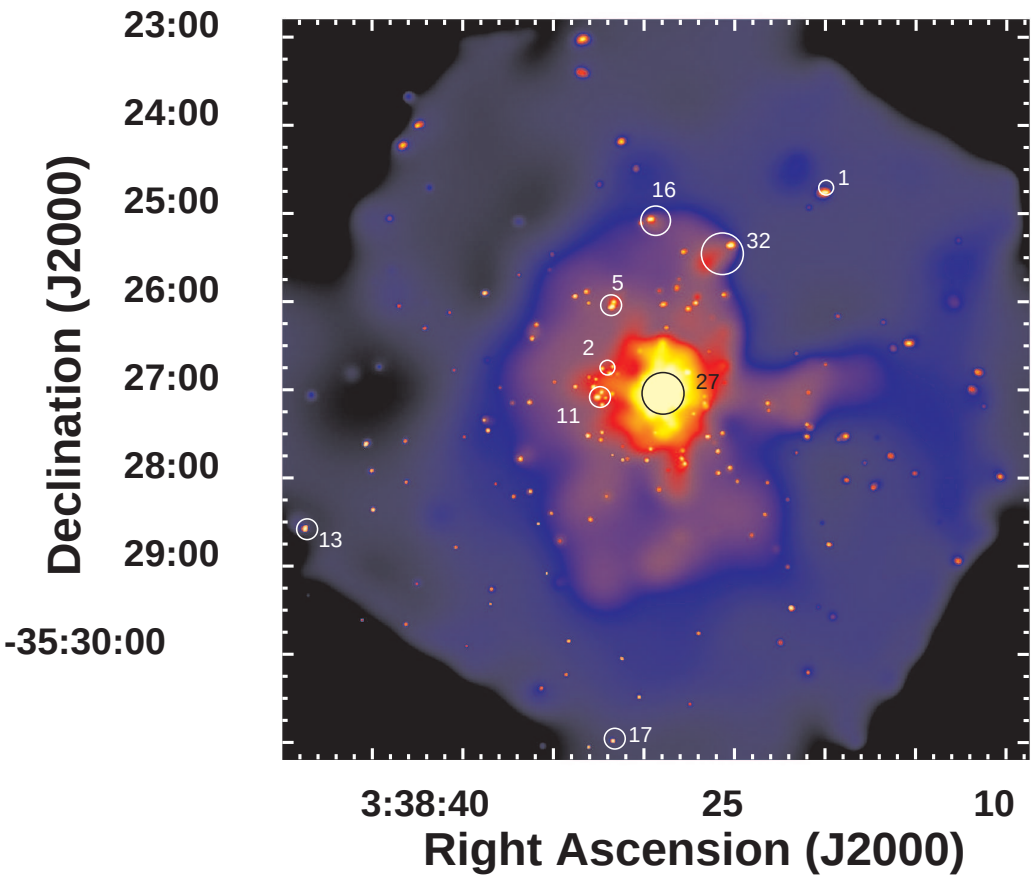

Fig. 2.21.— Adaptively smoothed *Chandra* ACIS-S image of NGC 1399 in the energy range 0.3-10 keV. Colors from black to white represent count rates from 0.021 cnts s^{-1} $arcmin^{-2}$ to 7.7 cnts s^{-1} $arcmin^{-2}$. Circles represent the position of sources detected by the wavelets algorithm in the HRI image.

correction was applied because the *csmooth* algorithm works better on the uncorrected data. However the exposure map is quite flat and we further checked that any feature present in the exposure map does not affect our conclusions.

Figure 2.21 shows a large number of pointlike sources present in the NGC 1399 field, most of which were unresolved in the HRI image. We marked with circles the sources detected in the HRI field (see § 2.2.9). The *Chandra* data show that sources 2, 11 and 5, identified as single sources in the HRI image, are instead multiple sources.

The filamentary structures found in the HRI image (Figure 2.4) are present in the

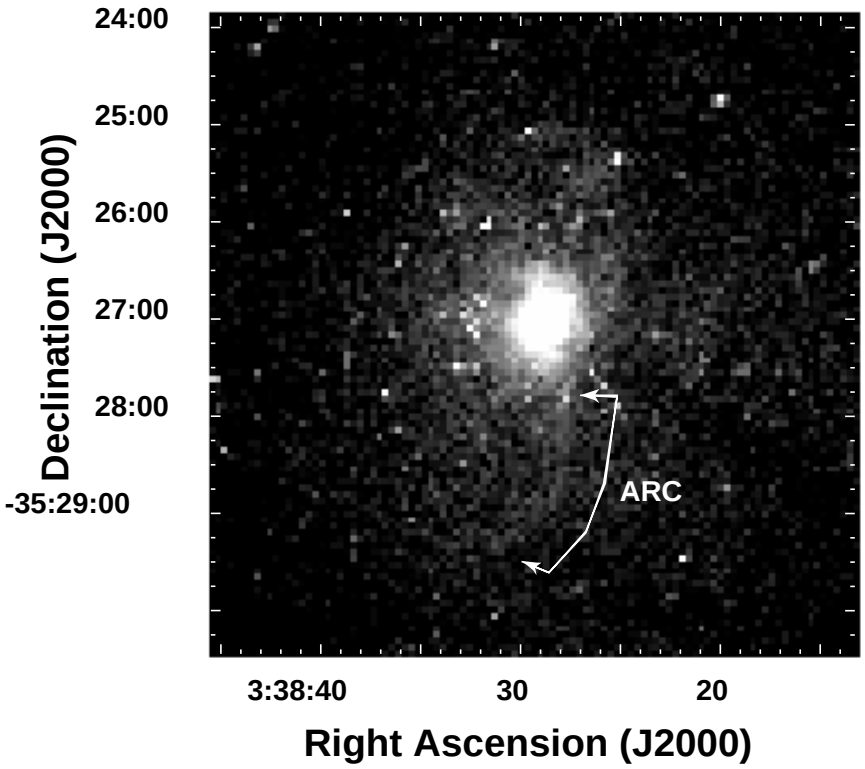

Fig. 2.22.— Raw 4 arcsec/pixel *Chandra* image of NGC 1399. The long arc following the Western edge of the radio lobe is visible South of NGC 1399.

Chandra image as well. The 'arm' protruding on the Western side and the 'voids' in the X-ray emission are clearly seen. The hypothesis that the filamentary structures may be due to the presence of a large number of pointlike sources unresolved in the HRI image, is ruled out by *Chandra* data. In fact the *csmooth* algorithm clearly separates point sources from the extended structures (Figure 2.21) and shows that the two components are not spatially correlated.

The correspondence between the halo features and the radio jets/lobes, discussed in § 2.2.8, are confirmed. Moreover the *Chandra* data revealed the presence of a long arc extending South that follows closely the Western edge of the radio lobe. The arc is better visible on the raw *Chandra* image shown in Figure 2.22. This feature has a low statistical significance (2σ) but the correlation with the radio lobe argues in favor of a real structure.

2.3. DISCUSSION

The study of galactic and cluster gaseous halos has often been based on the assumption of homogeneity and spherical symmetry. The deep HRI image of the NGC 1399 halo has shown instead significant departures from these simplified assumptions. Here we briefly summarize the result of our analysis, and then discuss their physical implications.

We model the X-ray brightness distribution of NGC 1399 with three distinct components: (1) a central component (dominating for $r < 50$"), coincident with the optical galaxy; (2) a 'galactic' component (50" $< r \leq$ 400") displaced South-West of NGC 1399 and (3) an ellipsoidal 'cluster' component ($r >$ 400") centered North-East of the optical galaxy. The cooling times of the central and galactic components are smaller than the Hubble time, suggesting the presence of a central cooling flow. The binding mass estimates, obtained assuming hydrostatic equilibrium, revealed that the dynamics of the central component are dominated by stellar matter while, at radii larger than 2 arcmin there is a large dark matter halo with two distinct components dominating respectively on galactic and cluster scales.

We also found significant filamentary structures and cavities in the X-ray emission. Some of these structures are correlated with the morphology and the position of the radio jets and lobes of NGC 1399, suggesting interactions between the radio emitting plasma and the hot gas.

Finally we used a wavelets based algorithm to detect 46 sources in the HRI field, 8 of which show significant time variability. Their distribution is consistent with the background source distribution at the 3σ level. However there is excess over background counts centered on NGC 1399. The presence of a large number of pointlike sources near the galaxy center is further confirmed by *Chandra* data.

2.3.1. Origin of the Central X-ray Peak

The center of the gaseous halo is occupied by a strong emission peak (see Figure 2.3a) centered on the optical galaxy. Such emission is often found in cooling flow galaxies (Canizares, Stewart, & Fabian 1983; Kim & Fabbiano 1995; see also Fabian, Nulsen & Canizares 1991) because of the higher density of cooler hot gas in the galactic center. RFFJ revealed the presence of a cooler region within the central 1.5 arcmin (14 kpc); this is compatible with the extent of the region dominated by the X-ray peak, as shown by the radial profile in Figure 2.11. Moreover both the central and galactic components have cooling times below the Hubble time (assumed to be $\sim 10^{10}$ years) within respectively 250" (23 kpc) and 350"

(32 kpc), so that significant cooling must have taken place. The cooling time of the cluster component, instead, is compatible with the Hubble time, suggesting that the cooling flow is mainly of galactic origin.

The alternative hypothesis that the central peak can be due to the presence of a nuclear source (Jones et al. 1997) is clearly ruled out by our data, because the observed profile (Figure 2.5) is wider than the HRI PRF even taking into account the PRF uncertainties. The difference between the optical (with slope $\alpha \sim -1.6$, Hilker et al. 1999a) and X-ray profiles ($\alpha \sim -2$ for the central component, see § 2.2.4) seen in Figure 2.9 also suggests that is unlikely that the central peak could be due to stellar sources. Allen, di Matteo & Fabian (2000) analyzing ASCA data, found that the addition of a power-law component to their NGC 1399 spectral model significantly improves the quality of the fit. They notice that the luminosity of the power-law component is compatible with the contribution expected from a population of unresolved hard X-ray binaries. However, the HRI count rate that would be produced by this power-law component falls more than an order of magnitude below the inner component count rate. We can thus exclude that this hard discrete population dominates the central component emission.

The gravitational mass estimate derived from the hydrostatic equilibrium (equation 1.35) shows that the hot gas within 100" follows closely the stellar mass profile. This result is independent on the assumed temperature profile (Figure 2.15) being mostly determined by the hot gas density profile. These X-ray data are thus in excellent agreement with the optical mass determinations of Saglia et al. (2000) who find no evidence of dark matter in the galaxy core.

The origin of the central density enhancement may be due to hot gas inflow within the inner 1 arcmin. The deprojection technique described in § 2.2.6 allowed to derive the cumulative gas mass profile of the central component (Figure 2.15). According to the mass deposition rate measured by RFFJ, which is in good agreement with our data, we expect to find $\sim 2.5 \times 10^9$ $M_\odot$ of deposited gas within the central 60" ($\sim$ 5 kpc) over 10^{10} yr, while we only observe $\sim 2 \times 10^8$ $M_\odot$ in the hot phase. Taking into account a possible larger than line-of-sight central absorption, the observed mass would increase of $\sim 30\%$, but the deposition rate would also increase (see RFFJ), so that the result remains almost unchanged. This difference suggests that $\sim 90\%$ of the hot gaseous mass that reached the inner regions of NGC 1399 has cooled enough to become invisible in X-rays. However RFFJ argue that the missing mass is not seen in any other phase. The situation gets even worse considering that we are ignoring stellar mass losses which must be considerable since the metallicity of the ISM in the galactic center is consistent with stellar values (Buote 1999; Matsushita, Ohashi & Makishima 2000). If the age of the cooling flow is lower than 10^{10} yr, this disagreement

would be reduced. Equating the observed hot gas mass to the amount expected from the cooling flow, we estimate a lower limit of 10^9 years to the age of the cooling flow.

We must notice that the latest studies of cooling flows in clusters and galaxies with Newton-XMM are revealing that the classical cooling flow model is not able to reproduce the observed temperature distributions (Peterson et al. 2001; Kaastra et al. 2001; Tamura et al. 2001). Matsushita (2001a) has shown that taking into account only the central region ($r < 1.5r_e$) of NGC 1399, $\beta_{spec} \sim 1$ indicating that the gas temperature is in good agreement with the stellar velocity dispersion (§ 1.4.1). This result suggest a correlation of the central component with the stellar population. Moreover Makishima et al. (2001) proposed that the cooler halo component found in the center of galaxy clusters is due to the structure of the gravitational well around cD galaxies, rather than to the presence of a cooling flow. An alternative to the cooling-flow scenario is thus emerging, which may provide a good explanation for the presence of the central emission peak. We will discuss this possibility in detail in section 5.2.

2.3.2. Dynamical Status of the Halo

Gravitational Effects

The X-ray brightness profiles (Figure 2.9) shows that past 1 arcmin the hot gas distribution is more extended than the stellar distribution. If the gas is in hydrostatic equilibrium, additional matter is required to explain this broader distribution. The change in slope of the X-ray brightness profile for $r > 400$" further requires the presence of two components that we identified with the 'galactic' and 'cluster' halo. This complex distribution was previously found by Ikebe et al. (1996) using the ASCA data, and explained in terms of a different concentration of dark matter on galactic and cluster scales (Ikebe et al. 1996; Makishima et al. 2001). Our data further show that this galactic component is not correlated with stellar matter, which is even more concentrated (Figure 2.15b) and dominates the dynamics of the galactic core.

The kinematics inferred from the GCs and PNe (see Figure 6 of Kissler-Patig et al. 1999) indicate that for $1' < r < 16'$ (5 kpc$< r <$90 kpc) from the galaxy center, the velocity dispersion increases with radius. This result is consistent with our measurements and suggests either the presence of a significant amount of dark matter associated with the outer radii of NGC 1399 or equivalently that the outer galactic dynamics is dominated by the cluster potential.

We must notice however that while on galactic scales the mass profiles may be explained

by the presence of dark matter, the deviations from symmetry, i.e. the offset between the stellar component (consistent with the central component) and the galactic dark halo, are hardly explained in the galaxy formation framework. For this reason in next sections we take into account possible departures from equilibrium.

Galaxy-Galaxy Interactions

An alternative scenario has recently been advanced by Napolitano, Arnaboldi & Capaccioli (2001, in preparation), that could explain our results by means of galaxy interactions. Their calculations show that the energy injection due to galaxy-galaxy encounters can account for the outer galaxy dynamics as seen in PNe and GCs, and is in agreement with the observed X-ray temperature profile. In this case there would be no need for additional dark matter in the 'galactic' halo. Support for the tidal interaction picture comes from Kissler-Patig et al. (1999) who showed that the GC system of NGC 1399 is 10 times more abundant than those of neighbors galaxies, while their properties are very similar. In the hypothesis that all galaxies initially had the same number of GCs per unit luminosity, the excess around NGC 1399 may be compatible with tidal stripping of GCs from nearby Fornax galaxies.

The effects of tidal interactions on the gaseous halos of elliptical galaxies have been explored by D'Ercole, Recchi & Ciotti (2000, hereafter DRC). They found that the interaction strongly affects the gas flow, altering the ISM density and thus increasing the cooling speed and luminosity. This mechanism is enhanced when energy injection from SNe Ia is included and the gas remains turbulent independently from the epoch of the encounter. In this process the surface brightness is scarcely affected and the global isophotes remain circular, although locally distorted. The DRC model predicts that the gas inflow produces steeper profiles in the central regions of the galaxy in the moment of maximum luminosity, indicating that the tidal perturbations may contribute to the formation of central brightness peaks such as the one seen in the NGC 1399 core. The steep slope of the galactic component (Table 2.2) too may be due to tidal gas stripping because the galaxy undergoes significant mass losses (up to 50%) in the outer regions. However, we must notice that in the case of NGC 1399, the effect of tidal stripping may be smaller than what expected from the DCR models because PSPC data (Jones et al. 1997) suggest a lower SN rate than assumed by D'Ercole and collaborators.

For these models to be consistent with the X-ray observations, tidal interaction must strongly affect the halo density distribution: the increase in the M/L ratio past 2 arcmin (Figure 2.15) is mainly determined by the shallower slope of the gas density profile in the outer galactic regions, since the isothermal model still exhibits the multi-component behavior (§ 2.2.6). Thus a simple temperature increase would not produce the observed agreement

with the optical data. Such strong profile alterations are not seen in the DRC simulations. Conversely Barnes (2000) found that encounters between galaxies of different masses can produce both radial profiles with a central peak and a 'shoulder' similar to our multi-component structure and azimuthal asymmetries as those seen in the NGC 1399 galactic halo. However his simulations also show that the stellar profile follows the gas profile, which is not seen in our data.

The X-ray surface brightness analysis (§ 2.2.3) revealed the presence of complex structures in the galactic halo. We have shown in § 2.2.5 that these brightness fluctuations are not due to artifacts of the smoothing algorithm, because they are present in the residuals of the bidimensional model, and have high statistical significance. Due to the weak dependence of the HRI spectral response on the temperature around 1 keV (see Clarke, Harris & Carilli 1997), they must be due to local density fluctuations of the hot gas. While some of these features can be due to the interaction between the radio jets and the surrounding ISM (§ 2.2.8), most of them are not related to any evident radio or optical feature and are spread all around the galaxy, suggesting a 'disturbed' nature of the whole halo.

It is possible that these structures are the signature of interaction between the NGC 1399 halo and other Fornax galaxies. In fact DRC predict significant density fluctuations in the hot gas and the formation of filamentary structures near the galaxy center as a consequence of galaxy-galaxy encounters. It's not easy to determine if these perturbations are due to the nearby NGC 1404 or to more distant members because, according to DRC, the perturbing effects lasts several Gyrs. We searched for possible signatures of interactions between NGC 1399 and NGC 1404 looking for excess emission in the region between the two galaxies. The slight excess we found is only significant at the 2σ level, so that no significant conclusion can be drawn from our data.

Ram Pressure

A different scenario that could explain the cluster and galactic halo displacement is one in which NGC 1399 is moving in the Fornax cluster potential, thus experiencing ram pressure from the cluster hot gas. The radial profiles in Figure 2.9 show a high degree of asymmetry with respect to the optical galaxy. The 2D models indicate that the galactic component is displaced $\sim 1'$ (5 kpc) South-West with respect to the X-ray peak (and thus optical galaxy), while the cluster component seems located ~ 5.6 arcmin (31 kpc) North-East of NGC 1399. Jones et al. (1997) argue that this displacement is compatible with the hypothesis that the galaxy is slowly moving (40 km s^{-1}) South-East in a larger potential. This would explain the displacement of the galaxy with respect to the cluster component but not the one of the

galactic halo. In the ram pressure scenario, the displacement and large scale asymmetry of the 'galactic' halo may suggest that NGC 1399 is not sitting at the very center of the cluster potential and is slowly moving North-East toward the 'cluster' component.

The effect of ram stripping has already been observed in nearby galaxies. For instance Irwin & Sarazin (1996) observed the presence of a very irregular halo in the Virgo galaxy NGC 4472. They found a steeper gradient in the X-ray emission in the direction of the cluster center associated with a temperature enhancement. They calculate that ram stripping is able to explain the observed halo features if the galaxy is moving at ~ 1300 km s^{-1} in the cluster potential. Their ROSAT HRI images also revealed filamentary structures and holes in the galactic halo, very similar to the features that we observed in the adaptively smoothed image of the inner halo (Figure 2.4). Additional evidence that galaxies moving in the cluster environment can produce filaments of cooler gas behind them were found by David et al. (1994) or Fabian et al. (2001b).

The accurate simulation of dynamic stripping in cluster and group elliptical galaxies performed by Toniazzo & Schindler (2001), show that the effect of dynamic stripping depends on the galaxy orbit and the duration of the subsonic and supersonic phases which determine the balance within gas losses and accretion onto the galaxy. In general their simulations reveal the formation of complex and elongated tails behind the galaxy (similar to those seen in NGC 4472) and strong decentering of X-ray isophotes due to supersonic stripping. Such irregular structures are not seen in the NGC 1399 galactic halo which seems instead rather circular ($\epsilon_{Galactic} = 0.02$, see Table 2.2).

A very rough estimate of the velocity of NGC 1399 can be obtained supposing that the displacement of the optical galaxy, coincident with the X-ray centroid, with respect to the galactic halo is due to the deceleration of the halo caused by ram pressure from the cluster component. In the hypothesis that the motion is highly subsonic, we can treat the different components as homogeneous spheres and calculate the initial velocity required to produce the observed displacement after a time $t = 10^9$ yr due to the ram pressure of the cluster halo $P \sim \rho_{cluster} v^2$. Using the parameters derived form the bidimensional model (§ 2.2.5): $\rho_{galaxy}/\rho_{cluster} \sim 4$, $R_{galaxy} \sim 4'$ and a displacement $\Delta S \sim \frac{1}{2}R$, we obtain an initial velocity of ~ 10 km s^{-1}, consistent with the initial assumption of subsonic motion. Even considering a more recent interaction where $t = 10^8$ the galaxy motion remains highly subsonic (~ 100 km s^{-1}). This result is in agreement with the observations, showing that the halo morphology is only weakly distorted. In conclusion, even though extreme projection effects may hide stronger stripping features, ram pressure may be causing the galaxy halo displacement but seems unlikely to be responsible for the observed inner halo structure of NGC 1399.

Cluster Merging effects

For what concerns the elongated cluster halo component, in many cases irregular features in the cluster halos seems associated with merger events (see for instance Sun et al. 2000; Mazzotta et al. 2000). Simulations of cluster merging (Roettiger et al. 1996) show that elongation and twisting of the X-ray isophotes are a general result of such interactions. In the case of the Fornax cluster Drinkwater, Gregg & Colless (2000) found evidence of a subcluster 3 degrees South-West of NGC 1399 centered on NGC 1316 (Fornax A). They claim that the two components are at the early stage of merging; in this case merging is unlikely to be the cause of the elongation of the cluster X-ray isophotes. To further study the dynamical status of the cluster halo we would need temperature maps of the whole cluster, as can be obtained with *Chandra* or XMM.

It is worth noticing that the X-ray centroid of the cluster component is displaced with respect to the optical distribution of Fornax cluster galaxies, which tend to concentrate South-West of NGC 1399 (see Figure 1 from Hilker et al. 1999b and Figure 3 from Drinkwater, Gregg & Colless 2000). If the merging picture is confirmed, this may imply that the galaxies in the two subclusters are infalling in the global potential well faster than the associated gaseous halos.

Kim & Fabbiano (1995) compared three X-ray dominant galaxies in poor groups: NGC 1399, NGC 507 and NGC 5044. They show that even if these galaxies have similar properties (temperatures, cooling core) their X-ray brightness profiles are very different. This suggests that the shape of the potential and the mass deposition mechanism may vary from galaxy to galaxy. If environmental effects (tidal interactions, ram pressure stripping) are important factors in determining the NGC 1399 halo structure, they must be considered as well in order to explain the observed differences.

2.3.3. X-ray/Radio Interactions

Signs of interaction between radio jet/lobes and the surrounding gaseous medium have been reported in powerful radio galaxies (see for instance Carilli, Perley & Harris 1994 for Cygnus A; Böhringer et al. 1993; McNamara et al. 2000; Fabian et al. 2000 for evidence of such interaction in clusters hosting powerful radio sources). NGC 1399 is a faint radio galaxy whose radio lobes are entirely contained within the optical galaxy. Nevertheless the structures seen in Figure 2.16 suggest that the same mechanisms at work in more powerful sources may be responsible for some of the galactic halo structures. The residual image in Figure 2.17 shows excess emission on both sides of the nucleus and a lack of X-ray emission along the radio jets

in the inner 15" ($\sim$ 1.4 kpc), as if the radio jets are displacing the ambient gas. For $r \sim 25$" ($\sim$ 2.3 kpc) more X-ray emission is seen in the North and South part of the galaxy, aligned with the direction of the radio jets.

Clarke, Harris & Carilli (1997) have studied, by means of hydrodynamical simulations, how these features are produced during the propagation of the radio jet trough the ICM. They show that, for a ~ 1 keV gaseous halo and a detector response similar to the ROSAT HRI (see their Figure 8), we expect to see excess emission located on the side of the jets, due to the shocked gas near the tail of the radio lobes, as the one seen in Figure 2.16 (region **A**) and in Figure 2.17.

In coincidence with the radio lobes, X-ray enhancements or deficits are expected depending on the thickness of the shocked gas Δr with respect to the lobe radius r. Near the edge of the radio lobe, where $r \geq 3.4\Delta r$, the shocked gas density is high enough to produce a brightness enhancement. On the contrary, in the tail of the lobes the compressed gas had time to expand, so that $r < 3.4\Delta r$ and the X-ray brightness is diminished, producing a 'cavity'. This picture is very similar to what we see in our data. Features **B** and **C** in Figure 2.16 may suggest respectively the presence of a cavity produced by the Southern lobe in the ICM and the excess emission associated with the edge of the lobe. The alternative hypothesis, that the excess is due to the presence of a bow shock at the leading end of the lobe, seems unlikely both because Carilli and collaborators showed that the bow shock is hardly seen at energies < 4 keV and because the signatures of bow shocks are usually sharper than the one seen in our data, showing up as compact bright spots or arcs. The *Chandra* image also revealed the presence of a long arc South of NGC 1399. The steeper gradient of the radio emission on the Western side of the Southern lobe, with respect of the Eastern side, suggests that this feature may represent a layer of hot gas compressed by the radio emitting plasma.

Signatures of interaction with the ICM do not show up so clearly in the Northern lobe, but this could be due to projection effects (see for instance Brunetti et al. 2000; Finoguenov & Jones 2000). The brightness enhancement near the West side of the lobe could be due to the thin layer of compressed gas surrounding the lobe while the steeper radio gradient near region **D** suggests that the lobe is avoiding a region of higher gas density. Indeed the crude estimate indicates that the pressure of the bubble (§ 2.2.8) can be up to 4 times higher than that of the surrounding ISM. An upper limit of $k \simeq 420$ on the ratio of the electron to heavy particle energy (or alternatively a lower limit of 0.005 on the filling factor) can be derived by matching the radio pressure to the thermal pressure of the bubble (Figure 2.18), in agreement with Killeen, Bicknell & Ekers (1988).

As discussed in § 1.3.2, Inverse Compton (IC) scattering of Cosmic Background photons by the radio emitting particles is often considered as an alternative process to explain the X-

Table 2.4: Southern lobe magnetic field strenght.

η	ϕ (rad)	ν_1 (GHz)	k	S_X (ergs s^{-1}cm^{-2}Hz^{-1})	B_{ME} (μG)	B_{IC} (μG)	B_{ME}/B_{IC}
1	$\pi/2$	1.00×10^{-2}	1	2.90×10^{-32}	4.90	0.37	13.3
1	$\pi/6$	1.00×10^{-2}	1	2.90×10^{-32}	6.59	0.54	12.2
1	$\pi/2$	1.00×10^{-2}	100	2.90×10^{-32}	15.0	0.37	40.9
1	$\pi/2$	1.00×10^{-4}	1	2.90×10^{-32}	4.90	0.37	13.4
0.1	$\pi/2$	1.00×10^{-2}	1	2.90×10^{-32}	9.46	0.37	25.7
0.01	$\pi/2$	1.00×10^{-2}	1	2.90×10^{-32}	18.3	0.37	49.7
1	$\pi/2$	1.00×10^{-2}	1	3.64×10^{-33}	4.90	1.16	4.21
1	$\pi/6$	1.00×10^{-2}	1	3.64×10^{-33}	6.59	1.7	3.85

Note - The calculation uses equations (1.17) and (1.20) assuming the following parameters: radio spectral index $\alpha_r = -0.8$, radio flux density $S_r = 0.0825$ Jy at $\nu_r = 1.465$ GHz, lobe diameter $\theta = 28$" and path lenght through the source $s = 25.7$ kpc. The X-ray flux S_X density is calculated at 1 keV assuming a galactic absorption of 1.3×10^{20} cm^{-2}; the upper syncrotron cutoff is taken to be $\nu_2 = 100$ GHz.

ray brightness enhancements near radio lobes (Harris & Grindlay 1979; Kaneda et al. 1995). We have evaluated this possibility for the X-ray excess near the edge of the Southern radio lobe of NGC 1399, following Feigelson et al. (1995), and comparing the minimum energy field strength B_{ME} (equation 1.20) with the magnetic field B_{IC} (equation 1.17) required to produce a measured ratio of radio to X-ray flux. We estimated the ratio B_{ME}/B_{IC} for a grid of values of the involved parameters: the filling factor η of the syncrotron emitting region, the angle ϕ between the magnetic field (assumed to be uniform) and the line of sight, the lower cutoff frequency ν_1 of the radio syncrotron spectrum, the ratio k of energy in heavvy particles with respect to electrons and the X-ray flux density S_X. We used the radio flux for the Southern lobe measured by Killeen, Bicknell & Ekers (1988), corrected for the fact that just half of the lobe contributes to the X-ray excess. The results are shown in Table 2.4. The X-ray flux was measured from the residuals shown in Figure 2.12, assuming that all the excess over the 2D model is due to IC scattering; this value may vary of 25% depending on the region used for the extraction, so that we included both the upper (3.64×10^{-33} ergs s^{-1}cm^{-2}Hz^{-1}) and lower (2.90×10^{-32} ergs s^{-1}cm^{-2}Hz^{-1}) flux limits in Table 2.4. We find that it is unlikely that more than a few percent of the excess near the edge of the Southern radio lobe may be due to IC scattering, since the ratio B_{ME}/B_{IC} is always > 1 for any choise of the parameters involved in the calculation.

Pressure confinement of the radio lobes (Killeen, Bicknell & Ekers 1988) is supported by our data (Figure 2.18). If the inclination of the radio source is $< 45°$, the radio jets remain collimated up to the radius within which the high density central component dominates ($\sim$ 50", Figure 2.18) and diffuse in lobes as soon as they enter in the lower density environment. A larger inclination is unlikely because the thermal pressure of the cluster component (long-dashed line in Figure 2.18) is of the same order of magnitude as the radio lobes pressure, and would probably not be able to confine the radio emitting plasma, if this was extending at greater distances.

Finally, we analyzed the possibility that the power-law component found in the spectral model of Allen, di Matteo & Fabian (2000) for NGC 1399 (see § 2.3.1) may be due to an active nucleus. Their estimated flux (converted to our adopted distance) is twice the value expected from our upper limit on a possible nuclear source, adopting their best fit parameters. Considering that Loewenstein et al. (2001) further reduce this upper limit by an order of magnitude it appears that the bulk of the power-law emission comes from the discrete source population revealed by the *Chandra* data (see Figure 2.21).

2.3.4. Discrete sources

The presence of a population of individual X-ray sources in E and S0 galaxies was first suggested by Trinchieri & Fabbiano (1985). Additional evidence was then provided by ROSAT and ASCA observations (e.g. Fabbiano, Kim & Trinchieri 1994; Kim et al. 1996; Matsumoto et al. 1997). These X-ray source populations are now been detected down to much lower luminosities with *Chandra* (e.g. Sarazin, Irwin & Bregman 2000, 2001). The HRI data demonstrate the presence of such population, possibly of accretion binaries, also in NGC 1399. This result is confirmed by the *Chandra* data which reveal a large number of pointlike sources surrounding the galaxy, many of which associated with globular clusters (Angelini, Loewenstein & Mushotzky 2001). This population of accretion binaries is probably responsible for the hard spectral component (Buote 1999; Matsushita, Ohashi & Makishima 2000; Allen, di Matteo & Fabian 2000) required to fit the high energy spectrum of NGC 1399. As demonstrated by comparing the 5" resolution ROSAT HRI image with the 10 times sharper *Chandra* ACIS image, subarcsecond resolution is essential for the study of X-ray source populations in galaxies.

Chapter 3

NGC 1404

3.1. INTRODUCTION

NGC 1404 is a bright early-type located ~ 10 arcmin South-East of NGC 1399, within the Fornax cluster. The galaxy is classified as an elliptical in the the RC3 catalogue (E1; de Vaucouleurs et al. 1991) and in the RSA catalogue (E2; Sandage & Tammann 1981). However kinematical studies have shown that NGC 1404 is likely to be a rotationally supported system and a thus misclassified S0 galaxy (D'Onofrio et al. 1995; Graham et al. 1998).

Due to her proximity to the dominant Fornax galaxy, in the X-ray band NGC 1404 has been usually studied in association with its brighter companion. The first detection of X-ray emission was obtained by the HEAO-1 satellite (Nugent et al. 1983) but the EXOSAT satellite was the first able to separate the NGC 1404 emission from NGC 1399 (Mason & Rosen 1985). The *Einstein* satellite confirmed the presence of an extended halo with $L_X \sim 3 \times 10^{41}$ erg s^{-1} in the 0.2-4.0 keV band (Thomas et al. 1986; Fabbiano, Kim & Trinchieri 1992), and a temperature > 1 keV at the 90% confidence level (Kim, Fabbiano & Trinchieri 1992a).

Loewenstein et al. (1994) analyzed ASCA data finding evidence of a very subsolar metal abundance ($Z < 0.2 Z_\odot$ at the 90% level) in the NGC 1404 halo and a temperature of 0.75 keV, suggesting a strong radial metallicity gradient. These findings were confirmed by Jones et al. (1997) using ROSAT PSPC data ($kT = 0.65$ keV and $Z = 0.16 Z_\odot$). They also found an elongated feature protruding on the SE side of the galaxy interpreted as a signature of ram pressure stripping of the NGC 1404 corona infalling toward the denser NGC 1399 halo. Arimoto et al. (1997) noticed that the ASCA data are compatible with the presence of a hard spectral component due to unresolved point sources. Buote & Fabian (1998) found

that a higher metallicity is allowed if the spectrum is fitted with a two temperature model. The low metallicity is invoked by Irwin & Sarazin (1998b) to explain the soft ROSAT PSPC spectrum.

In their study of a sample of early-type galaxies Brown & Bregman (2000) and Matsushita (2001a) found that the NGC 1404 corona has a higher temperature than other galaxies with similar velocity dispersion and luminosity; they explain this result as a strong environmental influence on the physical status of the halo. Toniazzo & Schindler (2001) simulated the effect of gas stripping on galaxies similar to NGC 1404. Comparing their surface brightness profile to the one measured by Fabbiano, Kim & Trinchieri (1992) they found that their models tend to predict a steeper profile than it is observed. Finally, the need for additional heating, over the one provided by gravity alone, is found by Bregman, Miller & Irwin (2001) using the *Far-Ultraviolet Spectroscopic Explorer* (FUSE) satellite, since the measured cooling rate is lower than the one expected by X-ray measurements.

In this chapter we use the ROSAT HRI resolution to explore the structure of the NGC 1404 corona and the interactions with the surrounding intracluster medium. As for NGC 1399, we adopt $H_0 = 75$ km s^{-1} Mpc^{-1} and a distance of 19 Mpc (1'=5.5 kpc).

3.2. OBSERVATIONS AND DATA ANALYSIS

NGC 1404 was observed at the same time of NGC 1399 since, being located near the dominant Fornax galaxy, it falls within the HRI field of view. For this reason the basic data reduction (aspect correction, exposure correction and composition of the three observations) is the same described in c§ 2.2.1 and 2.2.2. The position of NGC 1404 inside the HRI field is shown in Figure 2.2.

3.2.1. Brightness Distribution and X-ray/Optical Comparison

From Figure 2.2 it is evident that NGC 1404 is missing the large extended halo which surrounds its nearby companion. This is was confirmed by the adaptively smoothed image shown in Figure 2.3a: the X-ray emission of NGC 1404 is almost symmetric and centered on the optical galaxy (Figure 2.3b).

We examined the NGC 1404 halo in greater detail creating an adaptively smoothed image of the galaxy with a 2 arcsec/pixel resolution. Figure 3.1a shows that the hot halo is

circular in the center and becomes slightly elongated in the NE-SW direction past 40" from the center, with an axial ratio of ~ 0.8 at $r = 80$". At larger radii the surface brightness asymmetries are more pronounced: there is a steep gradient on the NW side of the halo and a 'tail' protruding on the SE side of the galaxy. The tail corresponds to the elongated feature reported by Jones et al. (1997) in the PSPC data.

The comparison with the DSS image (Figure 3.1b) shows that the extension of the X-ray halo is consistent with the optical distribution. A more accurate analysis also reveals that the stellar distribution is flattened in the NW-SE direction, i.e. perpendicular to the elongation of the X-ray isophotes. This indicates that the ellipticity of the X-ray isophotes does not reflect the underlying stellar distribution, but is probably due to ram pressure effects.

We notice that the presence of the bright star visible near the edge of the NGC 1404 tail (Figure 3.1b), does not affect our analysis since we didn't detect any stellar X-ray emission in the raw (unsmoothed) HRI data.

3.2.2. Radial Brightness Profiles

We derived the brightness profile of NGC 1404 extracting count rates in 2" annuli centered on the galaxy centroid. The background determination for this galaxy is even more difficult than for NGC 1399 (see § 2.2.4), due to the fact that it is embedded in the halo of its bright companion. Thus we had no other choice than to estimate the background level from the region between 200" and 300" from the galaxy (see Figure 3.2a), obtaining 5.60×10^{-3} counts arcmin^{-2} sec^{-1}. The measured count rates are shown in Figure 3.2a as a continuous line while the background subtracted profile is represented by open circles. The NGC 1404 emission extends out to 110" ($\sim$10 kpc) from the galaxy center and shows no sign of a multi component structure as the one detected in NGC 1399. The surface brightness is almost symmetric (Figure 3.1a) and declines with a power law profile out to 90". Past this radius the effect of ram pressure stripping becomes evident as a sharp cutoff in the radial profile. In Figure 3.2b we can see that in the North-West sector (thin dashed line) the galactic halo suddenly disappears in the X-ray background for $r > 90$" ($r > 8$ kpc) while in the South-East one (continuous line) the emission from the tail, seen in the adaptively smoothed images (Figure 2.3), extends up to ~ 150" (14 kpc).

We fitted the observed radial brightness distribution, within a 90" radius, with a Beta model (equation 1.31). In this case the on-axis PRF we used for NGC 1399 is no longer valid because NGC 1404 is located 10 arcmin South-West of NGC 1399. Although an analytical correction of the on-axis PRF is possible (David et al. 1996), it doesn't take into account the PRF azimuthal asymmetry. We thus convolved the Beta model with the on-axis PRF

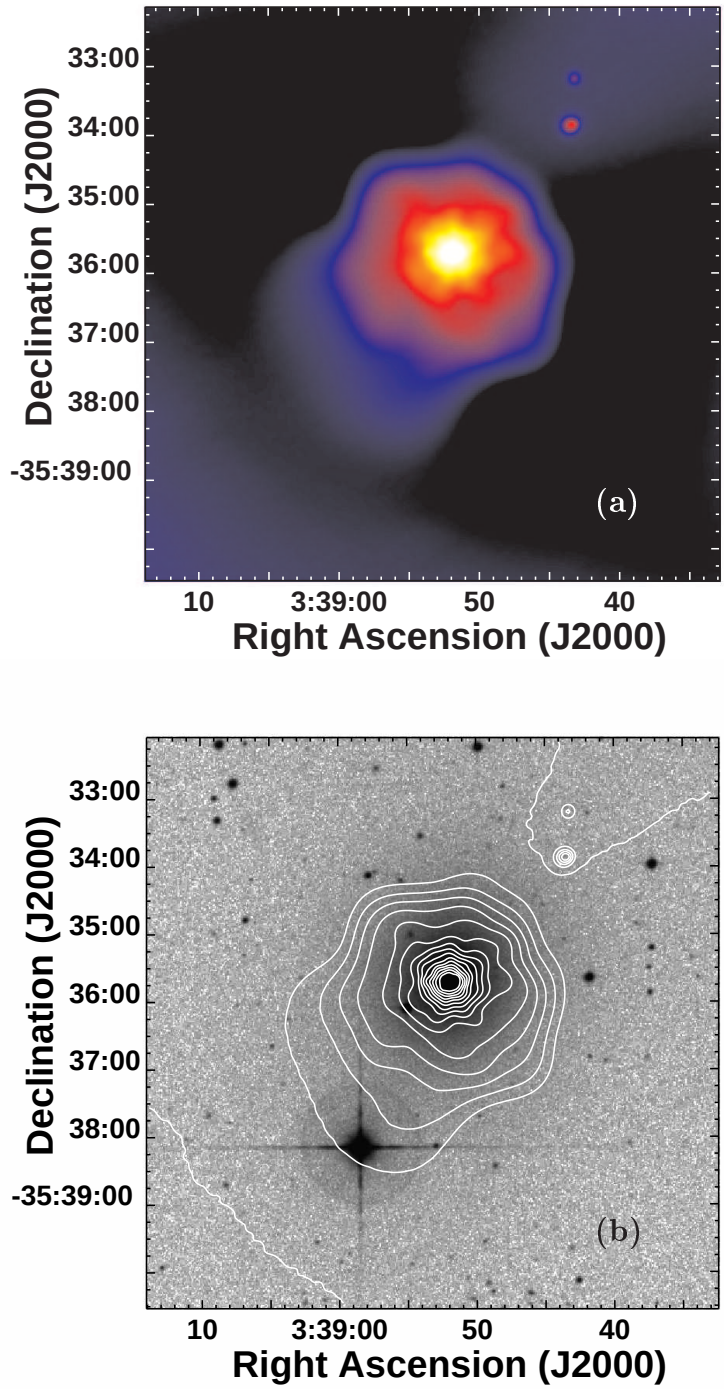

Fig. 3.1.— **(a)** 2×2 arcsec/pixel adaptively smoothed image of NGC 1404 HRI field. Colors from black to yellow represent logarithmic X-ray intensities from 1.1×10^{-3} to 1.3×10^{-1} cnts arcmin^{-2} s^{-1}. **(b)** X-ray brightness contours overlaid on the 1 arcsec/pixel DSS image (logarithmic grayscale). Contours are spaced by a factor 1.3 with the lowest one at 1.4×10^{-3} cnts arcmin^{-2} s^{-1}.

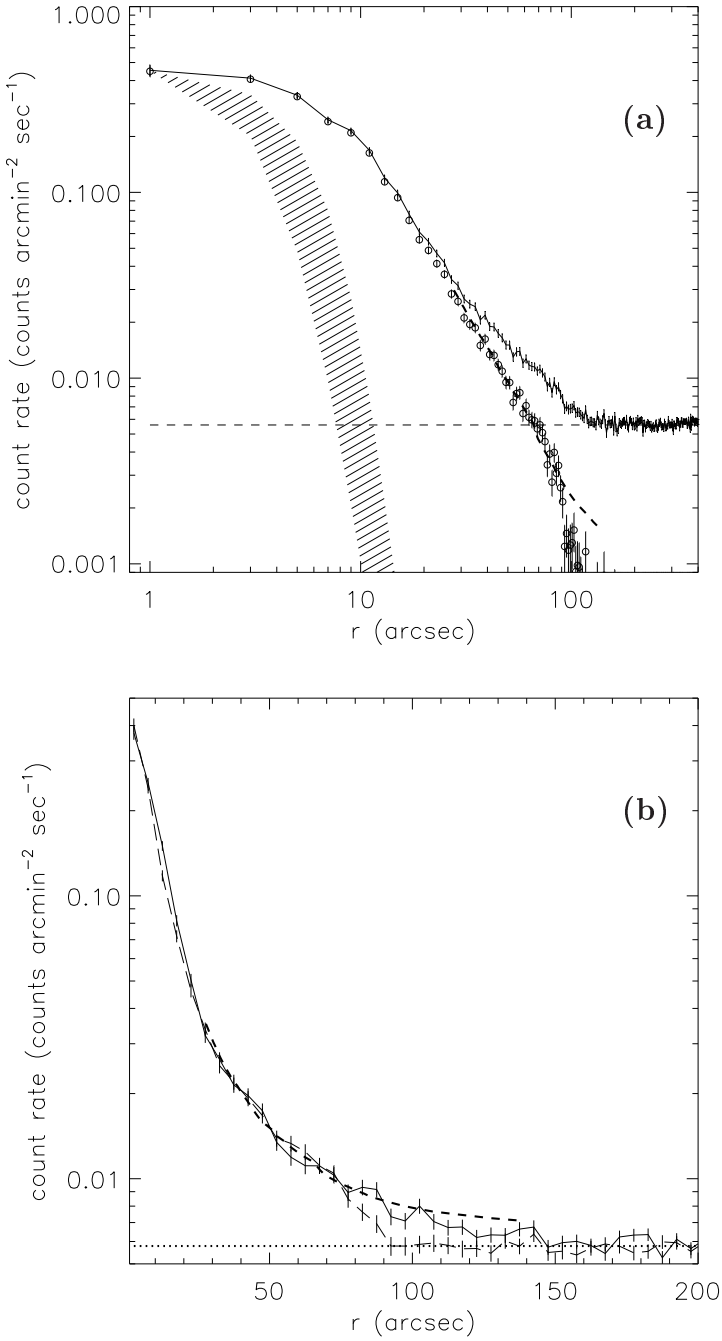

Fig. 3.2.— **(a)** Radial profile of NGC 1404 extracted in 2" annuli (continuous line). Circles represent the background subtracted profile using the count rate measured in the 200"-300" interval (dashed line). The optical profile from Forbes et al. (1998) is shown as a dashed line. The HRI on-axis PRF range is represented by the shaded region. **(b)** Radial profiles extracted in 5" annuli in the North-West (270° <P.A.< 360°, thin dashed line) and the South-East (90° <P.A.< 180°, continuous line) sectors. The optical profiles and background levels are represented respectively by the thick dashed line and the dotted line.

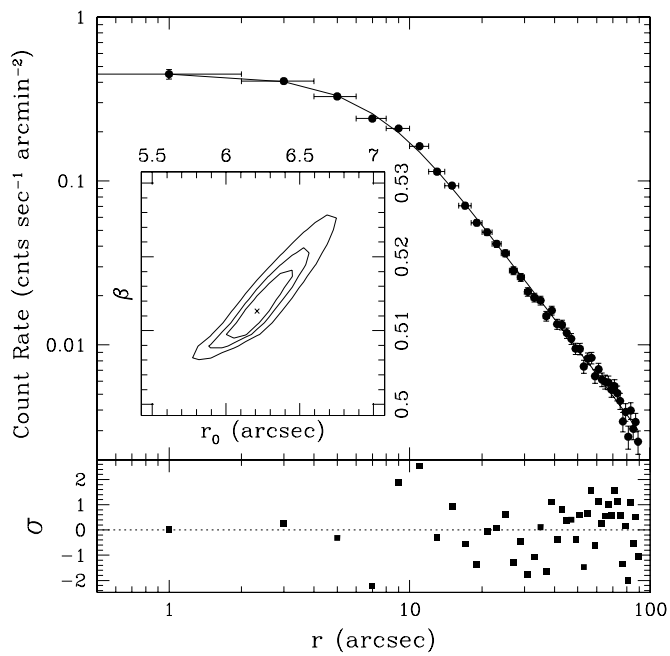

Fig. 3.3.— The best-fit model and residuals of NGC 1404 brightness profile within 90". The 66%, 90% and 99% contour levels relative to the core radius r_0 and slope β are shown in the inner panel.

and considered the resulting core radius as an upper limit to the correct value, obtaining $r_0 = 6.21^{+0.25}_{-0.2}$ arcsec and $\beta = 0.513^{+0.005}_{-0.004}$ with $\chi^2 = 51.5$ for 42 d.o.f. The best fit model is shown in Figure 3.3.

3.2.3. Density, Cooling Time and Mass Profiles

Following the method outlined in § 2.2.6 we derived the electron density, cooling time and mass profiles for NGC 1404. Since the deprojection algorithm tends to enhance the fluctuations present in the brightness profile, we used the best fit model to derive the deprojected electron density. This is possible because the NGC 1404 radial brightness profile was well fitted by a single symmetric Beta model out to 90" (§ 3.2). Figure 3.4a shows the good agreement between the deprojected density derived from the Beta model (continuous line) and the one from the surface brightness profile (filled circles). The discrepancy in the inner 5" is due to the fact that the Beta model is deconvolved for the instrumental PRF. We stopped the deprojection at 80" to avoid uncertainties related to the background subtraction

and to the asymmetries due to ram pressure stripping (§ 3.2), both of which tend to increase the fluctuations at large radii.

The cooling time profile derived from the Beta model is shown in Figure 3.4b and suggests that significant cooling must be present in the NGC 1404 halo because the cooling time is smaller than 10^9 yr within the inner 80" ($\sim$7 kpc). We adopted the cooling function of (Sarazin & White 1987).

The integrated gas mass and the total gravitating mass derived from equation (1.35) are shown in Figure 3.5. We assumed NGC 1404 to have an isothermal profile with $kT = 0.6$ keV (Jones et al. 1997).

3.2.4. Total Fluxes and Luminosities

In the case of NGC 1404 we used a single temperature Raymond-Smith spectrum with $kT = 0.6$ keV and metal abundance 0.2 solar, following Jones et al. (1997). We measured a count rate of 0.117 ± 0.001 counts sec^{-1} within a 150" radius, extracting the background from the 200"-300" annulus. The corresponding (0.1-2.4 keV) flux and luminosity are $f_X = (4.06 \pm 0.03) \times 10^{-12}$ erg s^{-1} cm^{-2} and $L_X = (1.57 \pm 0.01) \times 10^{41}$ erg s^{-1}.

3.3. DISCUSSION

In contrast with NGC 1399, NGC 1404 possesses a very regular and symmetric halo, well represented by a Beta profile within 90" (8 kpc). The X-ray brightness profile falls as $\sim r^{-2.08\pm0.03}$, in good agreement with the optical brightness profile $\Sigma \propto r^{1.9\pm0.1}$ (Forbes et al. 1998). Since the X-ray emission measure is a function of n_e^2 (equations 1.5 and 1.7) it is easy to see that $\rho_g^2 \sim \rho_{stars}$. If the gas and the stars are two isothermal spheres experiencing the same gravitational potential, equations (1.26) and (1.29) imply that $T_g \sim 2T_{stars}$ (Fabbiano 1989). This is further supported by the ROSAT PSPC spectral data, which yield $\beta_{spec} \sim 0.6$ (Brown & Bregman 1998; Matsushita 2001a), suggesting that the gas distribution is produced by the same gravitational potential that is binding the stellar population, out to $r \sim 80$" ($\sim$ 7 kpc; Figure 3.2b).

This scenario is in disagreement with the finding that luminosities and temperatures of X-ray compact galaxies are well explained by kinematical heating of gas supplied by stellar mass losses (Matsushita 2001a), which should give $\beta_{spec} \sim 1$. However Matsushita (2001a) notice that NGC 1404 is a peculiar galaxy, in the sense that it is significantly brighter than

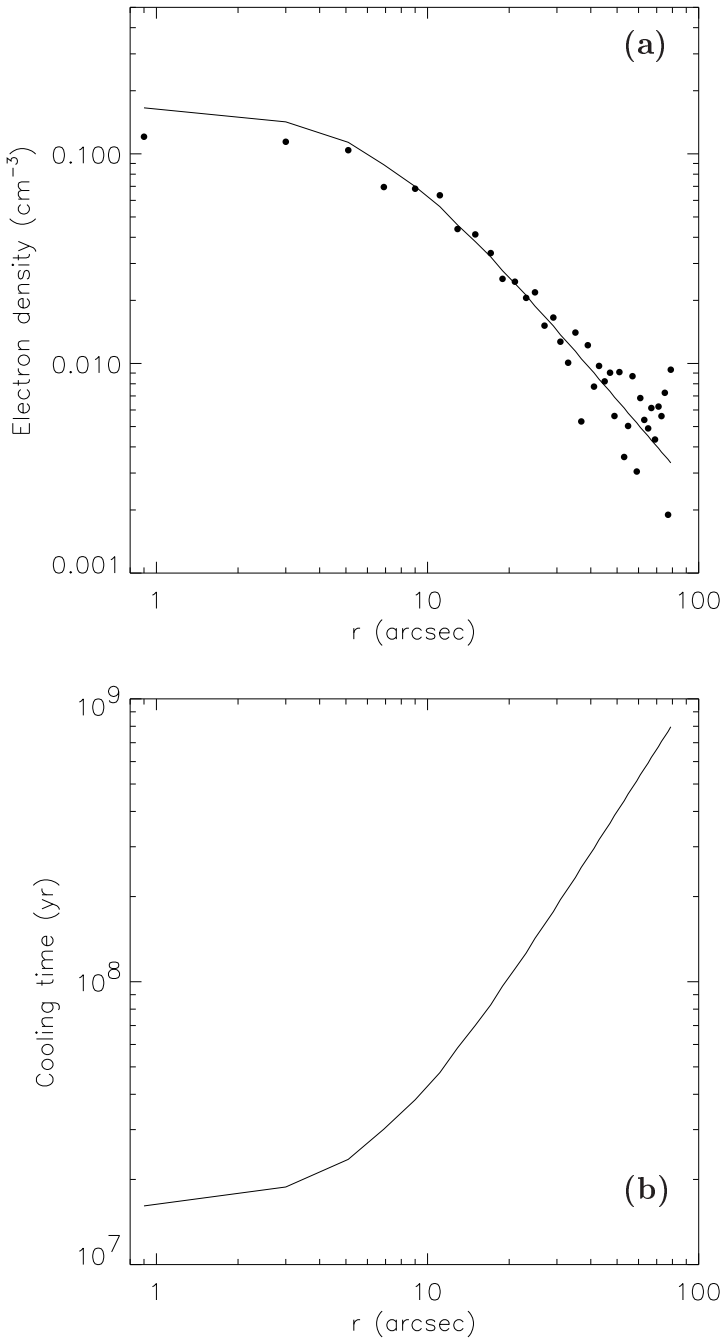

Fig. 3.4.— **(a)** Deprojected electron density profile of NGC 1404. The filled circles represent the profile obtained from direct surface brightness deprojection while the continuous line shows the smoother profile obtained by deprojecting the best-fit Beta model. **(b)** Cooling time profile derived from the best fit Beta model.

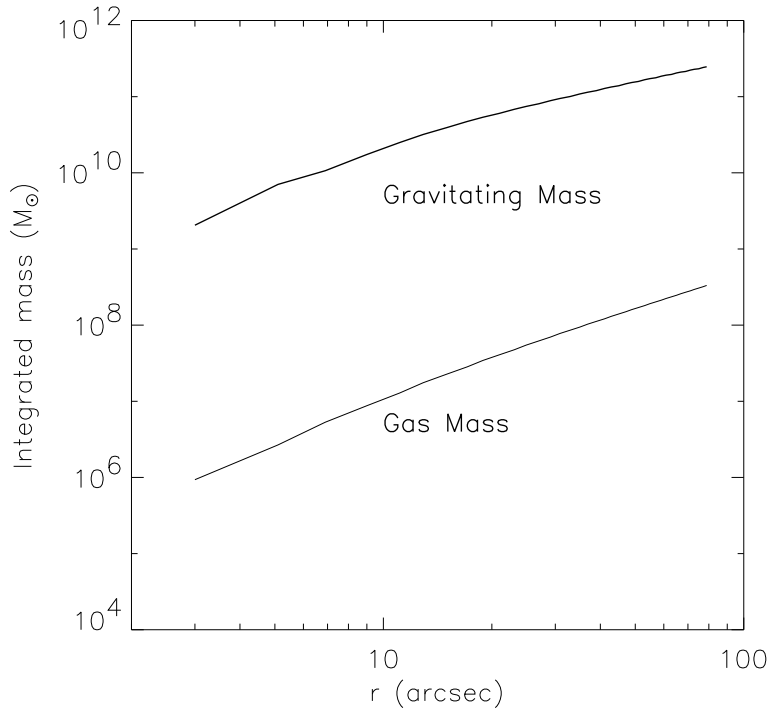

Fig. 3.5.— Integrated mass profiles of NGC 1404 derived from deprojection. The total gas mass is represented by the lower line while the total mass derived using equation (1.35) is shown by the upper line.

other compact ellipticals with the same optical luminosity. In fact, without being a central cluster galaxy, its luminosity is of the same order of magnitude of NGC 1399 (10^{41} erg s^{-1}). She explains this result in term of interaction with the ISM.

Indeed at radii larger than 80" the influence of dynamic stripping is evident from the presence of an elongated tail on the South-East side of the galaxy and the steep surface brightness gradient on the opposite side (Figure 2.3 and 3.2b). These features are aligned with the position of NGC 1399, suggesting that they may be due to the infall of the galaxy toward the cluster center. Ram pressure may be also responsible for the flattening of the X-ray isophotes in direction perpendicular to this motion. In fact, if the hot gas is just experiencing the same potential of the stellar component, we would expect an elongation in the same direction of the optical isophotes.

However the effect of ram stripping from the ICM is to reduce the X-ray luminosity, removing hot gas from the galactic halo (Toniazzo & Schindler 2001). The regularity of the X-ray brightness profile and its similarities to the optical profile within 90" ($\sim$ 8 kpc)

implies that either the stripping efficiency is low or that it affects significantly only the outer galactic regions. This is further supported by the fact that our brightness profile is shallower than expected from simulations of dynamically stripped galaxies performed by Toniazzo & Schindler (2001), even though they notice that their models may be overestimating the importance of the cooling processes. An alternative and more promising explanation is represented by the stifling of galactic winds (§ 1.6). In fact the presence of the dense NGC 1399 halo may both increase the X-ray luminosity and raise the halo temperature (see for instance Brown & Bregman 2000).

The gas, cooling time and total mass profiles derived in § 3.2.3 are in the same range of those of the central component of the NGC 1399 halo, within the inner 80". This seems in conflict with the different dynamical status of the halo core of NGC 1399, suggested by the $\beta_{spec} \sim 1$ value found by Matsushita (2001a). The explanation may lie in the presence of the additional and extended halo components (i.e. galactic and cluster components) generally found in cD galaxies and related to the central position inside the cluster potential well (e.g. Makishima et al. 2001). We will discuss further this possibility in § 5.4.

Chapter 4

NGC 507

4.1. INTRODUCTION

NGC 507 is the brightest member of a group of galaxies belonging to a poor system: the Pisces cluster. The latter in turn is part of the Perseus-Pisces supercluster (e.g. Wegner, Haynes & Giovanelli 1993; Sakai, Giovanelli & Wegner 1994), located at ~ 66 Mpc[1] from our galaxy (Huchra, Vogeley & Geller 1999). NGC 507 is classified as E/S0 galaxy (de Vaucouleurs et al. 1991). González-Serrano & Carballo (2000) showed that, while the surface brightness profile follows a *de Vaucouleur* law (equation 1.1) out to ~ 15" from the galaxy center, at larger radii there is significant excess emission over the $r^{1/4}$ profile. Barton, de Carvalho & Geller (1998) studied the galaxy distribution in the surrounding of NGC 507 finding that it is part of a group including ~ 70 members.

The first studies in the X-ray band based on *Einstein* data (Kim, Fabbiano & Trinchieri 1992a,b) measured a luminosity comparable to those of poor clusters ($L_X \simeq 10^{43}$ ergs s^{-1}) with a temperature $kT > 1.5$ keV at the 90% level, and suggested the presence of a cooler core. These findings where confirmed by Position Sensitive Proportional Counter (PSPC) mounted on the ROSAT satellite which revealed extended X-ray emission out to a radius of at least 16 arcmin. Kim & Fabbiano (1995) were able to resolve the cooler region within the central 150", thus supporting the presence of a massive cooling flow, and suggested that cooling clumps may be distributed at large radii. They estimated a hot gas temperature ~ 1.1 keV with no sign of excess absorption over the galactic value. The data constrained the metallicity to be not higher than the solar one.

[1]Assuming $H_0 = 75$ km s^{-1} Mpc^{-1}

Matsumoto et al. (1997) exploited the higher spectral resolution and larger energy range of the ASCA satellite to separate two distinct components in the NGC 507 X-ray spectrum: a soft thermal emission with $kT \simeq 1$ keV and a harder component with $kT \sim 10$ keV probably due to unresolved discrete sources. The ASCA data seem to favor a subsolar metallicity of $\sim 0.3\ Z_{\odot}$. The different metal abundance obtained by ROSAT and ASCA is explained in part by the new analysis performed by Buote (2000b) on the ROSAT PSPC data, which found a steep gradient in the metallicity profile of the hot halo.

NGC 507 is a radio galaxy with a steep radio spectrum and weak core (Colla 1975; de Ruiter et al. 1986; Parma et al. 1986). It may be a source with particularly weak jets, or possibly a remnant of a radio galaxy whose nuclear engine is almost inactive and whose luminosity has decreased due to synchrotron or adiabatic losses (Fanti et al. 1987). Canosa et al. (1999) used the ROSAT HRI data to study the correlation between the radio and X-ray emission of a possible nuclear source, obtaining an upper limit for the nuclear X-ray flux which exceeds the expectation based on the radio data by more than two orders of magnitude.

In this work we use the data collected by the ROSAT HRI to study the structure of the NGC 507 hot halo. In particular we concentrate on the properties of the nuclear region, where the HRI resolution allows to resolve small scale structures. We then relate the results to those obtained by the ROSAT PSPC at larger scales.

4.2. OBSERVATIONS AND DATA ANALYSIS

4.2.1. The Data

The NGC 507 field, including NGC 499, was observed on January 1995 by the ROSAT HRI (David et al. 1996) for a total time of ~ 28 ks (Table 4.1). The data, consisting of 2 Observing Bin Intervals (OBI), were reduced with the SASS7_5 versions of the ROSAT standard analysis software (SASS). To correct for the errors in the aspect time behavior (Harris 1999), discussed in § 2.2.1, we run the ASPTIME routine (F. Primini 2000, private communication).

We further tried to correct for problems related to the spacecraft wobble (Harris et al. 1998, also see § 2.2.1); however the pointlike sources detected in our field (Table 4.3) are not bright enough to allow an accurate determination of the X-ray centroid (crucial for the correction), when divided in time bins. Since the global PRF is ~ 7" FWHM we decided to

Table 4.1: The ROSAT HRI observation of the NGC 507/NGC499 field.

name	NGC 507
Field center	
(R.A., Dec)	$01^h23^m39^s$ 33°15'36"
sequence id.	RH600680n00
Exp. time	28310 s
obs. date	1995 Jan 14
P.I.	D.-W. Kim
No. OBI	2
Distance [a]	65.8 Mpc
N_H [b]	5.3×10^{20} cm^{-2}

[a] Estimated assuming $H_0 = 75$ km s^{-1} Mpc^{-1} and a velocity of 4934 km s^{-1} (Huchra, Vogeley & Geller 1999)
[b] Galactic line-of-sight column density (Stark et al. 1992)

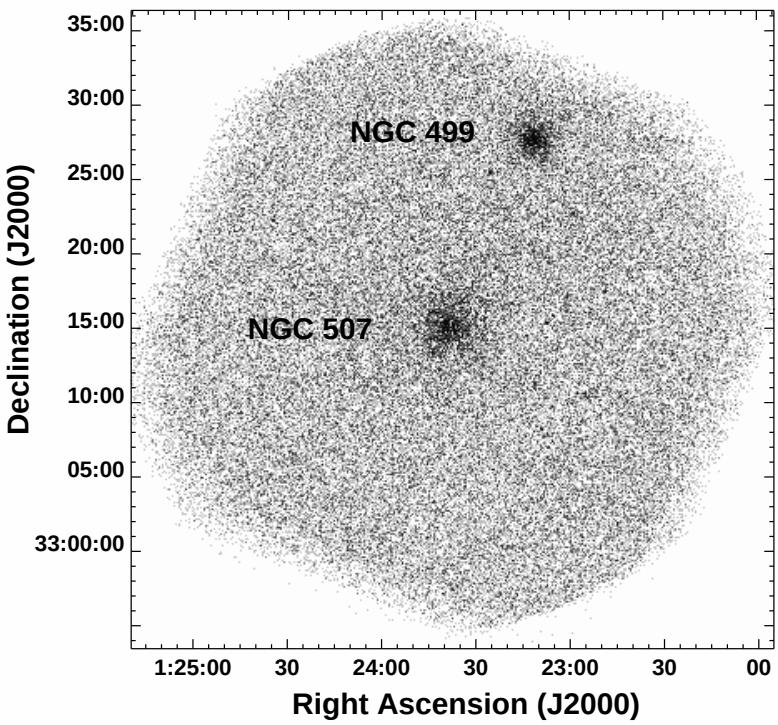

Fig. 4.1.— Raw HRI image of the NGC 507/NGC 499 field. The data are rebinned in 5×5 arcsec pixels. North is up and East is left.

use the uncorrected data. The HRI field of view (FOV) is shown in Figure 4.1.

We have run the software developed by Snowden et al. (1994, hereafter SMB), to produce an exposure map and a background map for our observation. We then corrected for exposure time and quantum efficiency variations across the detector by dividing the raw data by this exposure map.

4.2.2. Surface Brightness Distribution

To study the surface brightness distribution of NGC 507 the exposure corrected data were rebinned in 5×5 arcsec pixels and then convolved with a gaussian filter of $\sigma = 15$" (Figure 4.2). The resulting image shows the presence of an extended X-ray halo surrounding the galaxy. The central part of the halo (the one enclosed in the dashed box) is relatively symmetric but elongated in the NE-SW direction. Two filamentary structures seem to depart from the galactic center toward NW and SE respectively. The morphology of the outer halo is very irregular due to the low S/N ratio of the HRI image. However there appears to be more emission in the region enclosed within the two galaxies with respect to the other directions. The NGC 499 halo is less extended than the NGC 507 one and much more symmetric. The positions of the sources detected by the wavelets algorithm (Table 4.3) and discussed in § 4.2.7, are marked with crosses.

The large scale distribution of hot gas was already studied by Kim & Fabbiano (1995) with the ROSAT PSPC, which has a higher sensitivity than the HRI. We thus concentrate on the structure of the nuclear region (dashed box in Figure 4.2) which is better resolved by the HRI. The complex structure of this region is already suggested by the fact that the wavelets algorithm detects three distinct emission peaks (white crosses).

Examining this area in more detail (Figure 4.3a), a number of interesting features can be detected: 1) a strong emission peak can be observed in the center of the X-ray halo; this peak is slightly elongated in the NW-SE direction due to the presence of two 'tails': a main one extending in the NW direction and a fainter one visible on the SE side; 2) a secondary peak is visible ~ 50" West of the primary peak (source No.9); 3) a region of low X-ray brightness is interposed between the primary and secondary peak; 4) a third peak is visible ~ 40" East of the galaxy center (source No.5); 5) additional diffuse emission is present on the Southern side of the nucleus, making the surface brightness gradient flatter than on the Northern side.

The main peak is almost coincident with the center of the optical galaxy (Figure 4.3b). The second and third peak, instead, are not related to any optical feature, although being

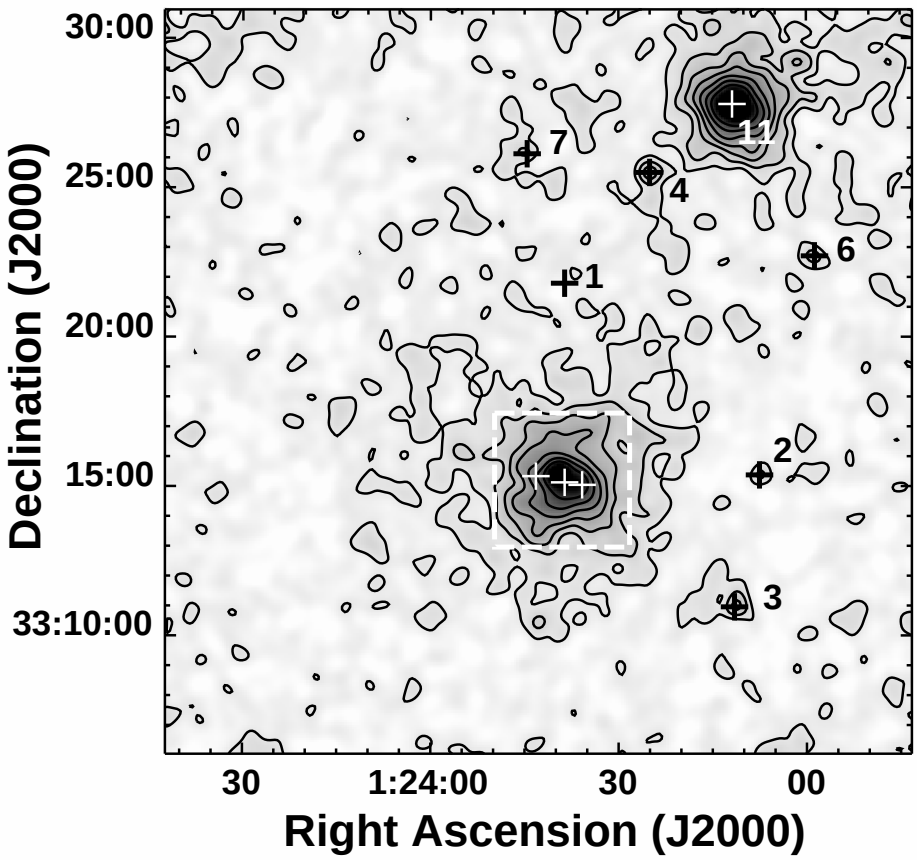

Fig. 4.2.— Exposure corrected image of the center of the HRI field. The data are rebinned in 5×5 arcsec pixels and smoothed with a gaussian filter of $\sigma = 15$". The X-ray contours are spaced by a factor of 1.2 with the lowest one at 6.4×10^{-3} cnts arcmin^{-2} s^{-1}. Crosses show the position of sources detected by the wavelets algorithm (Table 4.3). The white dashed box is the region enlarged in Figures 4.3, 4.5 and 4.6. In the figure North is up and East is left.

within the stellar body of the galaxy. There is also some faint emission coincident with the position of the elliptical galaxy NGC 508, located 1.5 arcmin North of NGC 507, which may indicate the presence of hot gas in the core of this system.

To reveal the presence of extended low S/N features we adaptively smoothed the HRI image with the *csmooth* algorithm contained in the CIAO CXC package (see § 2.2.3). In the resulting image (Figure 4.4), in addition to the three emission peaks mentioned before,

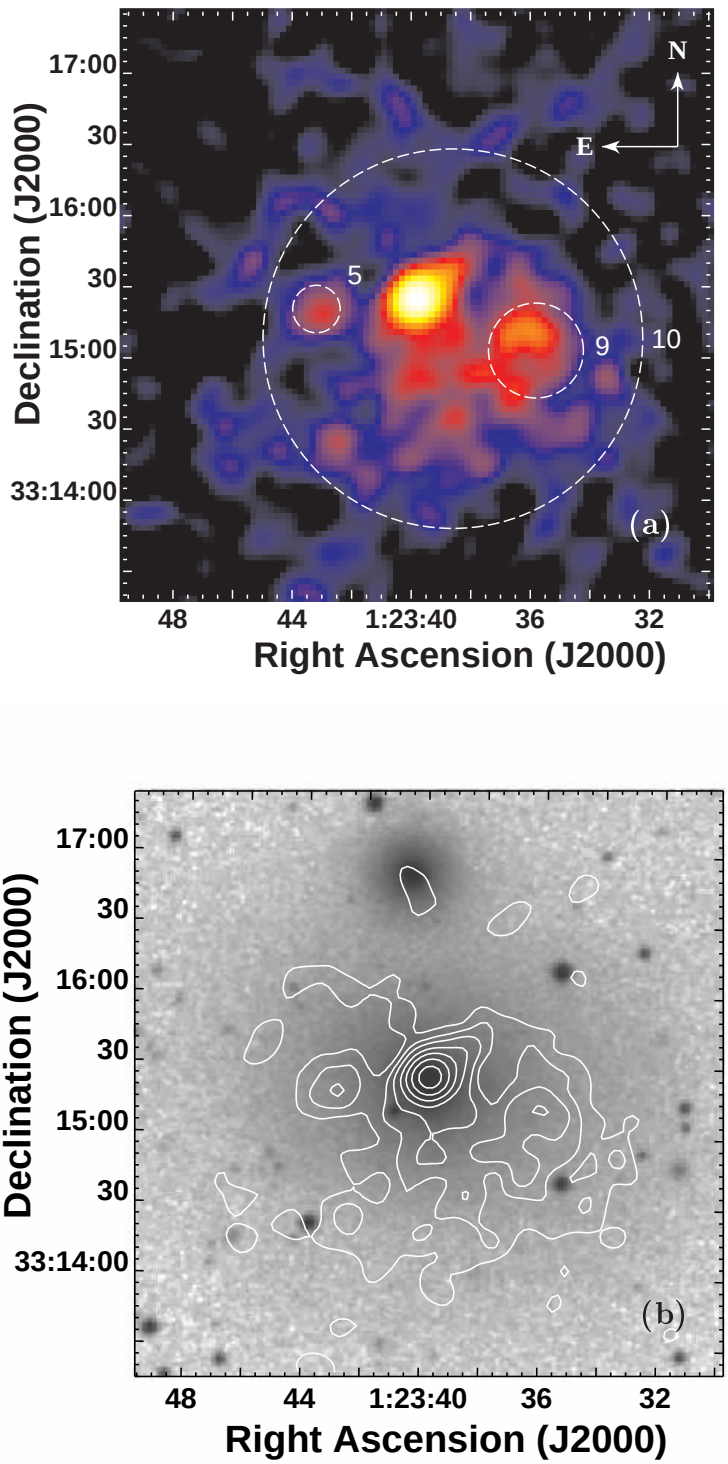

Fig. 4.3.— **(a)** 2.5×2.5 arcsec/pixel image of the nuclear region of NGC 507. The image is convolved with a gaussian filter of $\sigma = 5''$. Colors from black to white represent logarithmic X-ray intensities from 5.7×10^{-3} to 8.1×10^{-2} cnts arcmin^{-2} s^{-1}. The dashed circles show the region of maximum S/N ratio for the sources detected by the wavelets algorithm. **(b)** X-ray brightness contours overlaid on the 1 arcsec/pixel Digital Sky Survey (DSS) image (logarithmic grayscale). Contours are spaced by a factor 1.3 with the lowest one at 1.4×10^{-2} cnts arcmin^{-2} s^{-1}. In the figures North is up and East is left.

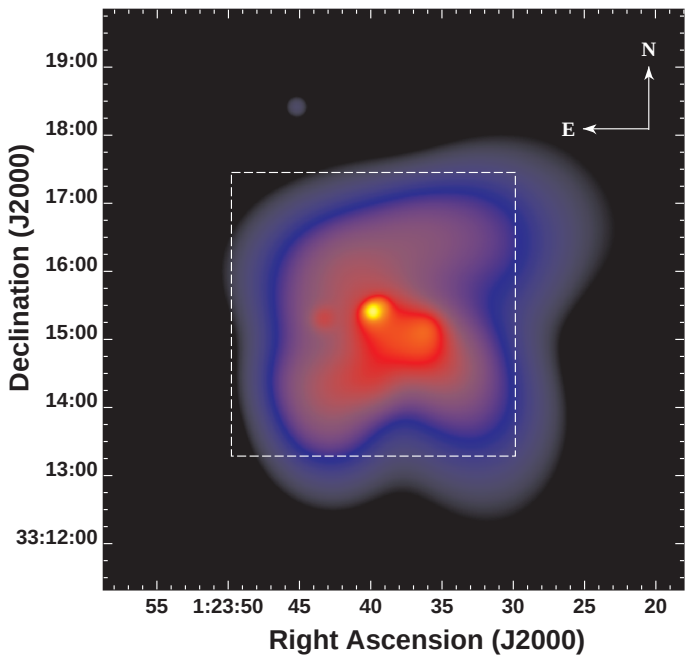

Fig. 4.4.— Adaptively smoothed image of the center of the NGC 507 halo. The data are rebinned in 1×1 arcsec pixels. Colors from black to yellow represent logarithmic X-ray intensities from 6.3×10^{-3} to 1.5×10^{-1} cnts arcmin^{-2} s^{-1}. The dashed box is the region enlarged in Figures 4.3, 4.5 and 4.6.

we can distinguish an elongated tail extending on the North and bending Westwards out to $\sim$ 200" (63 kpc [2]), and an X-ray tongue protruding by $\sim$ 160" (51 kpc) on the South-East side. These two features correspond to the filamentary structures visible also in Figure 4.2.

4.2.3. X-ray/Radio Comparison

NGC 507 is known to be a weak radio source. In Figure 4.5a,b we superimpose the radio contours at 20 cm (Parma et al. 1986; de Ruiter et al. 1986) on the smoothed X-ray image.

The nuclear radio source, visible in the high resolution map (Figure 4.5b) is coincident with the position of the central X-ray peak. However it seems to be slightly displaced ($\sim$ 4") toward the South-East edge of the peak. The radio jets/lobes appear aligned with

[2]At the the assumed distance of NGC 507, 1'=19.1 kpc

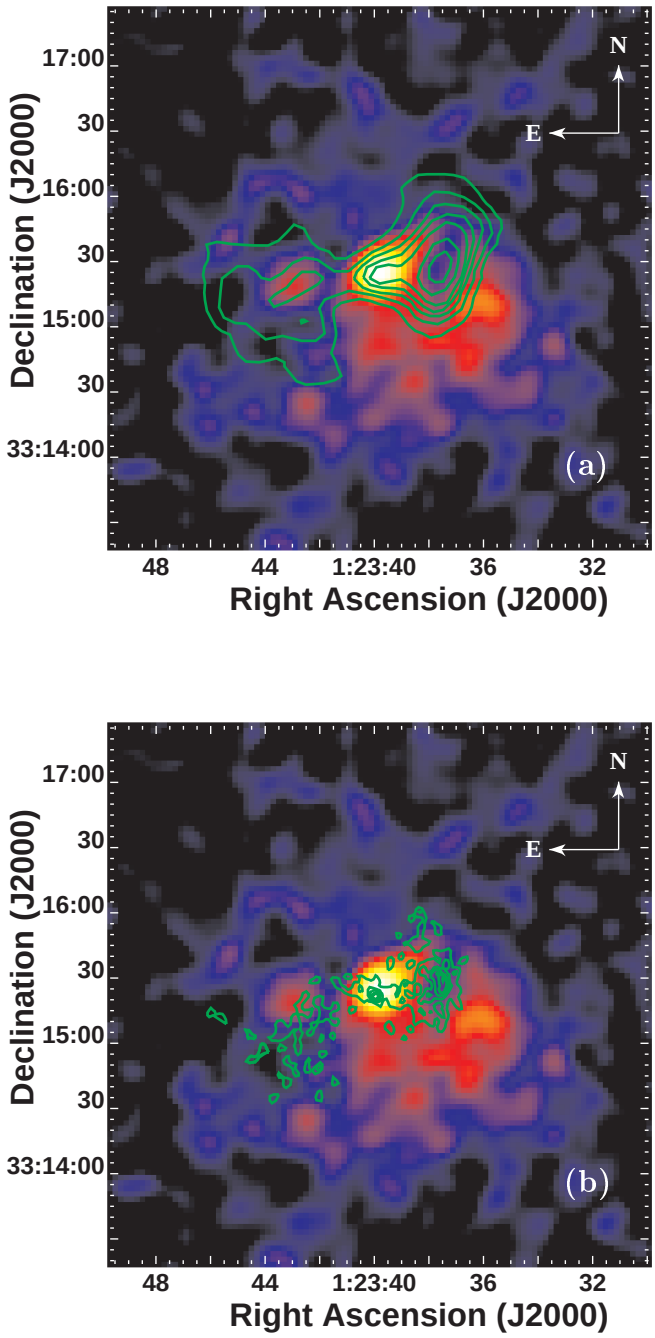

Fig. 4.5.— **(a)** 13" FWHM radio contours superimposed on the X-ray nuclear region of NGC 507. The X-ray image is the same shown in Figure 4.3a. **(b)** Higher resolution (3.5" FWHM) radio contours superimposed on the X-ray nuclear region of NGC 507.

the direction of the secondary X-ray peaks. The western jet appears to be collimated up to 10-15 arcseconds ($\sim$ 4 kpc) and then expands in a large lobe. The latter is coincident with the region of low surface brightness described in § 4.2.2. The higher resolution radio contours (Figure 4.5b) reveal a very good agreement between the morphology of the Western lobe and the shape of the 'cavity'. The secondary X-ray peak lies at the end of the radio lobe.

The correlation between the X-ray and radio surface brightness are less evident for the Eastern lobe. In fact this lobe is fainter than the Western one (27 mJy compared to 40 mJy at 1.4 GHz; de Ruiter et al. 1986). From the low resolution radio contours it seems that the compact X-ray peak falls in the center of the radio lobe; however, when we look at the high resolution map, the radio emission seems displaced South of the X-ray peak and falls in a region of low X-ray emission.

4.2.4. Bidimensional Halo Model

To study the complex structure of the inner halo of NGC 507 we built a bidimensional model using the *Sherpa* fitting software contained in the CIAO CXC package. The model was composed by adding together two bidimensional Beta components (equation 2.1), representing respectively the central X-ray peak and the larger galactic halo. The 2D model was convolved for the HRI PRF and then fitted on the exposure corrected HRI image following the method outlined in § 2.2.5: we fitted the large galactic component on a 30×30 arcsec pixel image and the central component on a higher resolution 5×5 arcsec pixel image.

Table 4.2 shows the best-fit parameters of the bidimensional model. During the fit the ellipticity ϵ and the position angle (P.A.) θ of the two components was fixed to 0. In fact the poor S/N ratio of the HRI image at large radii makes the ellipticity and P.A. of the galactic component difficult to determine and, anyway, of poor physical meaning. For what concerns the central component leaving ϵ and θ free to vary yields $\epsilon = 0.56 \pm 0.02$, $\theta = 137°$, and results in minor changes on the slope ($\beta = 0.63 \pm 0.01$) and the core radius ($r_0 = 0.32 \pm 0.02$). The central component is thus elongated in the NW-SE direction, as expected from the presence of the nuclear 'tails' (§ 4.2.2). The galactic component centroid is displaced by $\sim$ 22" (7 kpc) South-West of the central emission peak (Figure 4.6); this is in agreement with the position of source No.10 detected by the wavelets algorithm (Figure 4.3a) which corresponds with the galactic halo centroid. The best-values r_0 and β of the galactic component are consistent within 1 σ with those found by Kim & Fabbiano (1995); however our core radius is slightly larger due to the fact that we have separated the contribution of the central peak from the larger galactic halo.

Table 4.2: Best-fit parameters for the bidimensional halo model.

Component	Center Position		r_0	β	ϵ	θ	χ^2_ν	ν
	R.A.	Dec	(arcsec)		$(1 - \frac{minor\ axis}{major\ axis})$	(rad)		(d.o.f.)
Central	$01^h23^m39.8^s$	33°15'26"	0.22±0.02	0.58±0.01	$0.0^{(a)}$	$0.0^{(a)}$	0.5	73
Galactic	$01^h23^m38.7^s$	33°15'07"	49± 9	0.48±0.04	$0.0^{(a)}$	$0.0^{(a)}$	0.9	776

[a] The parameters ϵ and θ have no error because they were held fixed during the fit (see discussion in text).
Note - uncertainties are 1σ confidence level for 5 interesting parameters

4.2.5. Radial Brightness Profiles

To study quantitatively the hot halo of NGC 507 we derived radial profiles of the X-ray surface brightness. We binned the X-ray counts in 2 arcsec annuli, centered on the main X-ray peak, up to 20 arcsec and in 10 arcsec annuli at larger radii. This allows to both exploit the HRI resolution in the inner regions, where the X-ray emission is stronger, and to have a good S/N ratio in the outer regions. The derived profile is shown in Figure 4.7 as a thin continuous line.

To derive the instrumental background level we used the background map produced by the SMB software (dot-dashed line in Figure 4.7). However, as discussed in § 2.2.4, the latter may be a poor representation of the actual background when an extended source is present in the field. We followed the same approach used for NGC 1399, comparing the HRI data with the PSPC profile obtained by Kim & Fabbiano (1995). The HRI profile was rebinned in 30 arcsec annuli to match the PSPC resolution and the SMB background was then rescaled to obtain the best agreement between the two profiles in the 100-500 arcsec range. The final adopted background (dashed line) is in close agreement with the flattening level of the HRI profile, i.e. the brightness level measured at radii > 500 arcsec. This result was expected since, differently from the case of NGC 1399, the shorter exposure time resulted in a lower S/N ratio in the outer HRI field. Thus the measured background is dominated by the instrumental contribution expected when no source is present. Using this background determination we derived the background-subtracted profile shown as filled circles.

The inner 10 arcsec are dominated by the emission due to the central X-ray peak showed in Figure 4.3a. A comparison with the HRI PRF suggests that the peak is extended. However, taking into account the PRF uncertainties due to residual aspect problems (shaded region in the Figure; David et al. 1996) and the asymmetries discussed below, we find that

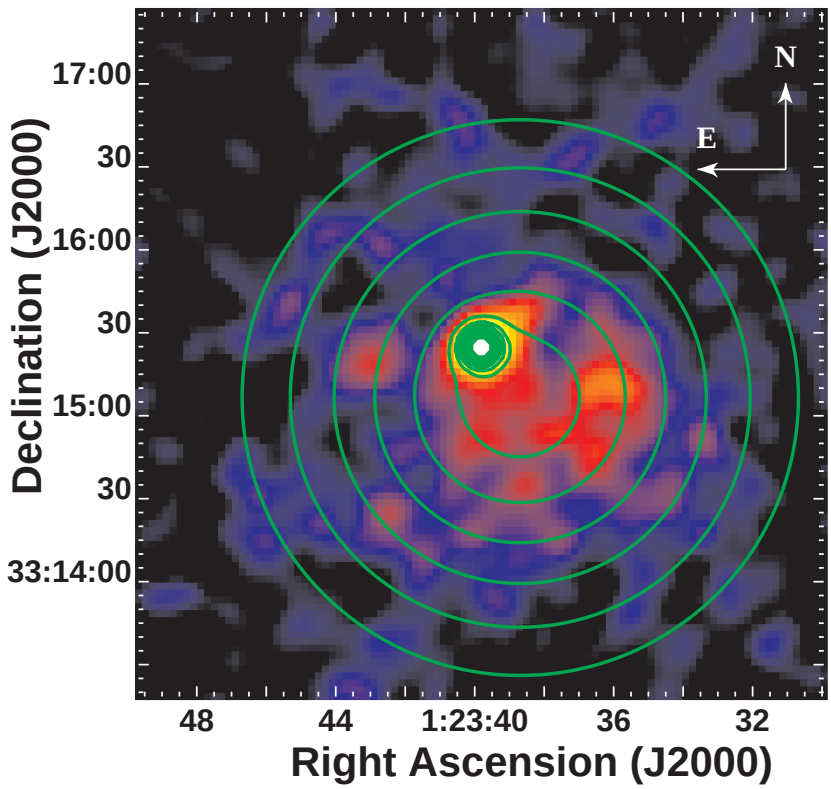

Fig. 4.6.— X-ray contours of the bidimensional model superimposed on the NGC 507 central halo. The model contours are spaced by a factor 1.3 with the lowest one at 9.6×10^{-3} cnts arcmin^{-2} s^{-1}.

the central peak is marginally consistent with the presence of a pointlike nuclear source. Past 20 arcsec ($\sim$ 6 kpc) the X-ray profile flattens due to the presence of the galactic halo component, and then decreases with a power-law profile for $r > 60$".

Figure 4.8 shows the model profile (§ 4.2.4) – convolved with the HRI PRF – superimposed on the HRI data. The contribution of the two components are shown by the dashed and the dot-dashed line for the central and galactic component respectively. The PSPC profile measured by Kim & Fabbiano (1995) is in very good agreement with the HRI data and shows that the halo brightness decreases as a $r^{-1.88}$ power-law even outside the range covered by the HRI points. For comparison we also show the optical V band surface brightness profile measured by González-Serrano & Carballo (2000).

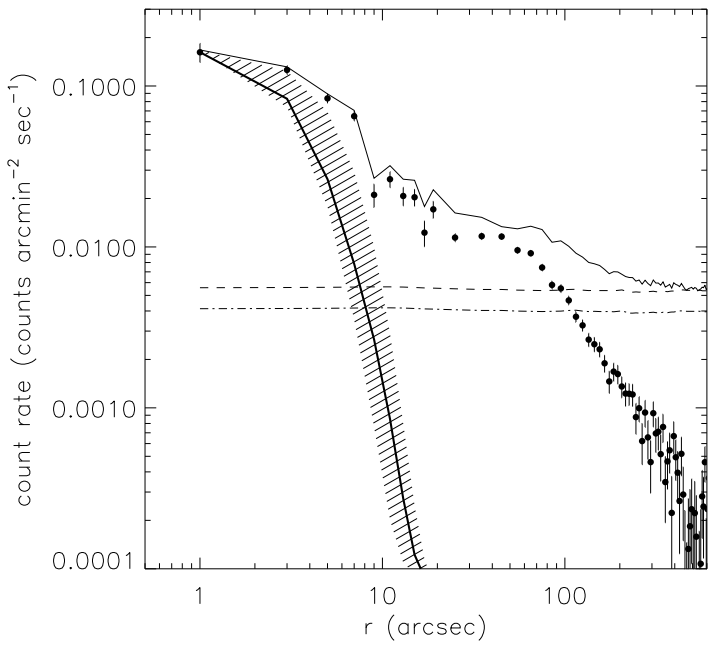

Fig. 4.7.— HRI surface brightness profile of NGC 507 (thin continuous line). The dashed (dot-dashed) line represent the SMB background map profile after (before) rescaling to match PSPC counts. Filled circles show the background subtracted profile obtained using the rescaled SMB background. The PRF profile and the uncertainties due to residual aspect errors, are shown respectively as the thick continuous line and the shaded region.

From Figure 4.8 we can see that in two regions, for 10" $< r <$ 20" and 40" $< r <$ 100", the HRI counts are in excess with respect to those predicted by the bidimensional model. To investigate these features we derived radial profiles excluding some of the structures described in § 4.2.2. Figure 4.9 shows that excluding sources No.5 and 9 (Table 4.3), corresponding to the secondary emission peaks shown in Figure 4.3a, significantly reduces the counts measured in the range 30" $< r <$ 70".

To study the excess in the range 10" $< r <$ 20" we derived a radial brightness profile adding together the counts extracted in two sectors (100° <P.A.< 160° and 280° <P.A.< 340°; '**Tail**' in Figure 4.10a) aligned with the tails extending on the NW and SE side of the central X-ray peak (§ 4.2.2). In Figure 4.10b, this profile is compared with the one obtained in the NE sector (340° <P.A.< 100°; '**No tail**' in Figure 4.10a) where the central component gradient is steeper. The profile in the region excluding the nuclear tails shows a better agreement with the bidimensional model out to 15"; at larger radii it falls below the model because it is missing much of the contribution of the galactic component, which

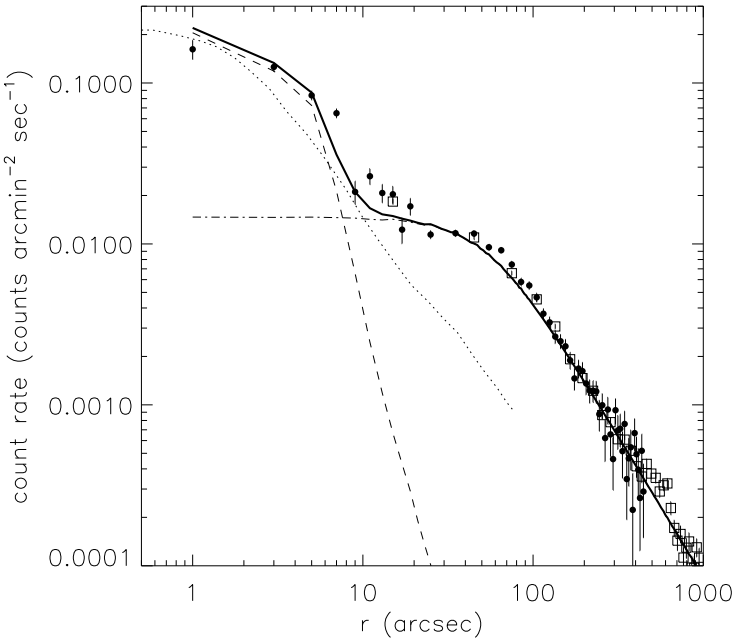

Fig. 4.8.— Radial profile of the bidimensional HRI model (continuous line). The central and galactic components are represented respectively by the dashed and dot-dashed lines. HRI (PSPC) counts are shown as filled circles (empty squares). The dotted line shows the V band surface brightness profile measured by González-Serrano & Carballo (2000).

is centered SW of the main peak (Figure 4.6).

Since most of the morphological structures seen in the central halo of NGC 507 may be due to the presence of the radio-emitting plasma, we also derived radial profiles in sectors occupied or avoided by the radio lobes (Figure 4.11a). The results are shown in Figure 4.11b. The profile avoiding the radio lobe regions shows a better agreement with the bidimensional model through all the range covered by the HRI data; conversely the profile extracted from regions occupied by the lobes shows significant deviations from the bidimensional model.

We can summarize the results of this section as follows: the bidimensional model is a reasonable representation of the X-ray brightness distribution. The main deviations from the model are associated to regions where the hot gas is presumably interacting with the radio emitting plasma; when such regions are ignored the radial profiles show a good agreement with the model profile.

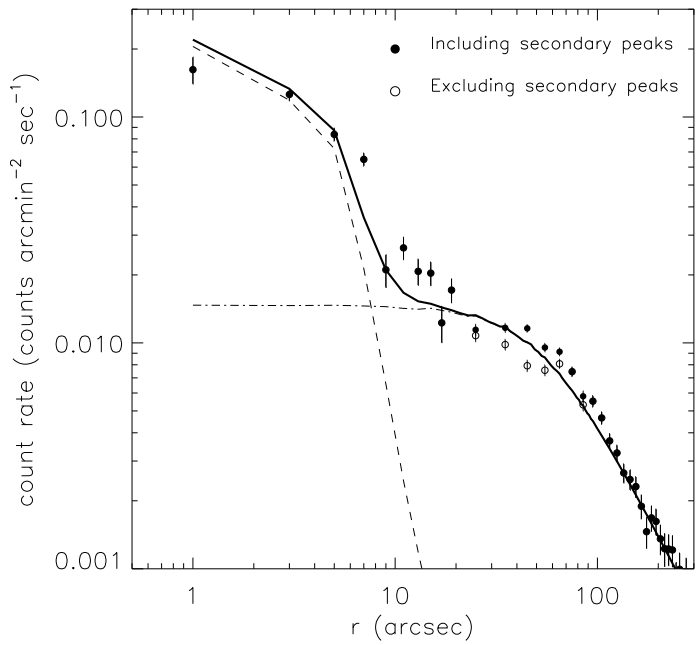

Fig. 4.9.— HRI radial profiles of the NGC 507 nuclear region including (filled circles) and excluding (empty circles) the secondary emission peaks corresponding to sources No.5 and 9 (Figure 4.3a). The meaning of the lines is the same as in Figure 4.8.

4.2.6. Density, Cooling Time and Mass Profiles

To derive the density profile of the X-ray emitting gas we followed the method discussed in § 1.4.2 and applied to NGC 1399 and NGC 1404 in § 2.2.6 and 3.2.3 respectively: we deprojected the measured emission in concentric shells assuming an isothermal temperature profile with $kT = 1.1$ keV and the cooling function given by Sarazin & White (1987). As discussed in § 4.2.5, the bidimensional model provides a good representation of the overall X-ray emission; it also models the X-ray profile excluding the contribution of regions where the interaction with the radio-emitting plasma causes strong fluctuations in the surface brightness. For such reason we use the model profile shown in Figure 4.8 to derive the underlying gas density. Since the temperature profile measured by Kim & Fabbiano (1995) shows the presence of a central temperature drop, we also used a lower temperature for the central component, obtaining an almost identical result. The deprojected density is shown in Figure 4.12. The dashed and dot-dashed lines represent the contribution of the galactic and central component respectively.

Using this density profile we calculated the cooling time (equation 1.37) of the NGC 507

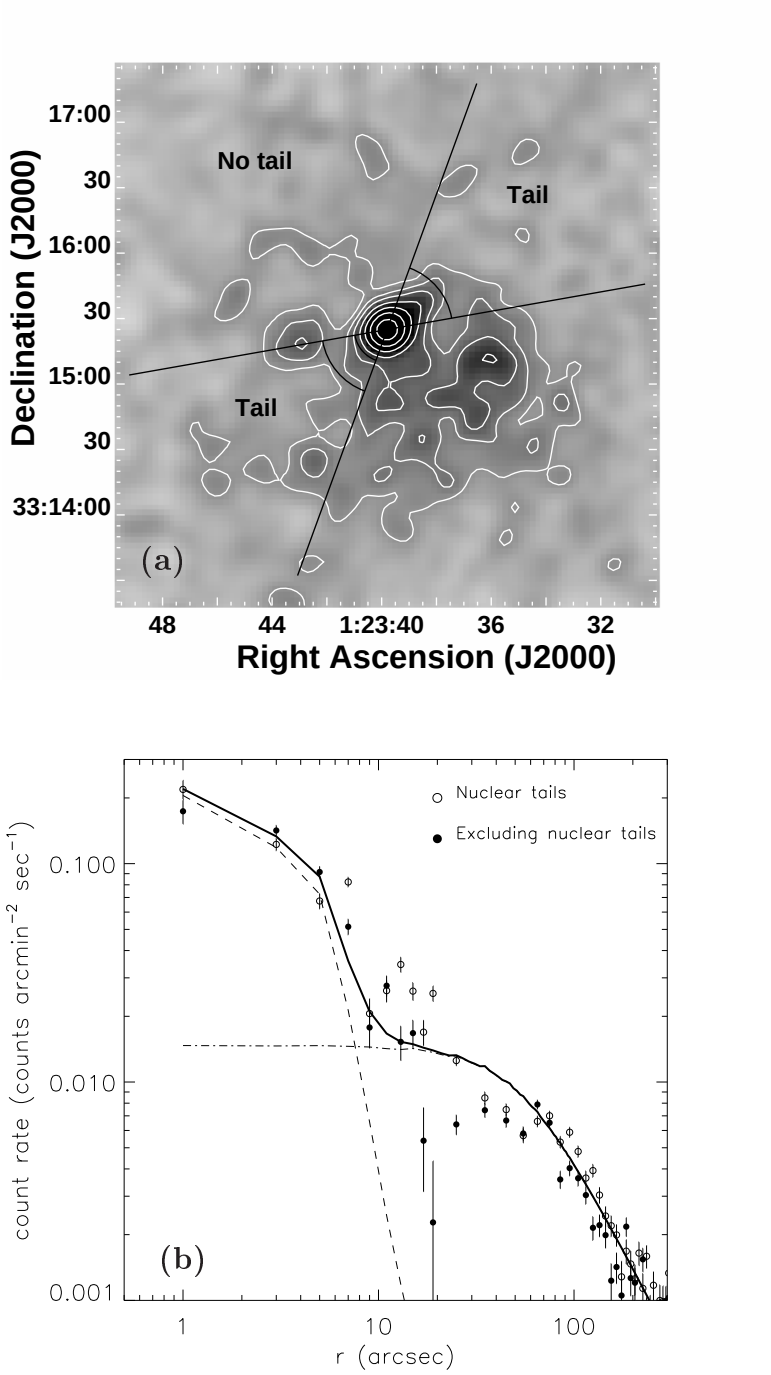

Fig. 4.10.— **(a)** X-ray surface brightness image of NGC 507 showing the NW and SE sectors used to extract the nuclear tail profiles and the NE sector excluding the nuclear tail contribution. **(b)** HRI radial profiles of the NGC 507 central region including (empty circles) and excluding (filled circles) the contribution of the nuclear tails. Both profiles are extracted excluding the secondary peaks (sources No.5 and 9 in Table 4.3). The meaning of the lines is the same as in Figure 4.8.

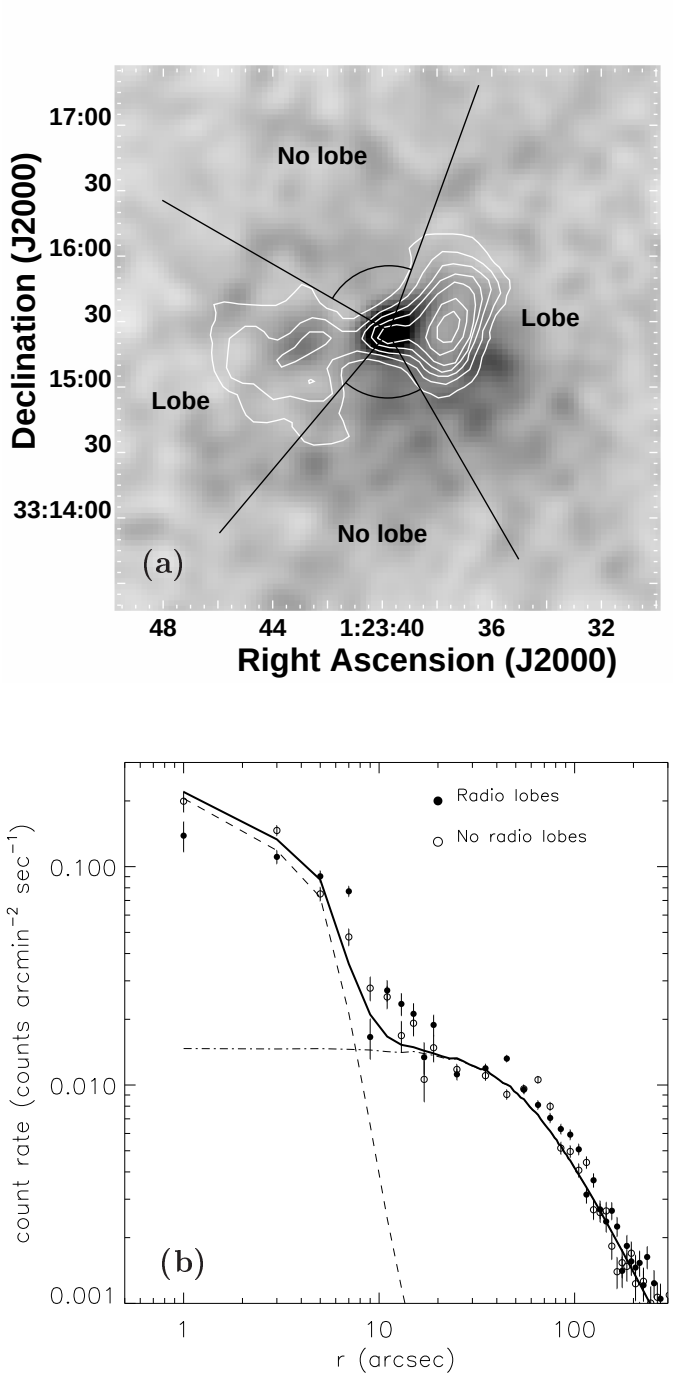

Fig. 4.11.— **(a)** X-ray surface brightness image of NGC 507 showing the East and West (North and South) sectors used to extract the X-ray profiles in the regions occupied (avoided) by the radio lobes. **(b)** HRI radial profiles of the NGC 507 central regions occupied (filled circles) and avoided (empty circles) by the radio lobes. The meaning of the lines is the same as in Figure 4.8.

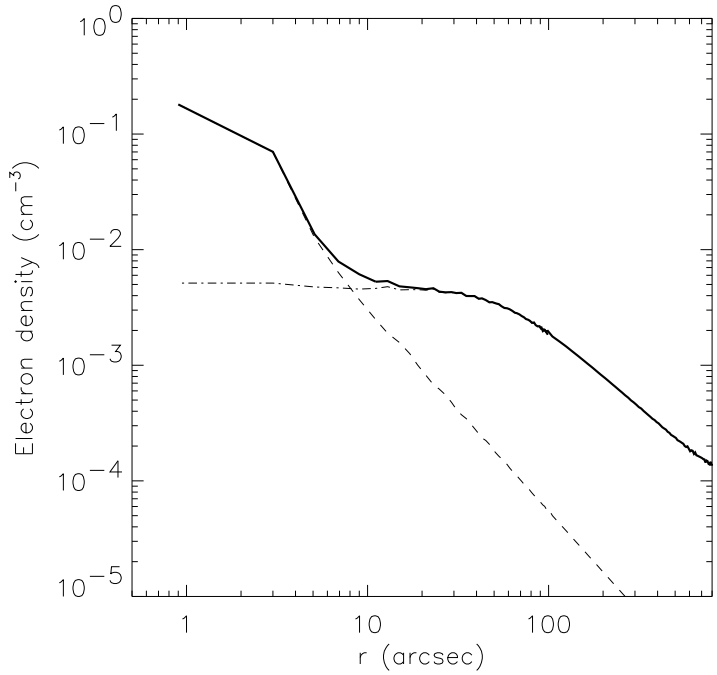

Fig. 4.12.— Deprojected density profile of the NGC 507 gaseous halo (continuous line). The dashed and dot-dashed lines show, respectively, the contribution of the central and galactic component.

halo shown in Figure 4.13. Our result is in good agreement with the Kim & Fabbiano (1995) estimate at large galactocentric distances ($r > 60$") with minor differences due to their use of a non-isothermal temperature profile. At smaller radii our HRI data are able to sample the characteristics of the central component, whose cooling time is more than one order of magnitude smaller than those of the galactic component. Both components, however, have cooling times smaller than the Hubble time (10^{10} yr) within the cooling radius $\simeq 250$" (80 kpc).

Figure 4.14 shows both the integrated gaseous mass and the integrated total mass as a function of radius. The gaseous mass, calculated from the gas density profile assuming cosmic abundances (see § 2.2.6), yields $\simeq 10^{12}$ $M_\odot$ within 1000" (320 kpc). The contribution of the central component, which dominates the inner 15" (5 kpc), is estimated to be $\sim 10^{10}$ $M_\odot$ at $r = 1000$", representing $\sim 1\%$ of the total gaseous mass.

The total mass profile was calculated using equation (1.35). We assumed three different temperature profiles: an isothermal profile at 1.1 keV, a linear fit $kT = -2.3 \times 10^{-4}\, r + 1.21$ keV (r is expressed in arcsec) to account for the temperature decline after $\sim$ 150", and

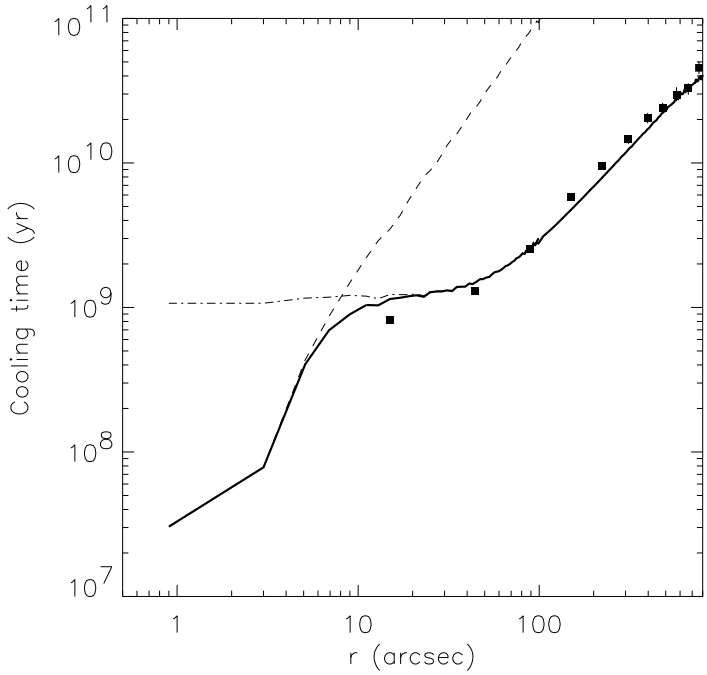

Fig. 4.13.— Cooling time profiles of NGC 507. The lines have the same meaning as in Figure 4.12. The cooling times derived by Kim & Fabbiano (1995) are shown as filled squares.

a power law $kT = 0.04\ r^{0.5} + 0.7$ keV to fit the central temperature drop. Figure 4.14b shows that the total mass profiles are weakly dependent on the assumed temperature profile, except in the inner 100" (32 kpc) where the central mass obtained accounting for the low central temperature is $\sim 50\%$ smaller. The shaded region represents the total stellar mass calculated from the surface brightness profile measured by González-Serrano & Carballo (2000) and assuming a M/L ratio ranging from 6 to 8 $M_\odot/L_\odot$.

For $r > 50$" our mass profile is in good agreement with Kim & Fabbiano (1995) and suggests the presence of dark matter, since it exceeds the stellar mass estimate extrapolated from the optical profile measured by González-Serrano & Carballo (2000). For r< 50" the X-ray mass estimate yields an unphysical result: in fact it falls below the stellar mass and its gradient is < 0 for 10" $< r <$ 50", which is impossible for an integrated profile. The difficulties involved in deriving accurate mass profiles in the halo core, from X-ray measurements, have been already noticed in previous works and can be explained by the presence of non-gravitational effects[3] (see for instance Brighenti & Mathews 1997). In our

[3]Within a few arcsec from the main emission peak we must also consider the influence of the PRF. Even

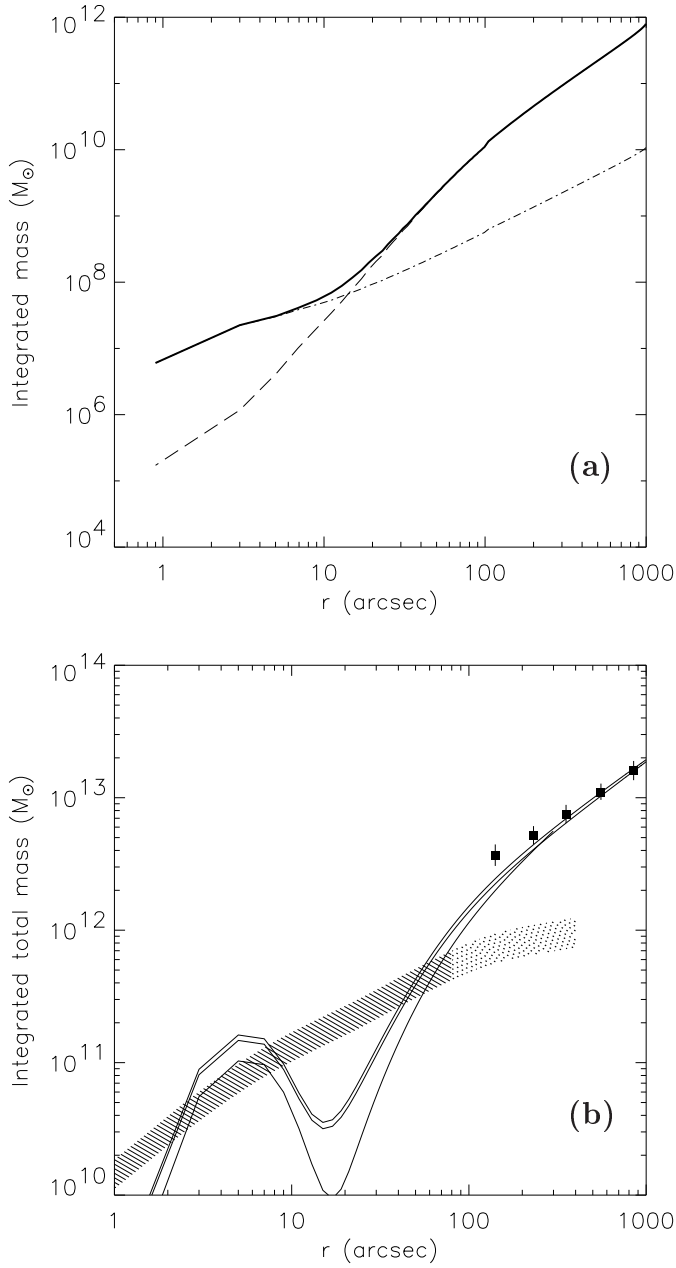

Fig. 4.14.— **(a)** Integrated gaseous mass within r. The meaning of the lines is the same as in Figure 4.12. **(b)** Integrated total mass within r. The continuous lines represent the gravitating mass estimates obtained assuming the different temperature profiles described in the text. The total mass estimate of Kim & Fabbiano (1995) is shown as filled squares. The shaded (dotted) region shows the stellar mass contribution estimated (extrapolated) from the optical profile measured by González-Serrano & Carballo (2000), assuming a M/L ratio ranging from 6 to 8 $M_\odot/L_\odot$. Notice the unphysical behavior of the total mass profile for $r < 50$", which is discussed in the text.

case we have seen how the presence of the nuclear radio source strongly perturbs the central halo morphology (§ 4.2.3). This is reflected in the gas density profile and thus on the total mass determination. Although we derived the total mass profile through the bidimensional model, which is less affected by X-ray/Radio interactions (see § 4.2.5), the reconstruction of the unperturbed gas distribution is a difficult task. However we notice that for 2" $< r <$ 10", i.e. where the central component emission dominates, the total mass profile does not greatly exceed the stellar mass, suggesting that the galactic center is dominated by luminous matter. This result is in agreement with those found in other galaxies (e.g. Brighenti & Mathews 1997) and will be discussed in detail in § 5.2.

4.2.7. Discrete Sources

To study the population of discrete sources in the HRI field we used the wavelets algorithm developed by Damiani et al. (1997a,b) and already described in § 2.2.9. Using a S/N threshold of 4.2[4] (corresponding to a contamination of 1 spurious source per field) the algorithm detected 11 sources shown in Figure 4.15. The properties of these sources, as measured by the wavelets algorithm, are reported in Table 4.3. Sources No.10 and 11 are missing from the table since they are NGC 507 and NGC 499. We also notice that sources No.5 and 9 correspond to the secondary central peaks discussed in § 4.2.2.

To derive the X-ray fluxes we used the PIMMS software to calculate a conversion factor between the HRI count rate and the incident flux. We assumed the same spectral models discussed in § 2.2.9: a power law with photon index 1.96 ± 0.11 ($f^b_{HRI} pow.law$ in Table 4.3) following the results of Hasinger et al. (1993) for faint sources, and a thermal spectrum with $kT = 0.52$ and abundance $Z \sim 0.2\ Z_\odot$ (f^{RS}_{HRI} in Table 4.3) as found by Kim & Fabbiano (1995). Assuming a galactic absorption of 5.3×10^{20} cm^{-2} we obtain a conversion factor of 1 cps=6.925×10^{-11} ergs s^{-1} and 1 cps=4.076×10^{-11} ergs s^{-1} respectively in the 0.1-2.4 keV energy range. We notice that the energy range is different from the 0.5-2.0 keV used in § 2.2.9 since here we are mainly interested in comparing our results with those of Kim & Fabbiano (1995). Restricting our energy band to the 0.5-2.0 keV interval, as we have done in § 2.2.9, results in a reduction of the X-ray fluxes of $\sim 55\%$ for the power law model and of $\sim 34\%$ for the thermal model.

In Table 4.4 we cross-correlate the sources detected in the HRI field with those found by

---

if the bidimensional model accounts for instrumental effects, an accurate deconvolution is very difficult.

[4]This value differs from the one used in § 2.2.9 for NGC 1399, since it depends on the S/N ratio of the data and thus on the exposure time.

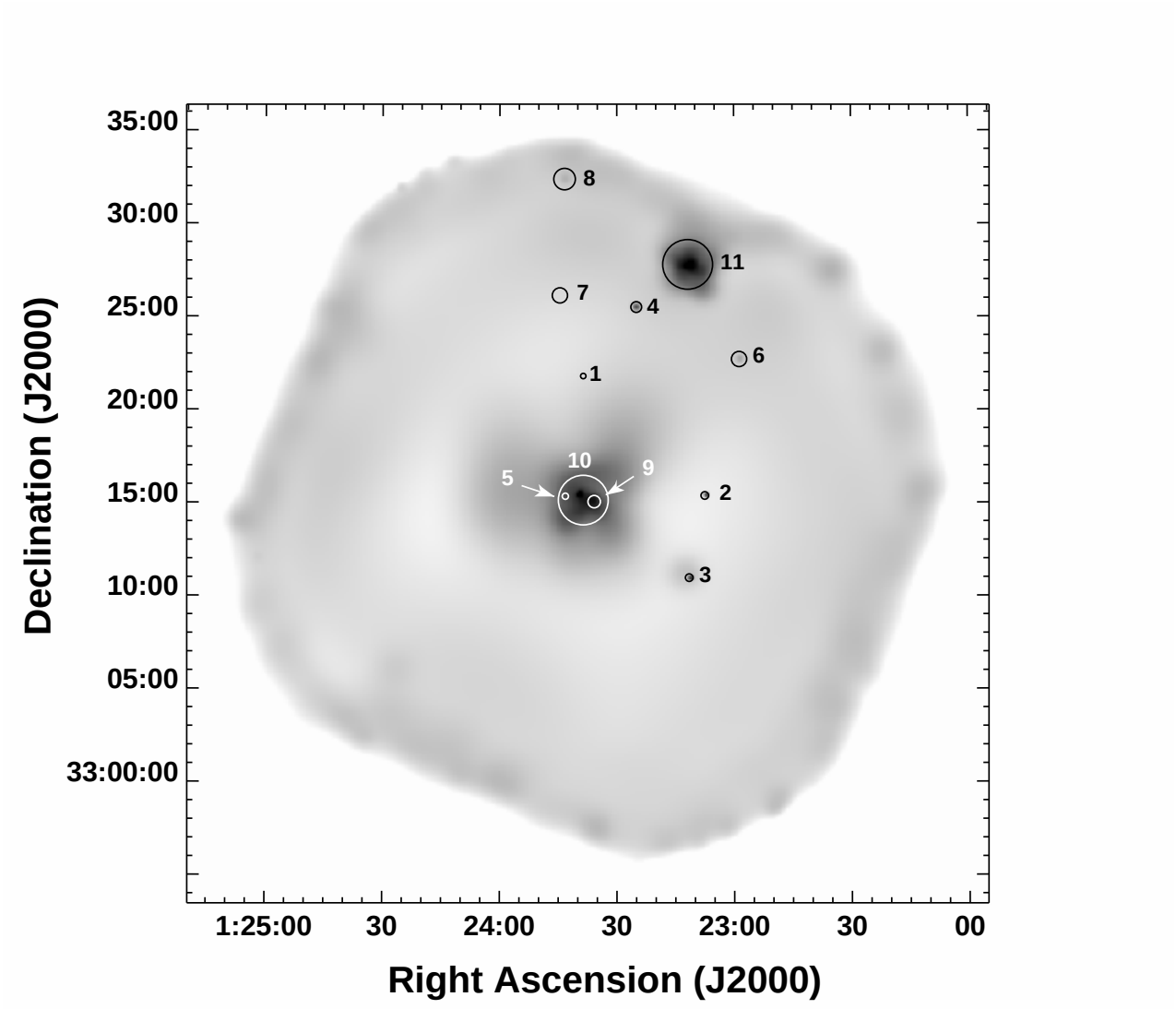

Fig. 4.15.— Discrete sources detected by the wavelets algorithm superimposed on the adaptively smoothed HRI field. The circles show the region of maximum S/N ratio for each source. The position of sources No.5 and 9 is shown in greater detail in Figure 4.3a.

Table 4.3: Discrete Sources - Results of the Wavelets algorithm

Source No.	R.A. (J2000)	Dec. (J2000)	3σ Radius (arcsec)	Counts	Max S/N	Count Rate (10^{-4} Cnts sec^{-1})	$f_{HRI}^{pow.law\,(a)}$	$f_{HRI}^{RS\,(a)}$
1	1:23:38.6	+33:21:48	8.7	13±6	4.3	5±2	35±14	20±8
2	1:23:07.5	+33:15:23	12.2	31±9	7.0	11±3	76±21	45±12
3	1:23:11.5	+33:10:58	12.2	37±10	8.0	13±4	90±28	53±16
4	1:23:25.0	+33:25:31	17.3	47±13	7.6	17±4	118±28	69±16
5	1:23:43.2	+33:15:21	17.3	33±11	4.8	12±4	83±28	49±16
6	1:22:58.7	+33:22:43	24.5	39±12	5.2	14±4	97±28	57±16
7	1:23:44.6	+33:26:08	24.5	33±11	4.6	13±4	90±28	49±16
8	1:23:43.4	+33:32:23	34.6	46±14	4.9	21±6	145±42	65±20
9	1:23:35.8	+33:15:03	34.6	104±28	6.1	37±10	256±69	151±41

[a] Flux in the 0.1-2.4 KeV band in units of 10^{-15} erg s^{-1} cm^{-2}.

Kim & Fabbiano (1995). The fluxes that they derive from PSPC data are reported in column f_{PSPC}^{RS}. We searched for long-term variability of the matching sources comparing these fluxes with those measured by the wavelets algorithm (Table 4.3). We mark as variable those sources whose flux varied by more than 3σ between the PSPC and HRI observations, i.e. between 1993 and 1995. We found that only source No.3 show significant variability in this interval. To check if the different procedures, extraction radii and background subtraction, significantly affect the PSPC count rate determination, we extracted from the GALPIPE database (see § 2.2.5) the count rates measured by the wavelets algorithm on the second of the PSPC observations (RP600254a01) used by Kim & Fabbiano (1995). The results are in good agreement with the Kim & Fabbiano (1995) determinations, except for source No.4. In this case however the proximity to the NGC 499 halo and the large PSPC PRF may compromise the wavelets accuracy. We must notice that sources No.5 and 9, which are likely to be produced by the interaction of the radio lobes with the surrounding ISM (see § 4.3.2), have no PSPC counterpart since they are undetected due to the lower spatial resolution of this instrument.

The optical DSS image of the NGC 507/499 region was visually inspected to find optical counterparts of the X-ray sources within a 2σ radius (Table 4.3) from the X-ray centroid. In this case we choose a smaller size (2σ) than the one adopted for NGC 1399 since the optical image of the NGC 507 region is more crowded. The results are summarized in column "Opt.id." of Table 4.4. We also cross-correlated our source list with the catalogs contained in the NED database. We found that source No.7 corresponds to the radio source NVSS J012345+332554 (Figure 4.16).

Table 4.4: Discrete Sources - Comparison with PSPC results and catalogues

Source No.	PSPC[a] No.	f_{PSPC}^{RS} [a,b]	f_{HRI}^{RS} [b]	Time Var. long-term[c]	Opt.id.	NED obj.
1	-	-	20±8	-	n	-
2	8	21 ± 10	45±12	n	y	-
3	10	171 ± 20	53±16	y	y	-
4	12	91 ± 12	69±16	n	y	-
5	-	-	49±16	-	n	-
6	7	81 ± 12	57±16	n	y	-
7	13	43 ± 10	49±16	n	y	NVSS J012345+332554
8	-	-	65±20	-	n	-
9	-	-	151±41	-	n	-

[a] As reported in Table 2 of Kim & Fabbiano (1995)

[b] Flux in the 0.1-2.4 KeV band in units of 10^{-15} erg s^{-1} cm^{-2}.

[c] Difference between PSPC and HRI fluxes: 'y' means variable source ($> 3\sigma$), 'n' means no variability detected.

Table 4.5: PSPC-HRI Sources Comparison - Upper limits from HRI data

PSPC[a] No.	f_{PSPC}^{RS} [a,b]	f_{HRI}^{RS}	f_{HRI}^{RS} 3σ upper limit	Time Var. long-term[c]
3	79 ± 15	14 ± 25	90	-
4	36 ± 10	21 ± 24	93	-
5	61 ± 14	40 ± 24	111	-
6	300 ± 27	116 ± 42	243	y
9	45 ± 11	8 ± 23	77	-
11	42 ± 11	14 ± 24	86	-
14	38 ± 10	32 ± 25	108	-
15	32 ± 10	9 ± 21	72	-
16	28 ± 10	9 ± 22	75	-
17	51 ± 11	11 ± 22	78	-
18	46 ± 13	67 ± 23	135	-
20	60 ± 14	19 ± 21	83	-

[a] As reported in Table 2 of Kim & Fabbiano (1995)

[b] Flux in the 0.1-2.4 KeV band in units of 10^{-15} erg s^{-1} cm^{-2}.

[c] Difference between PSPC flux and HRI upper limit: 'y' means variable source ($> 3\sigma$), '-' means no variability detected.

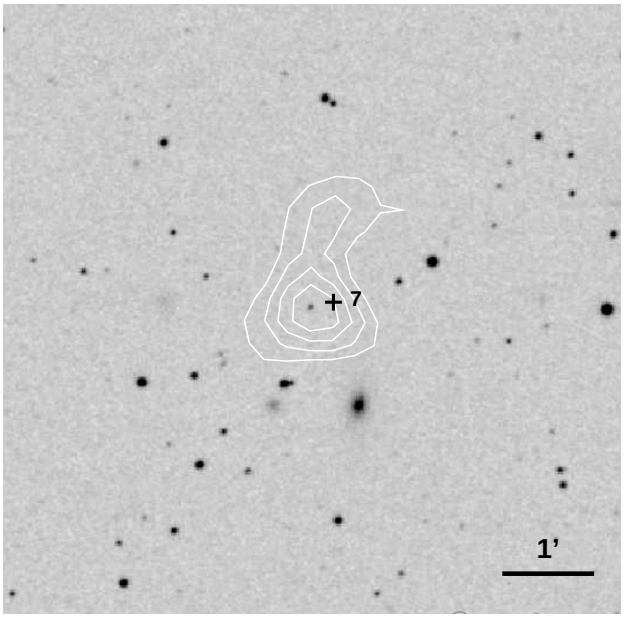

Fig. 4.16.— Radio contours superimposed on the optical DSS image of the region containing source No.7. The position of the X-ray centroid is marked by a cross.

Many of the sources detected in the PSPC data by Kim & Fabbiano (1995) are not detected in the HRI field. We derived upper limits on the HRI flux to find whether this result is due to the lower HRI S/N ratio or by the temporal variability of the sources. For all PSPC sources not detected in the HRI field, we extracted count rates using the radii reported in Table 2 of Kim & Fabbiano (1995) rescaled by a factor 1/3 to take into account the difference between the HRI and PSPC PRF. The background was measured locally in an annulus of radius twice the one used for the source. The resulting fluxes (obtained with the same conversion factors discussed above) and 3σ upper limits, are shown in Table 4.5. The comparison with the PSPC fluxes shows that all sources except one are below the HRI sensitivity. Source No.6 is the only one which must be significantly variable since the expected flux is higher than the 3σ upper limit indicated by the HRI data.

The implications of these results on the nature of the discrete sources found in the NGC 507/499 field will be discussed in § 4.3.4.

4.3. DISCUSSION

4.3.1. Origin of the Central Component

The surface brightness distribution shown in Figure 4.3a,b revealed the presence of a bright X-ray emission peak centered on the optical galaxy. The surface brightness profiles (Figure 4.7 and 4.8) show that the peak dominates the X-ray emission within the central 10 arcsec (3 kpc). The HRI data alone do not allow to distinguish between a pointlike or extended nature of the central peak, since the comparison of the X-ray profile with the HRI PRF (Figure 4.7) and the small core radius of the central component obtained from the bidimensional fit (Table 4.2) are marginally consistent with the presence of a nuclear X-ray source. However the displacement of the radio nucleus with respect to the X-ray peak (§ 4.2.3) seems to exclude the discrete nature of this component. This result is confirmed by the *Chandra* X-ray profile obtained recently by Forman et al. (2000).

We notice that Canosa et al. (1999), using the ROSAT HRI data, found an upper limit on the X-ray flux of a possible nuclear source that exceeds, by more than two orders of magnitude, the emission expected from the Radio data. The extended nature of the central peak implies that the flux of the nuclear source is much smaller than though before, thus reducing the disagreement between the radio and X-ray data.

The comparison between the optical and X-ray profile (Figure 4.8) seems to rule out the possibility that the central peak is due to the unresolved emission of galactic X-ray binaries. In this case the X-ray profile of the central component would be close to the optical one, since the X-ray source population should follow the stellar distribution. The previous considerations support the gaseous nature of the central peak, even though we expect some contribution from the unresolved sources present in the galaxy center.

Kim & Fabbiano (1995) noticed that significant mass deposition should be present within the cooling radius since the cooling times of the gaseous halo are smaller than the Hubble time (Figure 4.13). Their estimate (see equation 1.38), after rescaling to our adopted distance[5], yields a mass inflow rate of ~ 20 $M_\odot$ yr^{-1}. If the central X-ray peak was due to the mass deposited by the cooling flow, we would expect to find $\sim 2 \times 10^{11}$ $M_\odot$ within 250 arcsec from the galaxy center while the total mass of the central component is only $\sim 2 \times 10^9$ (Figure 4.14a) within the same radius. An identical result holds if we assume

[5]The mass inflow rate is inferred from the gas density (equation 1.38) which in turn depends on the X-ray luminosity. Since we can only measure the X-ray flux we have to rescale their estimate to our adopted distance.

an inhomogeneous flow where $\dot{M} \propto r$ (Fabian 1994). In fact, extrapolating the mass inflow down to $r = 10$" where the contribution of the central component is better defined, we obtain a deposited mass of $\sim 10^{10}$ $M_\odot$ while we observe less than 10^8 $M_\odot$. This result holds also if we take into account all the uncertainties included in the calculation such as the gas filling factor and the age of the cooling flow.

The problem of the missing deposited mass has been largely debated in literature (see for instance Fabbiano 1989; Fabian 1994; Rangarajan et al. 1995). Recently the failure to observe cool gas in the center of galaxies and clusters supposed to host large cooling flows (Matsushita et al. 2001b; Peterson et al. 2001; Kaastra et al. 2001; Tamura et al. 2001) has led many authors to stress the failure of the standard cooling flow models. In a recent study of a sample of early-type galaxies, Matsushita (2001a) noticed that the ISM temperature of X-ray compact galaxies is compatible with $\beta_{spec} \simeq 1$ where β_{spec} is defined in equation (1.30). She argues that this conclusion holds also for X-ray extended galaxies (such as NGC 507) if we consider only the inner galactic halo ($r < 1.5r_e$). The lower central temperatures would be explained by kinematical heating from stellar mass losses rather than by the cooling flow scenario.

In the case of NGC 507 the central X-ray peak may be produced by the gas ejected by the stellar population. The stellar origin of the gas is supported by the solar metallicity found by Buote (2000b) in the halo center. If the gas is in equilibrium with the stellar component, as suggested by Matsushita (2001a), we expect to find a central temperature close to 0.6 keV. The work of (Matsumoto et al. 1997), which found $\beta_{spec} \sim 0.6$, does not rule out such a possibility since it does not take into account the temperature drop within 150". In order to sample the inner 15", where the central component emission dominates, and to see if such low temperatures are present in the center of NGC 507, we will have to exploit the *Chandra* or XMM resolution.

4.3.2. X-ray/Radio Correlations

We showed in § 4.2.2 that the central NGC 507 halo has a very complex morphology. Figure 4.3 revealed the presence of secondary emission peaks and cavities in the X-ray emission. As discussed in § 2.3.2, the weak dependence of the HRI spectral response on the temperature near 1 keV (Clarke, Harris & Carilli 1997), suggests a correlation between surface brightness and density fluctuations of the hot gas. The comparison of these X-ray features with the radio maps of Figures 4.5a,b supports the scenario in which the hot gas has been displaced by the pressure of the radio-emitting plasma. In fact the very good agreement between the shape of the Western radio lobe and the X-ray cavity indicates that the lobe may have

produced a low-density 'bubble' in the gaseous medium, compressing the gas at the edge of the lobe. This interaction is also likely to be responsible for the N-S elongation of the lobe since the radio plasma expanded avoiding the denser Western and Southern regions.

The presence of such interactions is not so evident in the Eastern lobe. This may be due to projection effects and/or to the fact that the Eastern lobe seems to expand in a less dense environment (the X-ray centroid of the galactic component is displaced by $\sim$ 20"=6 kpc South-West of the nuclear radio source). The Radio/X-ray comparison in Figure 4.5a shows that a secondary emission peak lies in the center of the Eastern radio lobe. As already done in § 2.3.3, we used equations (1.17) and (1.20) to calculate the expected X-ray emission due to Inverse Compton scattering of Cosmic Background photons into the X-ray band, for a grid of values of the involved parameters. We used the radio flux for the Eastern lobe measured by de Ruiter et al. (1986) and we measured the X-ray flux density extracting counts from a 25" circle centered on the secondary emission peak. Since the X-ray flux depends on the assumed spectrum, we estimated an upper (1.18×10^{-31} ergs s^{-1}cm^{-2}Hz^{-1}) and lower (8.87×10^{-32} ergs s^{-1}cm^{-2}Hz^{-1}) limit using respectively power laws with photon index $\alpha_{ph} = 1.8$ and $\alpha_{ph} = 3$. The results are shown in Table 4.6. We found that the expected X-ray emission falls an order of magnitude below the measured excess since the ratio B_{ME}/B_{IC} is always $>> 1$ for any choise of the parameters.

Conversely, the higher resolution radio contours shown in Figure 4.5b suggest that the bulk of the radio emission may fall south of the peak, in a low emitting region. In this case both the secondary emission peak and the SE 'tongue' found in the adaptive smoothed image (Figure 4.4) may be produced by hot gas compressed by the radio-emitting plasma, similarly to what seen for the Western lobe.

The thermal confinement of the radio lobes is supported by the interactions between the radio and X-ray emitting plasma discussed above. Morganti et al. (1988) studied the pressure balance between the radio lobes and the surrounding ISM, finding that the thermal pressure greatly exceeded the radio one ($P_{thermal}/P_{radio} > 7$). However their estimate was based on *Einstein* data, which resulted in a temperature twice the ROSAT PSPC value. Taking into account the ROSAT temperature reduces the disagreement by more than 50%; the remaining excess may be explained by the departures from the minimum pressure conditions discussed in their work.

Finally we notice that no sharp features, such as shocks or knots, are seen in the HRI image, as expected in a weak radio source (Fanti et al. 1987).

Table 4.6: Eastern lobe magnetic field strenght.

η	ϕ (rad)	ν_1 (GHz)	k	S_X (ergs s^{-1}cm^{-2}Hz^{-1})	B_{ME} (μG)	B_{IC} (μG)	B_{ME}/B_{IC}
1	$\pi/2$	1.00×10^{-2}	1	1.18×10^{-31}	2.5	0.08	32
1	$\pi/6$	1.00×10^{-2}	1	1.18×10^{-31}	3.4	0.11	29
1	$\pi/2$	1.00×10^{-2}	100	1.18×10^{-31}	7.8	0.08	99
1	$\pi/2$	1.00×10^{-4}	1	1.18×10^{-31}	2.5	0.08	32
0.1	$\pi/2$	1.00×10^{-2}	1	1.18×10^{-31}	4.9	0.08	62
0.01	$\pi/2$	1.00×10^{-2}	1	1.18×10^{-31}	9.5	0.08	120
1	$\pi/2$	1.00×10^{-2}	1	8.87×10^{-32}	2.5	0.09	27
1	$\pi/6$	1.00×10^{-2}	1	8.87×10^{-32}	3.4	0.14	25

Note - The calculation uses equations (1.17) and (1.20) assuming the following parameters: radio spectral index $\alpha_r = -0.8$, radio flux density $S_r = 0.027$ Jy at $\nu_r = 1.465$ GHz, lobe diameter $\theta = 60$" and path lenght through the source $s = 19$ kpc. The X-ray flux S_X density is calculated at 1 keV assuming a galactic absorption of 5.3×10^{20} cm^{-2}; the upper syncrotron cutoff is taken to be $\nu_2 = 10$ GHz.

4.3.3. Large-scale Halo structure

In section 4.2.2 we have shown that the HRI data reveal the presence of a large halo surrounding NGC 507. Even though the irregular morphology of the halo may be affected by the low S/N ratio of the HRI data at large radii, a comparison with the PSPC image shown in Figure 4 of Kim & Fabbiano (1995) suggest that some of these features are indeed real.

The X-ray emission is more extended in the region between NGC 507 and NGC 499, creating a large halo that surrounds the two galaxies. The total mass profile (Figure 4.14b) shows that for $r > 80$" (25 kpc) the mass distribution is dominated by dark matter. If the hot gas distribution traces the gravitational potential this dark matter is distributed preferentially on group scales rather than being associated with the dominant galaxy of the cluster. In fact, on galactic scales, the total mass is compatible with the stellar matter contribution inferred from the surface brightness profile.

Exploiting the HRI resolution to study the inner halo ($r < 5'$) we found (§ 4.2.2) a complex morphology. We have seen in the previous section that some structures are likely to be due to the interaction with the radio lobes. However the presence of some 'tails', revealed by the adaptive smoothing technique (Figure 4.4), requires a different explanation.

The study of the inner halo also showed that the optical galaxy is centered on the central X-ray peak and is thus displaced with respect to the galactic halo. This result is confirmed independently by the bidimensional fit, which shows that the galactic component centroid is located $\sim 22''$ (7 kpc) South-West of the optical galaxy (Figure 4.6), and by the wavelets algorithm, which centered source No.10 (associated with the NGC 507 halo) South-West of source No.9 (coincident with the central peak, see Figure 4.3a). These results imply that the decentering of the galactic halo with respect to the optical galaxy is not an artifact produced by the X-ray/radio interactions in the halo core which displaced South-West the X-ray centroid, since the bidimensional model fitting (and to a lesser extent the wavelets algorithm) are strongly affected by the X-ray distribution at large radii.

We can imagine different scenarios to explain these observations: in the first one the hot halo distribution traces the gravitational potential. The latter is associated with the galaxy group and, instead of being centered on the dominant galaxy, is displaced toward NGC 499. This small displacement seems compatible with the distribution of galaxies within the NGC 507 group studied by Barton, de Carvalho & Geller (1998).

A second possibility is that tidal interactions between NGC 507 and NGC 499 are responsible for the asymmetries in the hot gas distribution. In § 2.3.2 we discussed the possibility that such interactions may produce large density fluctuations and the formation of filamentary structures. The presence of 'clumps' of cooler gas in the halo, suggested by Kim & Fabbiano (1995) (see § 4.3.4) may support such scenario.

The displacement of the optical galaxy with respect to the large-scale gas distribution may be produced by the motion of the stellar body within the larger galactic halo. The central component would be centered on the optical galaxy since it may be due to gas of stellar origin in equilibrium with the stellar component (§ 4.3.1). The northern tail seen in the adaptively smoothed image (Figure 4.4) may represent a cooling wake produced by such motion, similar those found by David et al. (1994) or Merrifield (1998). The smaller North-Western tail departing from the central component found in the surface brightness map and the radial brightness profiles (Figure 4.10a,b) may have a similar origin, even though we can not exclude that it simply represents a layer of gas shocked by the radio plasma on the edge of the Western radio lobe.

These considerations do not necessarily exclude each other since a combination of different effects is likely to be present in high density environments.

4.3.4. Discrete Sources

Kim & Fabbiano (1995) revealed the presence of many pointlike sources in the NGC 507 halo. The co-added spectrum of these sources was found to be well fitted by a soft thermal model (kT=0.52) with low abundance (0.0-0.2), leading the authors to speculate that they could be cooling clumps in the gaseous halo.

As discussed in § 4.2.7 we used the wavelets algorithm to investigate the nature of discrete sources in the HRI field (4.15). After excluding NGC 507 (source No.10), NGC 499 (No.11), we cross-correlated the HRI sources (Table 4.3) with those detected in the PSPC data (Table 2 of Kim & Fabbiano (1995)). Only 5 out of the 17 sources PSPC sources falling within the HRI field[6] are detected in the HRI data.

We compared the fluxes measured by the two instruments, since any temporal variability would exclude the extended nature of these sources. As shown in Tables 4.4 and 4.5 two sources varied significantly between 1993 and 1995. One more object (Source No.7) is likely to be associated with a background radio source.

In conclusion $\sim$ 20% of the sources detected by Kim & Fabbiano (1995) are likely to be compact objects; this number must be considered as a lower limit since 4 additional HRI sources possess an optical counterpart candidate. This result is not necessarily in disagreement with the soft spectrum reported by Kim & Fabbiano (1995) since recently Sarazin, Irwin & Bregman (2001) claimed the discovery of supersoft sources in NGC 4697 (even though their sources are preferentially located near the galaxy center). The nature of the remaining sources is still uncertain. If the emission is due to accreting binaries associated with NGC 507 these systems must host massive black holes since their luminosity would exceed, by at least an order of magnitude, the Eddinghton luminosity (equation 1.22) for a 1.4 $M_{\odot}$ Neutron Star. Finally, we can not exclude the diffuse origin of many sources since the irregular structure of the galactic halo and the filamentary features seen in the halo core suggest that significant density fluctuations may be present in the hot gas distribution, similar those found for NGC 1399.

[6]Sources No.1,2,19,21 of Kim & Fabbiano (1995) fall outside or on the edge of the HRI FOV.

Chapter 5

DISCUSSION

5.1. Summary of the Results

In this Section we briefly summarize the main results obtained in the previous Chapters; in the following Sections we compare the different galaxies of the sample and discuss the global properties of bright Early-Types.

5.1.1. NGC 1399

We have analyzed a deep ROSAT HRI observation centered on the cD galaxy NGC 1399, in the Fornax cluster, in conjunction with the archival ROSAT PSPC data of the same field. We found an extended and asymmetric halo extending on cluster scales ($r > 90$ Kpc). The halo profile is not consistent with a simple Beta model but suggests the presence of three different components. The combined HRI and PSPC data were fitted with a multi-component bidimensional model, consisting of: (1) a 'central' component (dominating for $r < 50$") centered on the optical galaxy and whose distribution follows the luminous matter profile; (2) a 'galactic' component ($50" < r \leq 400"$) displaced $1'$ (5 kpc) South-West of NGC 1399 and (3) a 'cluster' ellipsoidal component ($r > 400"$) centered $\sim 5.6'$ (31 kpc) North-East of the galaxy. The HRI image also revealed the existence of filamentary structures and cavities in the galactic halo, due to density fluctuations in the hot gas. The presence of these features is confirmed by a preliminary analysis of *Chandra* data.

The large scale surface brightness distribution can be explained if the galaxy hosts a large dark halo with different dark matter distributions on galactic and cluster scales (Saglia

et al. 2000; Ikebe et al. 1996). Alternative models, that explain the GCs abundance and its optical velocity dispersion profiles through tidal interactions with Fornax cluster galaxies (Kissler-Patig et al. 1999; Napolitano, Arnaboldi & Capaccioli 2001, in preparation), are compatible with our data only if such encounters result in shallower slope of the outer gas distribution. Tidal interactions may also explain the presence of the density fluctuations in the galactic halo (D'Ercole, Recchi & Ciotti 2000). Ram pressure from the cluster halo (e.g. Irwin & Sarazin 1996; David et al. 1994; Fabian et al. 2001b) is able to account for the decentering of the optical galaxy with respect to the galactic halo if NGC 1399 is moving subsonically (10-100 km s^{-1}) in the cluster potential. The displacement of the center of the cluster component with respect to the nearest Fornax galaxies may suggest that the cluster is not relaxed and may be undergoing a merger event.

We do not detect the X-ray counterpart of the nuclear radio source (Killeen, Bicknell & Ekers 1988) and pose an upper limit of $L_X^{3\sigma} = 3.9 \times 10^{39}$ erg s^{-1} on its luminosity in the 0.1-2.4 keV band. In agreement with Killeen and collaborators, our data support thermal pressure confinement of the radio emitting plasma. We found X-ray emission enhancements aligned with the radio jets that may be due to shocked gas and X-ray 'holes' and enhancements coincident with the position of the radio lobes. The latter are consistent with a scenario in which the hot gas is displaced by the radio plasma pressure (e.g. Clarke, Harris & Carilli 1997), while alternative models of Inverse Compton scattering of Cosmic Microwave Background photons fail to account for the observed excesses.

We detected 43 discrete sources in our field. Their flux distribution is consistent at the 2σ level with the number expected from X-ray background counts. However, the spatial distribution of these sources has a significant excess peaked on the central galaxy, suggesting a population of galaxian X-ray sources in NGC 1399. This is confirmed by the *Chandra* data, that reveal a large number of point-like sources associated with the optical galaxy. These sources are likely to explain the hard component found by ROSAT and ASCA spectral analysis (Buote 1999; Matsushita, Ohashi & Makishima 2000; Allen, di Matteo & Fabian 2000).

5.1.2. NGC 1404

The surface brightness distribution of the NGC 1404 halo is regular and almost consistent with the stellar distribution. The brightness profile is well represented by a single Beta model out to 90". The similarity with the 'central' component of the NGC 1399 halo suggest that the ISM distribution of NGC 1404 is produced by the same gravitational potential that is binding the stellar population. However the agreement with the optical profile implies

that the halo is 'hotter' than the stars (Fabbiano 1989), in agreement with the spectral measurements of Matsushita (2001a).

This scenario can be explained by interactions with the surrounding environment. Indeed, for $r > 90$" the effect of ram pressure stripping becomes evident as a sharp brightness cutoff in the North-West sector and an elongated tail on the opposite side of the galaxy.

Even though the cooling times, derived from the deprojected density profile of the NGC 1404 halo, are shorter than the Hubble time, no bright emission peak due to cool gas in the galaxy center is detected. Finally, the mass profile shows no evidence of multiple components.

5.1.3. NGC 507

The ROSAT HRI data showed, in agreement with previous studies, a bright X-ray halo surrounding NGC 507. The large-scale surface brightness distribution is irregular and more extended in the North direction.

The halo core revealed a complex morphology: there is a main X-ray peak, coincident with the position of the optical galaxy, and several secondary peaks. The radial brightness profile is only marginally consistent with the presence of a nuclear point source; however recent *Chandra* data rule out this possibility. The comparison with the optical profile seems to exclude that the main peak is due to the integrated emission of unresolved point sources. We conclude that this feature is likely produced by dense hot gas in the galaxy core.

There are clear signs of interaction between the radio-emitting plasma and the surrounding ISM, producing density fluctuations in the hot gas. The evidence is stronger for the Western lobe than for the Eastern one. However alternative physical processes, such as IC scattering of background photons, predict X-ray emission an order of magnitude lower than observed.

Modeling the halo surface brightness with a bidimensional double Beta model, we found that the galactic halo centroid is displaced ~ 22" (7 kpc) South-West of the optical galaxy. This result suggests a different origin for the central and the galactic components. Even though the cooling time of the halo within 250" (80 kpc) is shorter than the Hubble time, the mass of the gas present in the central component falls two orders of magnitude below the expected amount inferred from previous works. We propose that the central component is produced by stellar mass losses, in agreement with its high metallicity found by Buote (2000b).

The displacement of the cluster halo from the optical galaxy and the filamentary struc-

tures observed in the halo core suggest that the galaxy is slowly moving within the group potential. The total mass profile derived from the bidimensional model shows that a significant amount of dark matter is required at large radii, if the gas is in hydrostatic equilibrium. The dark halo extends on cluster scales and is likely associated with the whole cluster rather than with NGC 507, since the core region within 80" is dominated by stellar matter.

We found that $\sim 20\%$ of the sources detected by Kim & Fabbiano (1995) in the NGC 507 halo are due to point sources. The nature of the remaining population is unclear. If associated with NGC 507, they can be either accreting binaries hosting a massive black hole or density clumps of the X-ray halo.

5.2. The Origin of the Central Emission Peak in NGC 1399 and NGC 507

In Chapters 4 and 2 we have shown that the X-ray halo of the two dominant galaxies analyzed in the present work, NGC 1399 and NGC 507, possess a central bright X-ray peak. These features show some interesting similarities: i) in both cases the bright peak is centered on the optical galaxy, ii) the peak is displaced several kpc (5 kpc for NGC 1399, 7 kpc for NGC 507) with respect to the galactic halo centroid, iii) the peaks cannot be due to the presence of a nuclear point source nor to an unresolved population of point sources (even though some contribution is expected) thus suggesting to originate from thermal emission from diffuse gas.

The presence of a central emission excess over a simple Beta model, often found in galaxies and cluster of galaxies (see Fabbiano 1989; Fabian 1994), is usually attributed to the presence of a cooling flow which deposits large amounts of cooler gas in the halo core (Sarazin 1988). The higher gas density should produce a bright central peak since the thermal emissivity is $\propto n_e^2$ (see equation 1.5). However this interpretation has been challenged by the finding that the observed excess is smaller than what is expected if all the cooling gas reaches the halo center (Fabian 1994). The mass deposition profiles derived by many authors have shown that $\dot{M} \propto r$ (Fabbiano 1989), thus indicating that a significant amount of cooling gas must be deposited at large radii and is not able to reach the halo core.

Our data are consistent with the hypothesis that the central peaks are not due to the gas deposited by the cooling flow. In fact the expected amount of gas deposited by the flow exceeds the mass of the central component by, at least, an order of magnitude (§ 2.3.1 and § 4.3.1). This result is valid also when we restrict the analysis to the region where the central peak dominates the emission (50" and 15" respectively for NGC 1399 and NGC 507)

and we take into account the inhomogeneous flow scenario, where only part of the cooling gas reaches the halo center. Moreover, while in the case of NGC 1399 the disagreement is reconcilable with the cooling flow scenario if we reduce to $\sim 10^9$ yr the age of the cooling flow (but we are still ignoring stellar mass losses), this solution doesn't work for NGC 507, where the disagreement is larger. A further indication that the central X-ray peak is not related to the cooling flow is its displacement from the galactic halo centroid. If the brightness excess was related to the deposited cooling gas we would expect the inflowing mass to be located approximately in the halo center.

These considerations lead us to two separate conclusions: the first one is that since the observed X-ray excess is not due to the presence of a cooling flow, the mass inflow must be significantly smaller than the rates predicted not only by homogeneous models (a well established fact) but by the inhomogeneous scenario ($\dot{M} \propto r$) as well for both galaxies, in agreement with the most recent spectroscopic results from XMM (Matsushita et al. 2001b; Peterson et al. 2001; Kaastra et al. 2001; Tamura et al. 2001).

The second conclusion is that the distribution of the denser central gas must be related to the underlying stellar distribution. In fact Brighenti & Mathews (1997) argue that the temperature drop within 4 effective radii (r_e) observed in many galaxies, including NGC 507 and NGC 1399, is not a natural result of cooling flow models. Matsushita (2001a) studied the spectral properties of a sample of Early-Type galaxies as a function of the distance from the halo center and found that the hot corona of X-ray compact galaxies is likely due to the gas injected into the ISM by stellar losses. The X-ray luminosities and temperatures are compatible with the expectations obtained considering stellar motions as the main source of heat, leading to a mean value of $\beta_{spec} \simeq 1$ (see equation 1.30). X-ray extended galaxies as NGC 1399, instead, have a mean halo temperature which exceeds the value expected if the gaseous component is in equilibrium with the stellar population ($\beta_{spec} \simeq 0.5$).

This difference between compact and extended galaxies is reduced if we restrict the analysis to the region within $\sim 1\ r_e$ from the galaxy center. In the case of NGC 1399 $\beta_{spec} \simeq 0.9$ for $r \leq r_e \simeq 45$" (r_e is from Faber et al. 1989), i.e. the region dominated by the central X-ray peak. Taking advantage of the HRI resolution we can further improve this result. Matsushita (2001a) could not sample the luminosity of the region within 1.5 r_e because of the large PSPC PRF. Our data, instead, indicate that reducing the region observed down to r_e the X-ray flux is reduced to $\sim 40\%$ so that the luminosity of NGC 1399 is comparable to the energy injected in the ISM by stellar motions (see Figure 4 of Matsushita 2001a).

In the case of NGC 507 the correlation between the stellar population and the central component is less obvious. In fact, if the central peak is produced by stellar mass losses, we would expect its extension to be related to the underlying stellar distribution. The extension

of the central peak is $r \simeq 5$ kpc in both NGC 1399 and NGC 507 but, while this radius is comparable with the optical effective radius for the former, the latter has a broader optical distribution with $r_e \simeq 77$"(Faber et al. 1989). The discrepancy is solved in part by noting that the NGC 507 galactic halo has a central density approximately twice the one of NGC 1399, which gives a surface brightness ~ 4 times higher (the thermal emissivity scales as n_e^2, see equation 1.5). Thus the larger galactic halo luminosity prevents the observer to follow the central peak brightness, which declines as $r^{-2.5}$, out to large radii. Moreover the interaction between the ISM and the radio lobes (§ 4.2.3) may have significantly altered the ISM distribution of the central component, thus making a comparison with NGC 1399 more difficult.

The comparison of the hot plasma temperature with the one expected assuming dynamical equilibrium with the stellar component is a difficult task for NGC 507. It requires to obtain a reliable spectrum from the central 15", which has become possible only very recently with the *Chandra* and XMM satellites and whose data are not available yet. Matsumoto et al. (1997) found $\beta_{spec} \sim 0.6$ for NGC 507; however they used a 1.4 arcmin extraction radius which is much larger than the central peak extension. Taking into account the central temperature drop and the fact that Matsumoto and collaborators found a 20% lower temperature using the MEKA model (Mewe, Gronenschild & van den Oord 1985) instead of the classical Raymond-Smith code (Raymond & Smith 1977), we believe that the current data are compatible with a β_{spec} value close to one, as found for NGC 1399.

We conclude that the central X-ray peak found in NGC 507 and NGC 1399 are likely to be produced by the material ejected by stars in the ISM. The same mechanism at work in X-ray compact galaxies, i.e. kinematical heating by stellar mass losses, may be responsible for the cooler core observed in many bright Early-Type galaxies, even though some contribution from cooling gas can not be excluded.

5.3. Dynamical Status of the Halo

The bidimensional models used in § 2.2.5 and 4.2.4 to describe the structure of the X-ray halo surrounding NGC 1399 and NGC 507, allowed us to separate the compact central component (discussed in previous section) from the gaseous halo components extending on galactic and on cluster spatial scales. In both galaxies we found a displacement of several kpc between the X-ray centroid of these extended components and the optical galaxy. Assuming hydrostatic equilibrium we further showed that the total mass (Figures 2.15b and 4.14b) is dominated by stellar matter within a few effective radii from the optical centroid while, at larger distances, there is a significant contribution of dark matter.

These two results (the displacement of the optical galaxy and the small contribution of dark matter on galactic scales) suggest that the gas distribution on large scales is mostly determined by the cluster potential rather than being associated with the dominant galaxy. The comparison of the halo temperature outside a few effective radii and the stellar velocity dispersion yield values of $\beta_{spec} \simeq 0.5$ (Matsumoto et al. 1997; Brown & Bregman 1998, 2000; Matsushita 2001a) thus supporting the need for additional heat to the one provided by stellar mass losses alone. Sources of heat such as a central active nucleus or supernovae explosions, are not enough to account for the observational data (e.g. Matsumoto et al. 1997) and would however affect in first place the halo center. The alternative explanation proposed by Makishima et al. (2001) and Matsushita (2001a) is that X-ray extended galaxies are at the bottom of large potential structures corresponding to galaxy groups, which provide the additional heat by gravitational infall. This scenario is consistent with our data which show that both NGC 1399 and NGC 507 lie at the center of extended dark halos.

Nevertheless the X-ray halo presents one main difference between the two galaxies (Figure 2.11 and 4.8): to model the surface brightness distribution of NGC 1399 we had to introduce three different components which we associated with the central, galactic and cluster halo. Conversely the NGC 507 halo structure could be modeled with only two components. Comparing our total mass profiles to those obtained by other authors (Brighenti & Mathews 1997; Matsushita et al. 1998; Matsushita 2001a; Matsushita et al. 2001b) in bright Early-Types we find that a double structure is quite common. All these authors found a central region, within a few effective radii, dominated by stellar matter and a large dark halo extending outside the optical galaxy, in analogy with our findings. The mass profiles are thus tracing the galactic potential in the inner region and the dark extended halo elsewhere. It is however very difficult to assess the presence of a third component since this requires data of both high S/N ratio and high spatial resolution.

Two possibilities arise from this discussion: the first is that the galactic and cluster halo components are two separate entities reflecting the hierarchical nesting of the dark matter halos around dominant elliptical galaxies. In this case two separate components may be present in all bright Early-Types but, depending on the contribution of each component, their discovery through surface brightness analysis may be difficult, since the superposition can mimic a one-component profile. NGC 1399 may be a lucky case where the displacement of the different components and the faintness of the cluster halo makes the multi-component structure more evident. In this case we expect the galactic and cluster components to have different spectral signatures. In fact the region where the galactic component dominates the X-ray emission roughly coincides with the temperature maxima found by Kim & Fabbiano (1995). Spatially resolved spectroscopic studies with *Chandra* may test such a possibility.

This scenario holds if we assume that the gas distribution is tracing the gravitational potential, i.e. is in hydrostatic equilibrium. Thus an alternative possibility is that other physical mechanisms, such as tidal interactions (D'Ercole, Recchi & Ciotti 2000, e.g.), ram pressure (Toniazzo & Schindler 2001) or galactic wind stifling from the ICM (Brown & Bregman 1998, 2000) are significantly altering the hot gas distribution. As discussed in § 2.3.2, some of these effects (ram pressure, tidal interactions) may explain the displacement beween the optical galaxy and the galactic halo component, which is otherwise difficult to account for in the hierarchical dark halo scenario.

5.4. NGC 1404: a peculiar galaxy?

Our study of NGC 1404 was motivated by the fact that this galaxy, even though it is not a dominant cluster member, represents a very bright Early-Type with an X-ray luminosity ($L_X \sim 1.6 \times 10^{41}$ erg s^{-1}) of the same order of magnitude of NGC 1399. This X-ray luminosity is one order of magnitude larger than other Early-Types with similar optical luminosity (Brown & Bregman 1998; Irwin & Sarazin 1998b) and exceeds the one expected from kinetical heating by stellar mass losses (Matsushita 2001a). The hot halo temperature ($kT \sim 0.6$ keV) exceeds the one expected from the stellar velocity dispersion ($\sigma \sim 220 - 250$ Km s^{-1}, D'Onofrio et al. 1995; Graham et al. 1998) yielding $\beta_{spec} \sim 0.6$ (Brown & Bregman 1998; Matsushita 2001a). Although some authors (D'Onofrio et al. 1995; Graham et al. 1998) noticed that NGC 1404 has a large rotation velocity (~ 100 Km s^{-1}) and is thus likely to be a misclassified S0 galaxy, even taking into account the rotational contribution we still obtain $\beta_{spec} \leq 0.7$.

All these facts suggest that NGC 1404 is more similar to X-ray extended galaxies, such as NGC 1399 and NGC 507, than to compact galaxies of similar optical luminosity and velocity dispersion. However the analysis presented in Chapter 3 shows a number of significant differences: i) the X-ray surface brightness of NGC 1404 is smooth and is consistent with the stellar distribution; ii) the radial brightness profile is well represented by a single Beta model and there is no sign of the presence of a multi component structure; iii) the X-ray and optical profiles are in good agreement, suggesting once more that $\beta_{spec} \sim 0.5$ (see § 3.3). Moreover the hot halo is characterized by a very subsolar metallicity (Loewenstein et al. 1994; Jones et al. 1997), in contrast with the solar abundances found in the center of many bright ellipticals (Buote & Fabian 1998; Buote 2000b; Matsushita, Ohashi & Makishima 2000).

The cooling times and total mass profiles derived in Chapter 3 are more similar to the profiles of the central components derived for NGC 1399 and NGC 507 than to the properties of the extended galactic and cluster halo, thus suggesting a similar origin. However in this

case we would expect $\beta_{spec} \simeq 1$ as found for the central components of the two dominant galaxies (§ 5.2).

These conflicting evidences suggest that NGC 1404 is a peculiar galaxy and other physical mechanisms must be responsible for the status of the hot halo. Matsushita (2001a) noticed that environmental effects must be important since NGC 1404 is embedded in the NGC 1399 halo. We have seen that NGC 1404 possess an elongated tail which is likely to be produced by ram pressure from the surrounding ICM. Toniazzo & Schindler (2001) simulated the effects of ram pressure stripping on galaxies similar to NGC 1404 finding that it could explain differences in the X-ray luminosity similar to those observed between NGC 1404 and other Early-Types. Anyway a comparison is difficult since their models predict a higher halo temperature and steeper brightness profiles than observed, indicating that the balance between mass injection from stellar losses and cooling dropout is not well understood. Moreover the radial profiles shown in Figure 3.2b also showed that ram pressure stripping seems to affect the galactic halo only at large radii ($r > 3\ r_e$).

Brown & Bregman (1998, 2000) proposed that the temperature excess, over the value calculated from stellar velocity dispersion, can be produced by supernovae heating. This would produce strong stellar winds, thus reducing the total X-ray luminosity. Conversely, in high density environment, the stifling of galactic winds by the surrounding ICM pressure would increase the total luminosity of the galaxy. This scenario conflicts with the very low metallicity observed in the NGC 1404 halo, because high supernova rates lead to higher abundances. However Loewenstein et al. (1994) notice that the presence of a metallicity gradient in the NGC 1404 halo (maybe due to the subsolar ICM abundance), may bias the ASCA results, which are affected by the low spatial resolution. This hypothesis is supported by the larger $Z \sim 0.59\ Z_\odot$ metallicity reported by Matsushita (2001a) within 4 r_e.

The peculiar nature of NGC 1404 suggests the need for further studies; in fact this object represents a very good candidate to understand the effect of the environment on the physical status of the X-ray halo.

5.5. Density Fluctuations in the ISM

Most of the work done on Early-Type X-ray halos has been based on the simplified assumption of homogeneity and spherical symmetry. These assumptions were based mainly on the low spatial resolution of the X-ray satellites before ROSAT. Our HRI observations have shown the presence of significant brightness fluctuations and filamentary structures in the halo of both NGC 1399 and NGC 507. Since the ROSAT HRI spectral response is weakly

dependent on the temperature (Clarke, Harris & Carilli 1997), these features must reflect density fluctuations in the hot gas distribution. Excluding the structures clearly associated to the radio jets and lobes (see next section), these features have no obvious explanation. In § 2.3.2 we discussed a number of possible scenarios that could account for the density fluctuations found in the NGC 1399 halo, including tidal interactions with nearby galaxies and ram pressure stripping of the galactic corona by the ICM.

We were not able to detect these features with comparable significance in the NGC 507 halo, because of the poorer S/N ratio of the data. In the halo center, where the S/N ratio is higher, the adaptive smoothing technique revealed the presence of filamentary structures. At larger radii the presence of 'clumps' in the hot plasma was reported by Kim & Fabbiano (1995) using ROSAT PSPC data. Our HRI analysis showed that $\sim 20\%$ of these sources are likely to be point sources but the origin of the remaining objects is still uncertain. We can speculate that they reflect a complex structure of the X-ray halo similar to those found in the dominant Fornax galaxy.

The current data do not allow to distinguish between different scenarios: the central filamentary structures may represent X-ray wakes due to the motion of the galaxy within the cluster halo (David et al. 1994; Merrifield 1998). However these motions alone cannot account for the distribution of these features all over the hot halo; more complex interactions, such as those proposed for NGC 1399, must be considered. One further possibility is that this complex morphology reflects the inhomogeneity of the cooling process suggested by many authors (e.g. Kim & Fabbiano 1995; Peterson et al. 2001; Fabian et al. 2001a), thus giving important clues to understand the failure of cooling-flow models.

We expect that significant insight in the nature of these structures will come shortly from the analysis of *Chandra* and XMM data.

5.6. X-ray/Radio Interaction

Both dominant galaxies studied in this work (NGC 1399 and NGC 507) are faint radio sources. The analysis performed in § 2.2.8 and § 4.2.3 revealed the presence of interactions between the radio emitting plasma and the ISM. Such interactions have been predicted by several authors (e.g. Clarke, Harris & Carilli 1997; Reynolds, Heinz & Begelman 2001) and actually observed in many clusters of galaxies (Böhringer et al. 1993; McNamara et al. 2000; Fabian et al. 2000) and in a limited number of strong radio galaxies (e.g. Carilli, Perley & Harris 1994). Our data extends this result to weak radio sources as well, confirming that the interaction of radio jets and lobes with the surrounding medium is a widespread phenomena.

This interaction shows both similarities and differences between NGC 507 and NGC 1399: in both galaxies we found a low-emission region coincident with the position of the brighter radio lobe and excess emission at the edge of the lobe. We showed that the most likely explanation of these brightness variations is a change in the environmental gas density produced by the radio plasma pressure. However, while for NGC 1399 these features have been clearly revealed only by the adaptive smoothing technique, in the case of NGC 507 the effect of the radio lobes on the central halo morphology is immediately evident. Moreover the NGC 1399 radio jet and lobe morphology is only slightly disturbed while in NGC 507 the lobes look irregular and more diffuse.

A possible interpretation of these differences can be found in the different gas density in the galactic halo core. The electron density profiles, presented in Figures 2.13 and 4.12, show that the NGC 507 halo density (and thus the pressure since the halo temperatures are similar) is more than twice the NGC 1399 value. This must produce a stronger interaction in NGC 507, in qualitative agreement with the observations.

Finally our data confirm the role played by ISM to confine and shape the radio plasma: in both galaxies the radio and thermal pressure are found to be in good agreement while high density regions are usually associated to 'anomalies' in the radio lobe morphology.

5.7. Discrete Sources Population

The contribution of discrete sources to the total X-ray emission of Early-Type galaxies has been widely discussed in literature. However, before the launch of *Chandra*, most evidence was indirect, obtained through spectral analysis and by extrapolation from nearby Late-Type galaxies. Our analysis revealed a large number of sources associated with NGC 1399, within a few effective radii from the galaxy center. This result was confirmed by the high resolution *Chandra* observation. The brightest point sources seem to be located, in prevalence, in the globular clusters surrounding the cD galaxy, as shown by Angelini, Loewenstein & Mushotzky (2001).

As for NGC 507, the lower quality of the data did not allow us to perform a similar analysis; hence we will have to wait for higher quality *Chandra* data.

CONCLUSIONS

In this work we presented the study of three bright Early-Type galaxies hosted in groups or poor clusters of galaxies. We used ROSAT HRI and PSPC data to study the morphological structure of the X-ray halo and, when available, the higher resolution *Chandra* data.

Our study revealed a complex halo structure for the two dominant cluster galaxies, NGC 1399 and NGC 507, not well described by a simple Beta model. The halo center was found to be dominated by a bright X-ray peak coincident with the position of the optical galaxy. This central peak is not explained by the classical homogeneous or inhomogeneous cooling flow models. Instead our data suggest that these features are produced by stellar ejected material, kinetically heated by stellar mass losses.

The total mass distribution shows that within the effective radius the hot halo distribution is essentially tracing the galactic potential, dominated by luminous matter. At larger distances from the galaxy center the X-ray surface brightness and temperature require the presence of a large amount of dark matter. The presence of a different dynamical regime depending on the galactocentric distance was already found by many authors. Our study, however, clearly associates the central halo region with the stellar distribution and the external regions with the dark halo which extends on group and cluster spatial scales.

The NGC 1399 X-ray halo possess a more complex morphology than NGC 507. This finding requires either that the dark matter distribution has a hierarchical structure, or that environmental effects (ram stripping from ICM, tidal interaction with nearby galaxies) are producing departures from hydrostatic equilibrium. The latter hypothesis would explain the displacement between the different halo components, which is difficult to account for otherwise.

We found significant density fluctuations in the hot gas distribution of both NGC 1399 and NGC 507. Some of these features are explained by the interaction of the radio-emitting plasma, filling the radio jets and lobes, with the surrounding ISM. This evidence indicates that Radio/X-ray interactions are a more widespread phenomena than observed before. The

nature of the remaining structures is more uncertain: we speculate that they can be the result of galaxy-galaxy encounters or wakes produced by the motion of the galaxy through the ICM. Alternatively they may reflect the inhomogeneity of the cooling process invoked by many authors as an explanation for the failure of the standard cooling-flow models.

NGC 1404 represents a puzzling case. In fact, despite a large X-ray luminosity and halo temperature, which suggest a similarity with dominant cluster members, significant differences are found in the regular halo profile, small velocity dispersion and low metallicity. These conflicting evidences can be explained assuming again strong environmental effects. Even though NGC 1404 is indeed experiencing ram pressure stripping from the NGC 1399 extended halo, as demonstrated by the elongated SE 'tail', this phenomena seems to affect only the outer halo regions. A more promising explanation is, instead, the stifling of galactic winds by the ICM.

We studied the population of discrete sources found in proximity of the two dominant galaxies. We were able to assess that the observed excess of sources observed in the Fornax cluster is associated with NGC 1399. This result was later confirmed by the higher resolution *Chandra* data.

ACKNOWLEDGEMENTS

I wish to thank in first place my supervisor G. Peres, at the Palermo University, and G. Fabbiano, at the Harvard-Smithsonian Center for Astrophysics (C.f.A.) in Cambridge (MA - USA), for introducing and guiding me through the field of X-ray astronomy, and Dong-Woo Kim (C.f.A.) for the time dedicated to address my doubts about X-ray data reduction and interpretation.

Moreover:
– Dan Harris, at the C.f.A., for the useful discussions on the radio data interpretation;
– S. Sciortino and F. Damiani, of the Palermo Observatory, for advice on the use of the GALPIPE database and of the wavelets algorithm;
– Prof. N. Robba and Prof. M. Gelardi, of the Palermo University, for the useful suggestions on how to improve this thesis.

I'm also thankful to the Harvard-Smithsonian Center for Astrophysics, for welcoming me during my three visits to Cambridge, from 1999 to 2001.

Finally a special thank goes to my colleagues and to all the people working at the Palermo Observatory for making so pleasant these three years spent in Sicily.

This research has made use of:
- the NASA/IPAC Extragalactic Database (NED) which is operated by the Jet Propulsion Laboratory, California Institute of Technology, under contract with the National Aeronautics and Space Administration;
- the NASA Astrophysics Data System Bibliographic Services;
- data obtained from the High Energy Astrophysics Science Archive Research Center (HEASARC), provided by NASA's Goddard Space Flight Center.

LIST OF ACRONYMS AND ABBREVIATIONS

ACIS	-	AXAF Charged coupled Imaging Spectrometer (on board of the *Chandra* satellite)
ADAF	-	Advection Dominated Accretion Flow
AGN	-	Active Galactic Nucleus
ASCA	-	Advanced Satellite for Cosmology and Astrophysics
AU	-	Astronomical Unit (1 AU = 1.49×10^{13} cm)
AXAF	-	Advanced X-ray Astronomical Facility: former name of the *Chandra* satellite
BBXT	-	Broad Band X-ray Telescope
BETG	-	Bright Early-Type Galaxies
BH	-	Black Hole
cD	-	cD galaxy: elliptical galaxy embedded in an extended amorphous halo (see § 1.1)
CIAO	-	Chandra Interactive Analysis of Observations (standard analysis tool for *Chandra* data)
cnt	-	count
CXC	-	*Chandra* X-ray Center
Dec	-	Declination
DSS	-	Digital Sky Survey
EXOSAT	-	European X-ray Space Agency Telescope
FOV	-	Field Of View
FWHM	-	Full Width Half Maximum
HEAO	-	High Energy Astrophysical Observatory
HEASARC	-	High Energy Astrophysics Science Archive Research Center
HMXB	-	High Mass X-ray Binaries
HRI	-	High Resolution Camera (on board of *Einstein* and ROSAT satellites)
HST	-	Hubble Space Telescope

IPC	-	Imaging Proportional Counter (on board of the *Einstein* satellite)
IRAF	-	Image Reduction and Analysis Facility
IC	-	Inverse Compton
ICM	-	Intra Cluster Medium
ISM	-	Inter Stellar Medium
$L_\odot$	-	Solar luminosity
L_B, L_V	-	Optical luminosity in the B ($\lambda_{eff} \sim 4300$ Å) and V ($\lambda_{eff} \sim 5500$ Å) bands
LMXB	-	Low Mass X-ray Binaries
$M_\odot$	-	Solar mass
M_B, M_V	-	Absolute magnitudes in the B ($\lambda_{eff} \sim 4300$ Å) and V ($\lambda_{eff} \sim 5500$ Å) optical bands
MEKA	-	Emissivity model for a thin hot plasma developed by Mewe, Gronenschild & van den Oord (1985)
N_H	-	The amount of H per cm^{-2} interposed between the source and the observer, used to estimate the absorption due to the ISM.
NED	-	Nasa Extragalactic Database
NS	-	Neutron Star
OBI	-	OBservation Interval: temporal intervals in which each ROSAT observation is divided
pc	-	parsec (1 pc = 3.1×10^{18} cm)
P.A.	-	Position Angle: measured counter-clockwise starting from the North
P.I.	-	Principal Investigator: the main scientist involved in a scientific project.
PIMMS	-	Portable Interactive Multi-Mission Simulator (X-ray software)
PROS	-	Post Reduction Off-line Software
PRF	-	Point Response Function
PSPC	-	Position Sensitive Proportional Counter (on board of the ROSAT satellite)
QSO	-	Quasi Stellar Object (also quasar)
RA	-	Right Ascension
r_e	-	galactic effective radius obtained from the surface brightness profile (see § 1.1)
ROSAT	-	Roentgen Satellite
RS CVn	-	Late-type, evolved (spectral type K) stars with high coronal activity, found in binary systems
S/N	-	Signal to Noise ratio
SASS	-	Standard Analysis Software System (standard processing for ROSAT data)
SAX	-	Satellite per Astronomia X (also Beppo-SAX)
SED	-	Spectral Energy Distribution

SN, SNe	-	Supernova, Supernovae
SNR	-	Supernova Remnants
SSC	-	Synchrotron Self Compton
ULX	-	Ultra Luminous X-ray source
XMM	-	X-ray Multi Mirror telescope (also XMM-Newton)
Xspec	-	X-ray spectral analysis tool
yr	-	year
Z	-	metallicity: abundance of elements with atomic number > 2. $Z_\odot$ means the solar metallicity.

BIBLIOGRAPHY

Albert, C. E., White, R. A., & Morgan, W. W. 1977, ApJ, 211, 309

Allen, S. W., di Matteo, T., & Fabian, A. C. 2000, MNRAS, 311, 493

Angelini, L., Loewenstein, M., & Mushotzky, R. F. 2001, ApJ, 557L, 35

Arimoto, N., Matsushita, K., Ishimaru, Y., Ohashi, T., Renzini, A. 1997, ApJ, 477, 128

Arnaboldi, M., Freeman, K. C., Hui, X., Capaccioli, M., & Ford, H. 1994, Messenger, 76, 40

Bahcall, N. A. 1996, "Clusters and superclusters of galaxies" in *Formation and Structure of the Universe*, 1995 Jerusalem Winter School

Barnes, J. E. 1988, ApJ, 331, 699

Barnes, J. E. 2000, to appear in "Stellar Collisions, Mergers, and Their Consequences", M. Shara, ed., astro-ph/0010145

Barnes, J. E., & Hernquist, L. 1992, ARA&A, 30, 705

Barton, E. J., de Carvalho, R. R., & Geller, M. J. 1998, AJ, 116, 1573

Bautz, L. P., & Morgan, W. W. 1970, ApJ, 162L, 149

Bender, R. 1988, A&A, 202L, 5

Bertin, G., & Toniazzo, T. 1995, ApJ, 451, 111

Bertola, F., & Galletta, G. 1978, ApJ, 226, 115

Binney, J., & Cowie, L. L. 1981, 247, 464

Binney, J., & Tremaine, S. 1987, *Galactic Dynamics*, Princeton University Press, Princeton, NJ

Biretta, J. A., Stern, C. P., & Harris, D. E. 1991, AJ. 101, 1632

Boella, G., Butler, R. C., Perola, G. C., Piro, L., Scarsi, L., & Bleeker, J. A. M. 1997, A&AS, 122, 299

Böhringer, H., Voges, W., Fabian, A.C., Edge, A.C., & Neumann, D.M., 1993, MNRAS, 264L, 25

Bregman, J. N., Miller, E. D., & Irwin, J. A. 2001, ApJ, 553L, 125

Brighenti, F., & Mathews, W. G. 1997, ApJ, 486L, 83

Brown, B. A., & Bregman, J. N. 1998, ApJ, 495L, 75

Brown, B. A., & Bregman, J. N. 2000, ApJ, 539, 592

Brunetti, G., Cappi, M., Setti, G., Feretti, L., & Harris, D.E. 2001, A&A, 372, 755

Buote, D. A. 1999, MNRAS, 309, 685

Buote, D. A. 2000a, MNRAS, 311, 176

Buote, D. A. 2000b, ApJ, 539, 172

Buote, D. A., Canizares, C. R., & Fabian, A. C. 1999, MNRAS, 310, 483

Buote, D. A., & Fabian, A. C. 1998, MNRAS, 296, 977

Byram, E. T., Chubb, T. A., & Friedman, H. 1966, Science, 152, 66

Canizares, C. R., Fabbiano, G., & Trinchieri, G. 1987, ApJ, 312, 503

Canizares, C. R., Stewart, G. C., & Fabian, A. C. 1983, ApJ, 272, 449

Canosa, C. M., Worrall, D. M., Hardcastle, M. J., & Birkinshaw, M. 1999, MNRAS, 310, 30

Caon, N., Capaccioli, M., & D'Onofrio, M. 1993, MNRAS, 265, 1013

Capaccioli, M. 1989, in 'The World of Galaxies', Conference proceedings, Paris; ed. Springer-Verlag, New-York

Capaccioli, M., & Longo, G. 1994, A&A Rev, 5, 293

Carilli, C.L., Perley, R.A., & Harris, D.E. 1994, MNRAS, 270, 173

Carter, D., & Malin, D. F. 1983, MNRAS, 203, 49

Cavaliere, A., & Fusco-Femiano, R. 1976, A&A, 49, 137

Chandrasekhar, S. 1942, *Principles of Stellar Dynamics*, Chicago: University of Chicago, p. 231

Christlein, D. 2000, ApJ, 545, 145

Clarke, D.A., Harris, D.E., & Carilli, C.L. 1997, MNRAS, 284, 981

Colla, G., Fanti, C., Fanti, R., Gioia, I., Lari, C., Lequeux, J., Lucas, R., & Ulrich, M. H. 1975, A&AS, 20, 1

Conti, P. S. 1978, A&A, 63, 225

Damiani, F., Maggio, A., Micela, G., Sciortino, S. 1997a, ApJ, 483, 350

Damiani, F., Maggio, A., Micela, G., Sciortino, S. 1997b, ApJ, 483, 370

David, L. P., Forman, W., & Jones, C. 1991, ApJ, 380, 39

David, L. P., Harden, Jr., F. R., Kearns, K. E., & Zombeck, M. V. 1996, The ROSAT High Resolution Imager (HRI), Calibration Report 1996 February, revised, U.S. ROSAT Science Data Center, SAO, Cambridge, MA

David, L. P., Jones, C., Forman, W., & Daines, S. 1994, ApJ, 428, 544

David, L. P., Nulsen, P. E. J., McNamara, B. R., Forman, W., Jones, C., Ponman, T., Robertson, B., & Wise, M. 2001, ApJ, 557, 546

Davidson, K., & Ostriker, J. P. 1973, ApJ, 179, 585

D'Ercole, A., Recchi, S., & Ciotti, L. 2000, ApJ, 533, 799 (DRC)

de Ruiter, H. R., Parma, P., Fanti, C., & Fanti, R. 1986, ApJS, 65, 111

de Vaucouleurs, G. 1948 Annales d'Astrophysique, 11, 247

de Vaucouleurs, G., de Vaucouleurs, A., Corwin, H. G. Jr., Buta, R. J., Paturel, G., & Fouqué, P. 1991, Third Reference Catalogue of Bright Galaxies (New York: Springer) (RC3)

de Zeeuw, T., & Franx, M. 1991, ARA&A, 29, 239

Djorgovski, S., & Davis, M. 1987, ApJ, 313, 59

D'Onofrio, M., Zaggia, S. R., Longo, G., Caon, N., & Capaccioli, M. 1995, A&A, 296, 319

Dressler, A., Lynden-Bell, D., Burstein, D., Davies, R. L., Faber, S. M., Terlevich, R., Wegner, G. 1987, ApJ, 313, 42

Drinkwater, M. J., Gregg, M. D., & Colless, M. 2001, ApJ, 548L, 139

Ekers, R. D., et al. 1989, MNRAS, 136, 737

Elvis, M., Cooke, B. A., Pounds, K. A., & Turner, M. J. 1975, Nature, 257, 33

Eskridge, P. B., Fabbiano, G., & Kim, D.-W. 1995, ApJ, 448, 70

Fabbiano, G. 1984, in *X-Ray Astronomy '84*, ed. M. Oda, R.Giacconi, p.333, Tokyo: Inst. Space Astronaut. Sci.

Fabbiano, G. 1989, ARA&A, 27, 87

Fabbiano, G. 1998, IAUS, 188, 93

Fabbiano, G., & Schweizer, F. 1995, ApJ, 447, 572

Fabbiano, G., Kim, D.-W., & Trinchieri, G. 1992, ApJS, 80, 531

Fabbiano, G., Kim, D.-W., & Trinchieri, G. 1994, ApJ, 429, 94

Faber, S. M., Wegner, G., Burstein, D., Davies, R. L., Dressler, Alan, Lynden-Bell, D., Terlevich, R. J. 1989, ApJS, 69, 763

Fabian, A. C. 1994, ARA&A, 32, 277

Fabian, A. C., Hu, E. M., Cowie, L. L., & Grindlay, J. 1981, ApJ, 248, 47

Fabian, A. C., Mushotzky, R. F., Nulsen, P. E. J., & Peterson, J. R. 2001a, MNRAS, 321L, 20

Fabian, A. C., & Nulsen, P. E. J. 1977, MNRAS, 180, 479

Fabian, A. C., Nulsen, P. E. J., & Canizares, C. R. 1991, A&A Rev, 2, 191

Fabian, A. C., Sanders, J. S., Ettori, S., Taylor, G. B., Allen, S. W., Crawford, C. S., Iwasawa, K., & Johnstone, R. M. 2001b, MNRAS, 321L, 33

Fabian, A. C., et al. 2000, MNRAS, 318L, 65

Fabricant, D., Lecar, M., & Gorenstein, P. 1980, ApJ, 241, 552

Fanti, C., Fanti, R., De Ruiter, H. R., Parma, P. 1987, A&AS, 69, 57

Feigelson, E. D., Laurent-Muehleisen, S. A., Kollgaard, R. I., Fomalont, E. B. 1995, ApJ, 449L, 149

Ferguson, H. C. 1989, AJ, 98, 367

Finoguenov, A., & Jones, C. 2001, ApJ, 547L, 107

Forbes, D. A., Grillmair, C. J., Williger, G. M., Elson, R. A. W., & Brodie, J, P. 1998, MNRAS, 293, 325

Forman, W., Jones, C., & Tucker, W. 1985, ApJ, 293, 102

Forman, W., Markevitch, M., Jones, C., Vikhlinin, A., & Churazov, E. 2000, astro-ph/0110087

Fritz, G., Davidsen, A., Meekings, J. F., & Friedman, H. 1971, ApJ, 164L, 81

Gallagher, J. S., & Ostriker, J. P. 1972, ApJ, 77, 288

Ghosh, P., & White, N. E. 2001, ApJ, 559L, 97

Giacconi, R., et al. 1979, ApJ, 230, 540

González-Serrano, J. I., & Carballo, R. 2000, A&AS, 142, 353

Gorenstein, P., Fabricant, D., Topka, K., Harnden, F. R. Jr., & Tucker, W. H. 1978, ApJ, 224, 718

Goudfrooij, P., Hansen, L., Jørgensen, H. E., Nørgaard-Nielsen, H. U., de Jong, T., & van den Hoek, L. B., 1994, A&AS, 104, 179

Graham, A. W., Colless, M. M., Busarello, G., Zaggia, S., & Longo, G. 1998, A&AS, 133, 325

Grillmair, C. J., Freeman, K. C., Bicknell, G. V., Carter, D., Couch, W. J., Sommer-Larsen, J., & Taylor, K. 1994, ApJ, 422L, 9

Gunn, J. E., & Gott, J. R. I. 1972, ApJ, 176, 1

Gunn, J. E., & Tinsley, B. M. 1976, ApJ, 210, 1

Harris, D. E. 1999, in Proceedings of the colloquium "The Most Distant Radio Galaxies", Amsterdam, Royal Netherlands; eds: H. J. A. Rttgering, P. N. Best and Lehnert

Harris, D. E., Carilli, C. L., & Perley, R. A. 1994, Nature, 367, 713

Harris, D. E., & Grindlay, J. E. 1979, MNRAS, 188, 25

Harris, D. E., Silverman, J. D., Hasinger, G., & Lehmann, I. 1998, A&AS, 133, 431

Hasinger, G., Burg, R., Giacconi, R., Hartner, G., Schmidt, M., Trumper, J., Zamorani, G., 1993, A&A, 275, 1

Helsdon, S.F., Ponman, T. J., O'Sullivan, E., & Forbes, D. A. 2001, MNRAS, 325, 693

Hernquist, L. 1993, ApJ, 409, 548

Hilker, M., Infante, L., & Richtler, T. 1999, A&AS 138, 55

Hilker, M., Kissler-Patig, M., Richtler, T., Infante, L., & Quintana, H. 1999, A&AS, 134, 59

Hoessel, J. G. 1980, ApJ, 241, 493

Hubble, E. 1926, ApJ, 64, 321

Huchra, J. P., Vogeley, M, S., & Geller, M. J. 1999, ApJS, 121, 287

Ikebe, Y., et al. 1992, ApJ, 384L, 5

Ikebe, Y., et al. 1996, Nature, 379, 427

Irwin, J. A., & Sarazin, C. L. 1996, ApJ, 471, 683

Irwin, J. A., & Sarazin, C. L. 1998a, ApJ, 494L, 33

Irwin, J. A., & Sarazin, C. L. 1998b, ApJ, 499, 650

Irwin, J. A., Sarazin, C. L., & Bregman, J. N. 2000, ApJ, 544, 293

Jones, C., Stern, C., Forman, W., Breen, J., David, L., & Tucker, W. 1997, ApJ, 482, 143

Kaastra, J. S., Ferrigno, C., Tamura, T., Paerels, F. B. S., Peterson, J. R., & Mittaz, J. P. D. 2001, A&A, 365L, 99

Kahabka, P., & van den Heuvel, E. P. J. 1997, ARA&A, 35, 69

Kaneda, H., et al. 1995, ApJ, 453L, 13

Kellogg, E. M. 1974, in *X-ray Astronomy*, ed. R. Giacconi & H. Gursky, Dordrecht: Reidel

Kellogg, E. M. 1975, ApJ, 197, 689

Kellogg, E. M., Murray, S., Giacconi, R., Tananbaum, H, & Gursky, H. 1973, ApJ, 185L, 13

Killeen, N. E. B., & Bicknell, G. V. 1988, ApJ, 325, 165

Killeen, N. E. B., Bicknell, G. V., & Ekers, R. D. 1988, ApJ, 325, 180

Kim, D. W., & Fabbiano, G. 1995, ApJ, 441, 182

Kim, D.-W., Fabbiano, G., Matsumoto, H., Koyama, K., & Trinchieri, G. 1996, ApJ, 468, 175

Kim, D.-W., Fabbiano, G., & Trinchieri, G. 1992a, ApJS, 80, 645

Kim, D.-W., Fabbiano, G., & Trinchieri, G. 1992b, ApJ, 393, 134

King, I. R. 1962, AJ, 67, 471

King, I. R. 1966, AJ, 71, 64

Kissler-Patig, M., Grillmair, C. J., Meylan, G., Brodie, J. P., Minniti, D., & Goudfrooij, P. 1999, AJ, 117, 1206

Kriss, G. A., Cioffi, D. F., & Canizares, C. R. 1983, ApJ, 272, 439

Lamb, F. K., Pethick, C. J., & Pines, D. 1973, ApJ, 184, 271

Landini, M., & Monsignori Fossi, B. C. 1990, A&AS, 82, 229

La Parola, V., Peres, G., Fabbiano, G., D.-W., Kim, & Bocchino, F. 2001, ApJ, 556, 47

Lewin, W. H. G., van Paradijs, J., & van den Heuvel, E. P. J. 1995, *X-ray Binaries*, Cambridge University Press, UK

Loewenstein, M., & Mathews, W. G. 1987, ApJ, 319, 614

Loewenstein, M., Mushotzky, R. F., Angelini, L., Arnaud, K. A., & Quataert, E. ApJ, 555L, 21

Loewenstein, M., Mushotzky, R. F., Tamura, T., Ikebe, Y., Makishima, K., Matsushita, K., Awaki, H., Serlemitsos, P. J. 1994, ApJ, 436L, 75

Longair, M. S. 1992, *High Energy Astrophysics - Second edition*, vol.1, p. 100, ed. Cambridge University Press, UK

Longair, M. S. 1998, *Galaxy Formation*, ed. Springer-Verlag, New York

Lubow, S. H., & Shu, F. H. 1975, ApJ, 198, 383

Mackie, G., et al. 1996, in ASP Conference Series, Vol. 101, "Astronomical Data Analysis Software and Systems V", G. H. Jacoby and J. Barnes eds.

Makishima, K., et al. 2001, PASJ, 53, 401

Mason, K. O., & Rosen, S. R. 1985, Space Science Reviews, 40, 675

Mathews, T. A., Morgan, W. W., & Schmidt, M. 1964, ApJ, 140, 35

Matsumoto, H., Koyama, K., Awaki, H., Tsuru, T., Loewenstein, M., & Matsushita, K. 1997, ApJ, 482, 133

Matsushita, K., Makishima, K., Ikebe, Y., Rokutanda, E., Yamasaki, N., Ohashi, T. 1998, ApJ, 499L, 13

Matsushita, K. 2001, ApJ, 547, 693

Matsushita, K., Belsole, E., Finoguenov, A., & Böhringer, H. 2001, in preparation

Matsushita, K., Ohashi, T., & Makishima, K. 2000, PASJ, 52, 685

Mazzotta, P., Markevitch, M., Vikhlinin, A. , Forman, W. R., David, L. P., & VanSpeybroeck L. 2001, ApJ, 555, 205

McNamara, B.R., Wet al. 2000, ApJ, 530L, 81

Merrifield, M. R. 1998, MNRAS, 294, 347

Meszaros, P., Nagel, W., Ventura, J. 1980, ApJ, 238, 1066

Mewe, R., Gronenschild, E. H. B. M., van den Oord, G. H. J. 1985, A&AS, 62, 197

Miley, G. 1980, ARA&A, 18, 165

Minkowski, R. 1961, AJ, 66, 558

Mitsuda, K., et al. 1984, PASJ, 36, 741

Morgan, W. W., Kayser, S., & White, R. A. 1975, ApJ, 199, 545

Morganti, R, Fanti, R., Gioia, I. M., Harris, D. E., Parma, P., & de Ruiter, H. 1988, A&A, 189, 11

Nagel, W. 1981a, ApJ, 251, 278

Nagel, W. 1981b, ApJ, 251, 288

Nugent, J. J., Jensen, K. A., Nousek, J. A., Garmire, G. P., Mason, K. O., Walter, F. M., Bowyer, C. S., Stern, R. A., & Riegler, G. R. 1983, ApJS, 51, 1

Nulsen, P. E¿ J. 1982, MNRAS, 198, 1007

Ostriker, J. P., & Hausman, M. A. 1977, ApJ, 217L, 125

Ostriker, J. P., & Tremaine, S. D. 1975, ApJ, 202L, 113

O'Sullivan, E., Forbes, D. A., & Ponman, T. J. 2001, MNRAS, 328, 461 (astro-ph/0108181)

Pacholczyk, A. G. 1970, *Radio Astrophysics*, W H. Freeman & Co., San Francisco, US

Paolillo, M, Fabbiano, G., Peres, G., &, Kim, D.-W. In "X-Ray Astronomy 2000", ASP Conference Series, Vol. 234, 2001, R. Giacconi, S. Serio and L. Stella, eds.

Paolillo, M., Fabbiano, G., Peres, G., & Kim, D.-W. in press in the proceedings of the conference "Sesto 2001 - Tracing Cosmic Evolution with Galaxy Clusters", Sesto Pusteria (Bolzano), 3-6 July 2001

Paolillo, M., Fabbiano, G., Peres, G., & Kim, D.-W. 2002, in press in ApJ

Parma, P., de Ruiter, H. R., Fanti, C., & Fanti, R. 1986, ApJS, 64, 135

Pellegrini, S. 1994, A&A, 292, 395

Pellegrini, S., & Fabbiano, G. 1994, ApJ, 429, 105

Peterson, J. R., et al. 2001, A&A, 365L, 104

Petterson, J. A. 1978, ApJ, 224, 625

Pfeffermann, E., et al. 1987, Proc. SPIE, 733, 519

Pringle, J. E., & Rees, M. J. 1972 A&A, 21, 1

Rangarajan, F. V. N., Fabian, A. C., Forman, W. R., & Jones, C. 1995, MNRAS, 272, 665 (RFFJ)

Raymond, J. C., & Smith, B. W. 1977, ApJS, 35, 419

Reynolds, C. S., Heinz, S., Begelman, M. C. 2001, ApJ, 549L, 179

Richstone, D. O. 1975, ApJ, 200, 535

Richstone, D. O. 1976, ApJ, 204, 642

Robertson, J. G. 1983, Proc. of the Astronomical Society of Australia, 5, 144

Roettiger, K., Burns, J. O., & Locken, C. 1996, ApJ, 473, 651

Saglia, R. P., Kronawitter, A., Gerhard, O., & Bender, R. 2000, ApJ, 119, 153

Sakai, S., Giovanelli, R., & Wegner, G. 1994, AJ, 108, 33

Sandage, A., & Tammann, G. 1981, A Revised Shapley-Ames Catalog of Bright Galaxies, (Washington: Carnegie Institution of Washington)(RSA)

Sarazin, C. L. 1988, *X-ray Emission from Clusters of Galaxies*, ed. Cambridge University Press

Sarazin, C. L., & Bahcall, J. N. 1977, ApJS, 34, 451

Sarazin, C. L., Irwin, J. A., & Bregman, J. N. 2000, ApJ, 544L, 101

Sarazin, C. L., Irwin, J. A., & Bregman, J. N. 2001, ApJ, 556, 533

Sarazin, C. L., & White, R. E. 1987, ApJ, 320, 32

Schechter, P. L. 1976, ApJ, 203, 297

Schneider, D. P., & Gunn, J. E. 1982, ApJ, 263, 14

Schombert, J. M. 1986, ApJS, 60, 603

Serlemitsos, P. J., Loewenstein, M., Mushotzky, R. F., Marshall, F. E., & Petre, R. 1993, ApJ, 413, 518

Shakura, N. I., & Sunyaev, R. A. 1973, A&A, 24, 337

Smith, E. P., et al. 1996, ApJS, 104, 287

Snowden, S. L., McCammon, D., Burrows, D. N., & Mendenhall, J. A. 1994, ApJ, 424, 714 (SMB)

Stark, A. A., Gammie, C. F., Wilson, R. W., Bally, J., Linke, R. A., Heiles, C., & Hurwitz, M. 1992, ApJS, 79, 77

Sulkanen, M. E., & Bregman, J. N. 2001, AJ, 548L, 131

Sun, M., Murray, S. S., Markevitch, M., & Vikhlinin, A. 2000, to appear in the proceedings of the American Astronomical Society, HEAD meeting #32, #13.05

Taam, R. E., & Fryxell, B. A. 1988, ApJ, 327L, 73

Tamura, T., et al. 2001, A&A 365L, 87

Tanaka, Y., Inoue, H., Holt, S. S. 1994, PASJ, 46L, 37

Thomas, P. A., Fabian, A. C., Arnaud, K. A., Forman, W., Jones, C. 1986, MNRAS, 222, 655

Toniazzo, T., Schindler, S. 2001, MNRAS, 325, 509

Trentham, N. 1998, MNRAS, 294, 193

Trinchieri, G., & Fabbiano, G. 1985, ApJ, 296, 447

Trinchieri, G., Fabbiano, G., & Canizares, C. R. 1986, ApJ, 310, 637

Trinchieri, G., Pellegrini, S., Wolter, A., Fabbiano, G., & Fiore, F. 2000, A&A, 364, 53

Tully, R. B. 1988, *Nearby Galaxies Catalog*; Cambridge University Press

Ulmer, M. P., et al. 1981, ApJ, 243, 681

Vaiana, G., et al. 1981, ApJ, 245, 163

van den Heuvel, E. P. J. 1992, in *X-ray Binaries and Recycled Pulsars*, ed. E. P. J. van den Heuvel and S. A. Rappaport, p.233

Weinberg, S. 1972, *Gravitation and Cosmology: Principles and Applications of the General Relativity*; New York, Wiley

van Paradijs, J., & Verbunt, F. 1984, *High Energy Transient in Astrophysics*, ed. S. E. Woosley, (A.I.P., NY), p.31

Vedder P. V., Trester J. J., & Canizares C. R. 1988, ApJ, 332, 725

Wegner, G., Haynes, M. P., Giovanelli, R. 1993, AJ, 105, 1251

Weisskopf, M. C., O'dell, S. L., van Speybroeck, L. P. 1996, SPIE, 2805, 2

White, D. A. 1992, PhD thesis, Univ. Cambridge

White, N. E., Kaluzienski, J. L., & Swank, J. H. 1984, *High Energy Transient in Astrophysics*, ed. S. E. Woosley, (A.I.P., NY), p.31

White, N. E., Nagase, F., & Parmar, A. N. 1995, in *X-ray Binaries*, ed. W. Lewin, J. van Paradijs, & E. van den Heuvel, Cambridge Univ. Press

White, R. E., & Sarazin, C. L. 1987, ApJ, 318, 621

White, R. E., & Sarazin, C. L. 1991, ApJ, 367, 476

Whitmore, B. C., McElroy, D. B., & Schweizer, F. 1987, ApJ, 314, 439

Whitmore, B. C., McElroy, D. B., & Tonry, J. L. 1985, ApJS, 59, 1